Cosmological Constraints on Weakly Coupled Portals

THESIS

submitted in partial fulfillment of the
requirements for the degree of

MASTER OF SCIENCE
in
PHYSICS

Author :	Tycho Blom
Student ID :	1866001
Supervisor :	Dr. A. Boyarsky
2^{nd} corrector :	Dr. V. Cheianov

Leiden, The Netherlands, July 22, 2021

Cosmological Constraints on Weakly Coupled Portals

Tycho Blom

Instituut-Lorentz, Leiden University
P.O. Box 9500, 2300 RA Leiden, The Netherlands

July 22, 2021

Abstract

The Standard model of particle physics is extremely successful in explaining accelerator data. However, it is incomplete and fails to resolve several phenomena known as beyond the Standard model (BSM) problems. The BSM problems may be solved by introducing new particles. In addition to particle experiments, cosmological observation offers a way we can put limits on the parameters of these new particles. This work gives a detailed qualitative description of several such cosmological constraints. The observations used are described, and then ways in which new particles could impact such observations. Then, these constraints are applied to two case studies: the scalar portal and the neutrino portal. In both cases, a significant part of the parameter space unexplored by direct experimental studies can be excluded based on these cosmological arguments.

Contents

Version of July 22, 2021– Created July 22, 2021 - 14:39

Chapter 1

Introduction

1.1 Standard Model of Elementary Particle Physics

As the name implies, the Standard Model (SM) concerns elementary particles. These particles, with no known sub-structure, are considered the fundamental constituents of matter and forces [1]. Mathematically, the different particles are described as excitations of one of several quantum fields, which together form the Standard Model [2].

The full quantum field theory is based on the gauge group $SU(3) \times SU(2) \times U(1)$. In this expression, $SU(3)$ is the symmetry group of the strong interaction, giving rise to 8 massless spin-1 gauge bosons, called gluons. $SU(2) \times U(1)$ is the symmetry group of the electro-weak interaction, from which the $W^{\pm}$ and Z bosons, as well as photons, arise as spin-1 gauge bosons as well.

Additionally, among the elementary particles are the spin-$\frac{1}{2}$ fermions, which are classified into three flavors of both leptons and quarks. Leptons are only charged under the electro-weak interactions, while quarks also have a *color* charge, corresponding to the strong force.

Finally, there is the spin-0 Higgs boson. The Higgs field is responsible for the electro-weak symmetry breaking, which gives mass to the $W^{\pm}$ and Z bosons through the Higgs mechanism. The $SU(2) \times U(1)$ symmetry is spontaneously broken, leaving a residual $U(1)_{EM}$ symmetry, which is the gauge symmetry of the electromagnetic interaction. This leaves a massive Higgs boson and a non-vanishing vaccuum expectation value (v.e.v.), which lends the fermions their mass as well.

Since the original formulation of the electro-weak sector with the Higgs mechanism[3–5] and then the strong sector[6–8], the Standard Model has had all of its necessary predicted particles experimentally confirmed [9–

Version of July 22, 2021– Created July 22, 2021 - 14:39

19]. The culmination of this success, the discovery of the Higgs boson in 2012 [20–23], has firmly cemented the SM as an accurate and self-consistent theory up to the Planck scale [24].

1.2 Beyond Standard Model

However, the SM might be self-consistent, but it is also incomplete. Certain observations cannot currently be reconciled with the SM in its current form; these are called Beyond Standard Model (BSM) problems.

The most immediately obvious shortcoming of the SM is the lack of a description of gravity and its corresponding force carrier, the graviton. However, since quantum gravity starts to play a role in phenomenology only at the Planck scale, $\mathcal{O}(10^{19}\,\mathrm{GeV})$, we currently lack the data needed to distinguish between different models[i]. In fact, even a 100% accurate detector the size of jupiter could not detect even a single graviton in the lifetime of the universe [26], so we do not expect conclusive data on quantum gravity any time soon. For now, our classical model of gravition, General Relativity, is very accurate for energies we can currently access[27], so we do not consider this a BSM problem here.

Generally, something is called a BSM problem only when an observed phenomenon is inconsistent with the SM. The most glaring issues are:

Neutrino Oscillations and Masses

In the SM, neutrinos are massless particles. They belong to one of three flavours: electron, muon or tauon; their lepton flavours are conserved in reactions [28]. However, since the original "Solar Neutrino Problem", in which it was found that the amount of detected electron neutrinos was not consistent with the theoretical predictions[29], numerous experiments have consistently shown that neutrinos are massive, and they change between the three flavours [30]. This phenomenon is known as *neutrino oscillations*. Though there is theoretical precedent for such oscillation mechanisms [31], there is no mechanism for neutrino mass generation in the SM without introducing new physics [32].

[i] In some models of quantum gravity, particularly those with extra compactified spatial dimensions, the gravitational interactions are modified at high energies by propagation of gravitons into the higher dimenional space-time. As a result, in these models, the Planck scale where we might observe quantum gravity effects is significantly reduced, allowing for some current tests of certain phenomenological models for quantum gravity [25]

Baryon Asymmetry of the Universe

We find, from a wide range of observations [33–36], that our universe is composed of matter, with no cosmologically significant amounts of anti-matter. This apparent asymmetry is unlikely to be an initial condition of the universe, since inflation would exponentially dilute any pre-existing baryon number [37]. Generation of a baryon asymmetry requires the fulfilment of the "Sakharov conditions"[38]:

1. A baryon number violating process; clearly, if the initial baryon number is zero, some baryon number violation must occur in order to generate asymmetry.

2. C and CP violation; particles and anti-particles must behave fundamentally differently, otherwise the process in 1. would act symmetrically both ways and cancel out.

3. Non-equilibrium; in thermal equilibrium, even non-conserved quantum numbers will remain symmetric, so the baryon number violation must occur when the universe is out of equilibrium.

As it turns out, the first condition is obeyed in the SM (in the early universe) [39]. As for the second condition, the SM does exhibit both C and CP violation [40, 41], but the CP violation is too weak to account for the observed asymmetry [42, 43]. The third condition could in principle be fulfilled in the SM, provided that the electro-weak symmetry breaking is a first-order phase transition [39]. This is, however, ruled out by the observed mass of the Higgs boson [44–46]. Therefore, in order to explain baryon asymmetry, we need some addition to the SM.

Dark Matter

Dark matter is perhaps the most well-known unsolved problem in all of physics and needs little explanation. There is a wealth of observational evidence, including measurements from galaxy rotation curves [47], galaxy clusters[48], gravitational lensing [49, 50] and the Cosmic Microwave Background [34], that the majority of matter in the universe does not emit any electromagnetic radiation. This "dark" matter composes about 27% of the total energy of the universe [34].

The only particles in the SM that are both electrically neutral and stable are neutrinos, which, since they have mass, could account for a portion of the observed dark matter. In order to constitute all dark matter, though, the sum of neutrino masses is observed to be too small[34, 51]. Also, in

this case structure formation would evolve quite differently, which would leave significant marks on our current universe[52]. In addition, phase-space arguments require fermionic particles to exceed a few hundred eV to account for all dark matter in Dwarf galaxies (a few tens of eV for galaxies) [53, 54]. All in all, SM neutrinos cannot provide an explanation for the majority of dark matter, so we require an extension.

Of course, some unsatisfying aspects of our current understanding of physics may also be considered problems, such as some Hierarchy problems or the origin of the Cosmological Constant, but these do not exhibit incongruencies between theory and observation, so they are typically not included in BSM problems [37].

1.3 Portals

Although neutrino mass generation generally does require adding some new field to the Lagrangian [32, 55] and both issues with the SM for producing baryon asymmetry require introducing additional particles as well [56, 57], dark matter has several proposed solutions. Although attempts to explain dark matter phenomena by modifiyng gravity have come under scrutiny in light of some challenging measurements[58, 59], a more exotic proposed solution, primordial black holes, remains a reasonable candidate[ii] [61–63]. That said, most of the compelling dark matter candidates do involve introducing new particles to the SM [64], which seems natural, since we know that it is incomplete from the other BSM problems.

So how do we go about adding one or more additional particles to the SM? A new particle that interacts with the SM could directly address some BSM problem, or act as mediators, or *portals*. These portals would couple to some hidden sector[iii], connecting it to the SM. Since such a coupling must retain the existing gauge (and Lorentz) symmetry of the SM, there is limited number of possible portals, especially when we add the condition of *renormalizability*. This means that for each loop order, we can adjust parameters in order to calculate observables in finite terms, which preserves unitarity (makes sure probabilities do not exceed 1)[2].

[ii] Recent microlensing measurements put stringent constraints on the abundance of primordial black holes in a certain mass region, but this does not exclude the possibility of the majority of dark matter comprising lighter black holes [60].

[iii] Additional particles that are not currently part of the SM are collectively referred to as the "dark" or "hidden" sector.

There are only three renormalizable (coupling dimension ≤ 4) portals[iv][37, 65]:

- Scalar portal; introduces a new scalar particle S, coupling with the Higgs doublet H:

$$\mathcal{L}_S = (\alpha_1 S + \alpha S^2)(H^\dagger H) \tag{1.1}$$

- Vector portal; introduces a new $U(1)$ massive gauge field A'_μ, coupling with the $U(1)$ weak hypercharge field B_μ:

$$\mathcal{L}_{A'_\mu} = \frac{\epsilon}{2} F'_{\mu\nu} F^{\mu\nu} \tag{1.2}$$

  with $F'_{\mu\nu} = \partial_\mu A'_\nu - \partial_\nu A'_\mu$ and $F_{\mu\nu} = \partial_\mu B_\nu - \partial_\nu B_\mu$

- Neutrino portal; introduces a new fermion N, coupling with the SU(2) lepton doublet L:

$$\mathcal{L}_N = F_\alpha (\epsilon_{ab} \bar{L}_{\alpha,a} H^*_b) N \tag{1.3}$$

  with $a, b \in \{1, 2\}$ and $\alpha = e, \nu, \tau$

Note that the term "portal" sometimes refers to both the coupling term itself and the associated particles.

1.4 Cosmological Beam Dump

While portals can be, and are, constrained in particle experiments, cosmological constraints can offer sensitivity to generally much much weaker couplings. In a beam dump experiment, exotic states are generated by shooting a high-energy particle beam into a fixed target. After propagating through some filter, they decay or scatter in the empty environment inside the detector, generating some measurable signal.
Cosmological constraints are analogous in that new particles are produced in the hot, dense plasma of the early universe, subsequently decay to affect various stages of universal evolution, generating a measurable signal.

[iv] We describe here superficial renormalizability based on a power counting argument. Actually, higher dimensional couplings can be considered as effective field theories, applicable up to a certain energy scale. These apparent "non-renormalizable" terms could in fact arise from a complete renormalizable theory with more degrees of freedom.

Version of July 22, 2021– Created July 22, 2021 - 14:39

This method of studying weakly coupled particles has therefore been aptly dubbed the *cosmological beam dump* [66].

In this work we will aim to provide a general scheme for contraining the parameter space of these portals using cosmological observations. In the next chapters, we will briefly discuss these observations and their origins, and then the way that portals could impact these phenomena. We then provide as case studies detailed discussions of the Scalar and Neutrino portals, applying the previously discussed techniques to constrain them, focusing on sub-GeV masses.

In particular, we will focus on qualitative descriptions and physical understanding of these techniques. This leads to general analytical and semi-analytical constraints which are very broadly applicable. However, these constraints typically cannot compete with the efficiency of numerical work and simulations. The downside to numerics is that they can be difficult to understand and control. As such, the main goal of this work is not so much to constrain the parameter space of weakly coupled portals, as it is to give a detailed, qualitative description of the physics involved in several methods to do so.

Chapter 2

Astrophysical and Cosmological Observations

There are many different observations that have the potential to constrain decaying or annihilating particles. The majority and most important of these fall within the categories outlined and briefly explained below.

2.1 X-ray Background

The X-ray and gamma-ray backgrounds are diffuse spectra of x- and gamma-rays[i]. Since the inital discovery in 1962[67] (1964 for gamma-rays[68]), the characteristics and origin of this background has been of considerable interest. Over the years, detailed measurements of the total spectrum have been performed, down to sub-keV energies [69, 70] and up to 100 GeV[71].

One relevant feature of the X-ray sky at energies above $\sim$2 keV is the Galactic Ridge X-ray Emission[72, 73]. This is a narrow strip along the galactic plane that sources a significant X-ray contribution, which are generally considered to be originating from discrete sources, like accreting white dwarfs and coronally active stars[74–76]. The near isotropy of the rest of the background points to an extragalactic and possibly cosmological origin[77]. The X-ray spectrum is thought to originate mostly from discrete sources as well, particularly quasars and other Active Galactic

[i]Typically, a distinction is made in the literature between the X-ray background and the gamma-ray background, on account of the different energies requiring different detectors for the measurement of the spectra. Up to $\sim$100 keV energies are considered X-rays and higher energies are classified as gamma-rays.

Nuclei (AGN's)[78–80]. The gamma-ray spectrum is largely associated with supernovae[81, 82], with the very high energies originating from X-ray-selected BL Lacertae objects[83, 84], which are an extreme subclass of AGN[85].

A discussion of the X-ray background in the context of new physics is incomplete without mention of the 3.5 keV line. This is an emission line found in the X-ray spectrum of several galaxy clusters and the Andromeda galaxy[86–89]. Several origins have been proposed, including astrophysical solutions[90, 91] and new physics solutions (notably, decaying dark matter[92]). Though the topic is subject to prolific debate[93–95], more observational data is needed for a concensus conclusion. For a more comprehensive account of the observations and possible solutions, see [96] and references therein.

2.2 Cosmic Microwave Background

The Cosmic Microwave Background (CMB) is diffuse, nearly isotropic background radiation consisting of faint microwaves. A major triumph of modern precision cosmology, measurements of the CMB hold special significance, since it's the oldest remaining electromagnetic radiation. Since its accidental discovery in 1964 [97][ii], details of the structure of the CMB have served as confirmation of the Big Bang description of the universe and provided important insights about its evolution. Nowadays, precision measurements of minute temperature anisotropies from the Wilkinson Microwave Anisotropy Probe (WMAP)[99] and the Planck spacecraft [34] are some of the most important verifications of the ΛCDM model of cosmology.

Origin of the CMB

In the early universe, the temperature of the plasma exceeded the ionisation energy of a hydrogen atom, 13.6 eV, which means that electrons and protons could not effectively combine to form neutral hydrogen. During this time, the universe was opaque for photons, because of the abundance of charged electrons participating in Compton scattering (or Thomson scattering, if you will).
At some point, due to the expansion, the temperature got low enough so

[ii] Technically, the first registered measurement of the CMB occured in 1941, but its significance was not recognised at the time[98].

that neutral hydrogen atoms could not simply get ionised by that background. This did not occur at a temperature $T = 13.6$ eV, because there are many more photons than baryons (as we will see below), so the high-energy tail that was capable of ionising the hydrogen remained significant until much lower temperatures; almost all electrons were bound at around $T = 0.26$ eV[iii]. This process is called "recombination". At this point, there are are no longer charged electrons to scatter the photons, and they start to travel freely. This period is sometimes referred to as photon decoupling, or the "time of last scattering". It is precisely these photons that have travelled ever since recombination from the surface of last scattering, roughly 370000 years after the Big Bang[102].

Features of the CMB

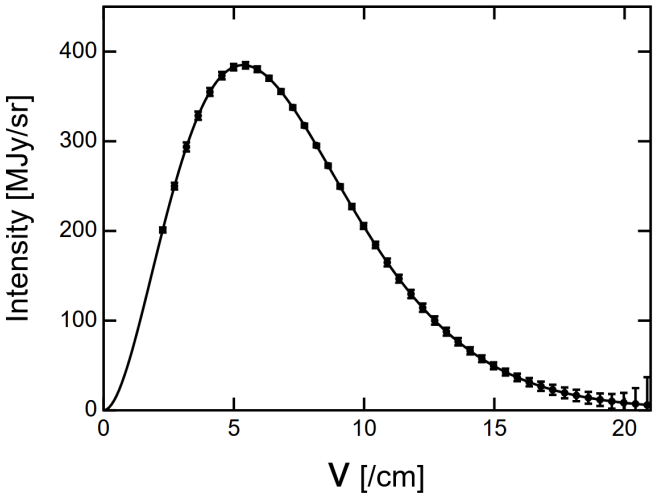

Figure 2.1: *Spectrum of the CMB from FIRAS data[103], fitted to a blackbody spectrum with temperature $T = 2.728$ K. In order to make the uncertainty visible, the error bars shown correspond to a confidence of 400σ, which is indistinguishable from* 100% *confidence. Image from [104].*

One striking aspect of the CMB is its frequency spectrum, pictured in Figure 2.1, which is of a near perfect blackbody form. It was measured quite precisely by the FIRAS instrument aboard the COBE satellite[103]

[iii]Strictly speaking, the dynamics of this process are more involved. Direct recombination of electrons to the ground state of hydrogen is not efficient, so they enter in the excited states first and then cascade down. Both the cosmic background and emitted photons can ionise atoms with excited electrons, so an accurate temperature figure requires a more detailed approach. The $T = 0.26$ eV number is a result of this calculation[100–102]

and it remains the most perfect blackbody spectrum ever measured[105]. This is exactly what would be expected from a simple Big Bang model, but energy release in the early universe (such as that from decaying or annihilating particles) could distort this spectrum[106, 107], details of which we will discuss in the next chapter. As such, these measurements have put stringent constraints, or ruled out entirely, alternative models of cosmology or structure formation [108, 109].

Another important feature is the anisotropy, meaning the CMB temperature is not exactly the same in every direction. The characteristic shape of this anisotropy is shown in Figure 2.2. The exact structure of this anisotropy, especially at smaller angular differences, is very rich and many complex physical phenomena have subtle effects, but its basic origin is as follows:

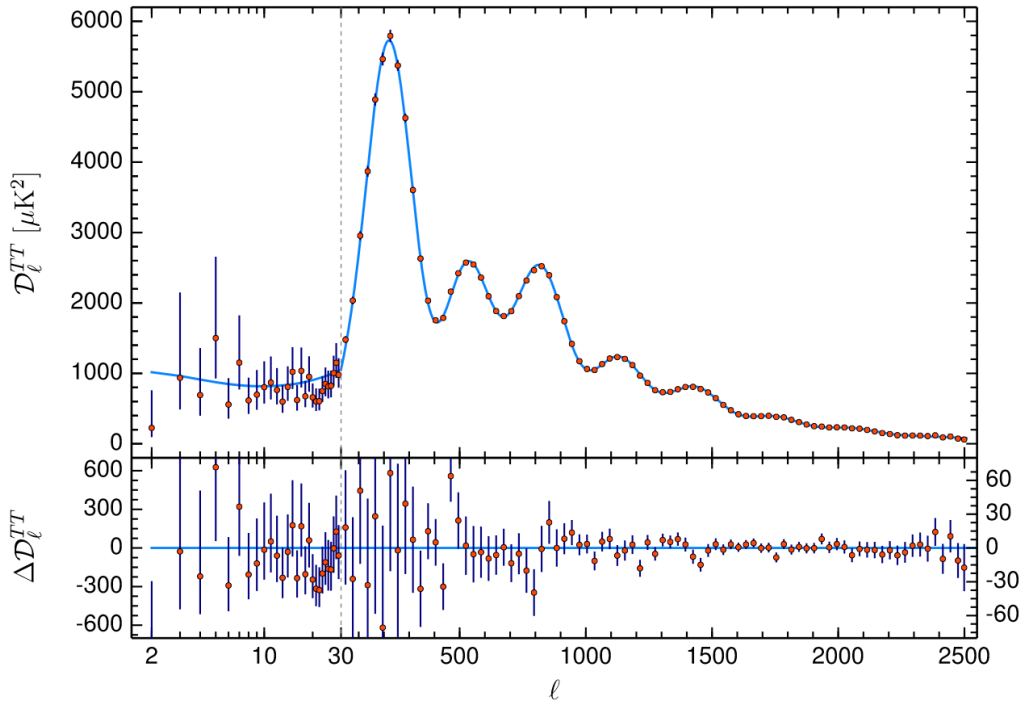

Figure 2.2: *Temperature power spectrum of the CMB as a function of the multipole moments ℓ from Planck. These arise from the Fourier decomposition of the spectrum into spherical harmonics. Higher multipoles correspond to smaller angular scales. From [34].*

Before recombination, as was discussed, the photons are tightly cou-

pled to the electrons and protons due to Compton scattering. Since the photon mean free path is so small at this time, a fluid description is applicable; the photon-baryon fluid. There is a significant pressure, coming from the photons, and a significant gravity from the baryons, which have competing effects. Gravity causes the fluid to clump, while pressure causes it to spread out. This results in "sound waves" in the plasma, acoustic oscillations. These density perturbations, creating compressed hot spots and diluted cold spoty, are the main source of (*primary*) anisotropy [105, 110, 111].
However, recombination is not instantaneous. Due to decreasing free electron densities, the photon mean free path gradually increases from almost zero to the size of the observable universe. These free moving photons diffuse, due to the pressure, equilising the density fluctuations by dragging along some of the baryonic matter from hot to cold. This is called diffusion damping, and it decreases anisotropy in small angular scales[110, 112, 113].

Then, between recombination and now, the travelling photons are subject to a number of effects that can cause additional (*secondary*) anisotropy. These can be classified into two categories: gravitational effects and ionisation effects. Gravitational effects can be effectively summarised as such: metric distortions along the path of the photon will induce gravitational redshift[114]. This is because, due to the expansion of the universe, the depth of the potential well changes as the photon travels, so that the blueshift from infalling does not cancel the redshift from outgoing[110]. Examples of these types of effects are the Integrated Sachs-Wolfe (ISW) effects[iv], and the Rees-Sciama effect, which is the non-linear extention to the late-time ISW[115].
The scattering effects are caused by the period of reionization, when the universe temporarily reverted back to a charged plasma, due to ionization from photons emitted by the first stars and quasars [116]. In this time, though the electrons density was much diluted compared to the pre-recombination era due to the expansion, Compton scattering again occured. Anisotropy could then arise from scattering by ionized regions of varying bulk motion with respect to the Hubble flow (the Vishniac or Ostriker-Vishniac effect[117, 118]), inhomogeneities in the ionization fraction[119] or the Sunyaev-Zel'dovich effects[120], which can induce both

[iv] Not be confused with the non-integrated Sachs-Wolfe effect, which describes the gravitational redshift induced from potential wells at the surface of last scattering, part of the primary ansiotropy induced by density perturbations, together with the intrinsic temperature fluctuations[114].

Version of July 22, 2021– Created July 22, 2021 - 14:39

temperature and spectral distortion anisotropies due to the upscattering of photons by high-energy electrons from galaxy clusters[110, 111].

Effective Number of Neutrino Species

Through their specific influence on the CMB anisotropy, detailed measurements of many cosmological parameters have been made, such as the curvature of the universe k, the dark matter density Ω_{DM} and the baryon-to-photon ratio $\eta \equiv n_B/n_\gamma$, the ratio of number densities of baryons and photons[v], which will be of particular importance. Another parameter found from the CMB, which we will be especially interested in for the purpose of contraining new physics, is the effective number of neutrino species, N_{eff}. It parametrises any additional energy density in the neutrino bath; its definition requires some introduction.

The (effective) number of relativistic degrees of freedom:

$$g_* = \sum_{\text{bosons}} g_i + \frac{7}{8} \sum_{\text{fermions}} g_i$$

(where the $7/8$ factor comes from the Fermi-Dirac distribution as opposed to the Bose-Einstein distribution) is an important evolving parameter in cosmology. In particular, it determines the radiation energy density $\rho_{rad} = g_* \frac{\pi^2}{30} T^4$ (and thus the expansion rate in the radiation-dominated era) and the total entropy density of the universe $\tilde{s} = g_* \frac{2\pi^2}{45} T^3$ (non-relativistic contributions to the entropy are always negligible) [102].

As the early universe cools down, many particles become non-relativistic at some point and no longer contribute to g_*, making it decrease monotonically [121]. In the standard model, the last of these particles to undergo this transition are electrons and positrons, as they are the lightest massive particles (recall that neutrinos are assumes massless). This happens when the cosmic temperature crosses the eletron rest mass (~ 0.5 MeV), so new electrons and positrons cannot be created from the background anymore (they only annihilate). However, shortly prior to this, the neutrino interaction rate with electrons and positrons becomes smaller than the rate of expansion (the Hubble rate), so the average neutrino will never interact with the other SM particles again; this is called "freeze-out".

[v] This ratio η is time-independent, since at temperatures well below the electro-weak scale, there are no baryon number violating processes[102].

The neutrino freeze-out, which occurs at $T \simeq 1.4$ MeV[122], effectively decouples the neutrinos from the photon-electron bath[vi]. So when the electrons and positrons annihilate, all the energy from the electron/positron part of the radiation energy density gets transferred only to the photon bath, and not the neutrino bath, creating a temperture difference.

This can be shown explicitly by using entropy conservation in a comoving volume. This applies for systems in equilibrium, which the photon-electron bath obeys. Thus we can write: $g_*^{e,\gamma} a^3 T_\gamma^3 =$ constant, with T_γ the photon temperature and $g_*^{e,\gamma}$ the degrees of freedom of the photon-electron bath. Since we have $g_*^{e,\gamma} = 11/2$ before electron-positron annihilation and $g_*^{\gamma} = 2$ after, we can equate:

$$\begin{aligned} g_*^{e,\gamma} a^3 T_\gamma^3 \Big|_{\text{before}} &= g_*^{e,\gamma} a^3 T_\gamma^3 \Big|_{\text{after}} \\ \frac{11}{2} T_{\gamma\text{before}}^3 &= 2 T_{\gamma\text{after}}^3 \\ \Rightarrow T_{\gamma\text{before}} &= \left(\frac{4}{11}\right)^{1/3} T_{\gamma\text{after}} \end{aligned}$$

Since the neutrino temperature does not change during this process, after electron-positron annihilation, we can say $T_\gamma = T_{\gamma\text{after}}$ and $T_\nu = T_{\text{before}} = (4/11)^{1/3} T_\gamma$. Now, any deviation from this energy relation is parametrised in term of N_{eff} like $\rho_\nu = N_{eff} \frac{7\pi^2}{120} T_\nu^4$[122, 125, 126], or:

$$N_{eff} \equiv \frac{8}{7} \left(\frac{11}{4}\right)^{4/3} \frac{\rho_\nu}{\rho_\gamma} = 3 \left(\frac{11}{4}\right)^{4/3} \left(\frac{T_\nu}{T_\gamma}\right)^4 \tag{2.1}$$

As can be easily seen from the right-hand side, the standard case we just considered gives $N_{eff} = 3$, which seems appropriate, given the 3 neutrino species in the standard model. However, detailed calculation of the temperature evolution of the neutrino bath actually gives $N_{eff} \simeq 3.045 - 3.046$ for the standard model value[127, 128]. This is because neither the neutrino decoupling, not the electron-positron annihilation happens instantaneously, and since the are quite close in time, there is some relic interaction,

[vi] Much like the CMB from photon decoupling, there is a background of relic neutrinos originating from neutrino decoupling. This takes place at a significantly earlier time, it would be another valuable and detailed source of information on the early universe. Indirect evidence for its existence has confirmed its existence[123], but direct detection of the neutrino background remains out of experimental reach, because low-energy neutrinos are notoriously difficult to detect[124].

Version of July 22, 2021– Created July 22, 2021 - 14:39

slightly heating the neutrino bath[vii]. That said, we will not consider this difference in this work, because it will be small with respect to the effects we consider.

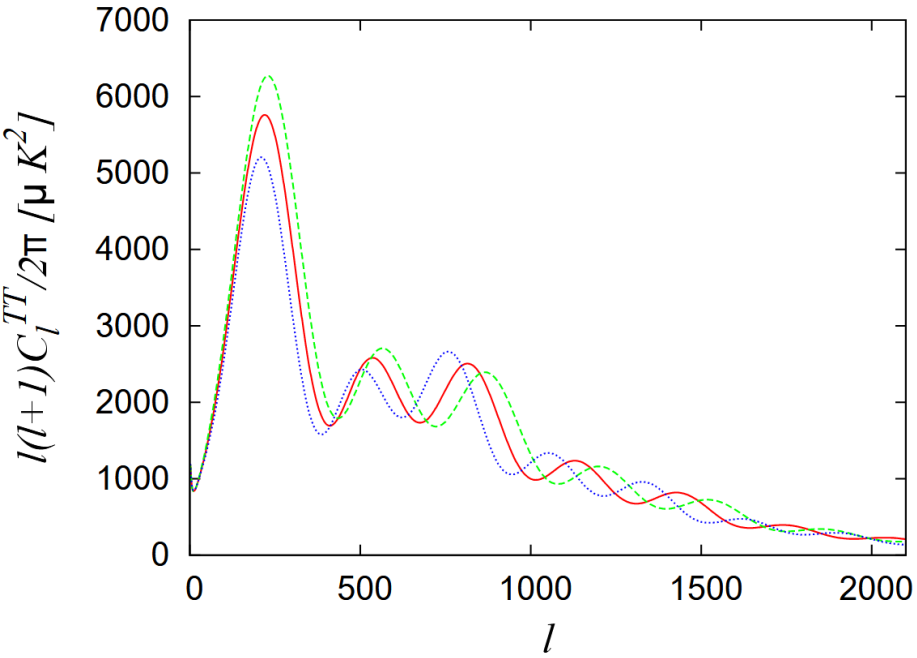

Figure 2.3: *CMB power spectra for the cases with $N_{eff} = 1$ (blue dotted line), 3 (red line) and 5 (green dashed line), where the other cosmological parameters are kept unchanged. From [125].*

The way N_{eff} is constrained by the CMB anisotropy is often misunderstood [133]. As shown in Figure 2.3, naively changing N_{eff} while keeping other parameters fixed results in significant changes to the spectrum. These occur because a change in the radiation density implies a change in the expansion rate (the Hubble parameter H) before and during recombination. This has a noticeable effect on other observables we can measure from the CMB, including the Λ energy density and the total matter density, and consequently, the sound horizon r_s, the distance sound waves could travel since the start of the universe until recombination[134]. The sound horizon angle $\theta_s = r_s/D_A$, where D_A is the angular size distance, is very tightly constrained by the angular position of the acoustic peaks

[vii]The modern value is a result of both finite temperature QED corrections[129, 130] and flavour oscillation effects[127, 131, 132] that have to be accounted for

Version of July 22, 2021– Created July 22, 2021 - 14:39

of the CMB anisotropy spectrum (not their height), making the constraint very insensitive to changes in the model[34, 134].

That said, it is quite difficult to constrain N_{eff} by using θ_s. While θ_s is well constrained, r_s and D_A are calculated from other cosmological parameters, the constraints on which are much more model-dependent. Since there is some uncertainty in the measured values of the baryon and total matter densities, the effect on θ_s of a change in N_{eff} can be compensated by changes in the other parameters within their allowed ranges.
However, the diffusion length r_d, the characteristic length scale for diffusion damping, has a much weaker dependence on these densities[134, 135]. Even though the diffusion angle $\theta_d = r_d/D_A$ is less strongly constrained by observation, we can use it to constrain N_{eff} independently of other cosmological parameters as follows:

Changes in N_{eff} do not induce significant changes in the inferences of the baryon density Ω_b, the redshift at matter-radiation equality $1 + z_{EQ}$ or θ_s[133]. Thus, we should study the effects of varying N_{eff} while keeping these quantities fixed (by adjusting the Λ and dark matter densities). Then, we find that $r_s \propto H^{-1}$, so we can infer that $D_A \propto H^{-1}$ as well, in order to keep θ_s fixed. In contrast, $r_d \propto H^{-1/2}$, which means that $\theta_d \propto H^{1/2}$. This means the damping angular scale increases with increasing N_{eff}, which leads to more diffusion damping[133, 138]. Figure 2.4 shows the effects, when the fixed parameters are considered, as well the fact the effect of Big Bang Nucleosynthesis on the CMB can be partly degenerate with the effect of N_{eff}. We will take a closer look at that.

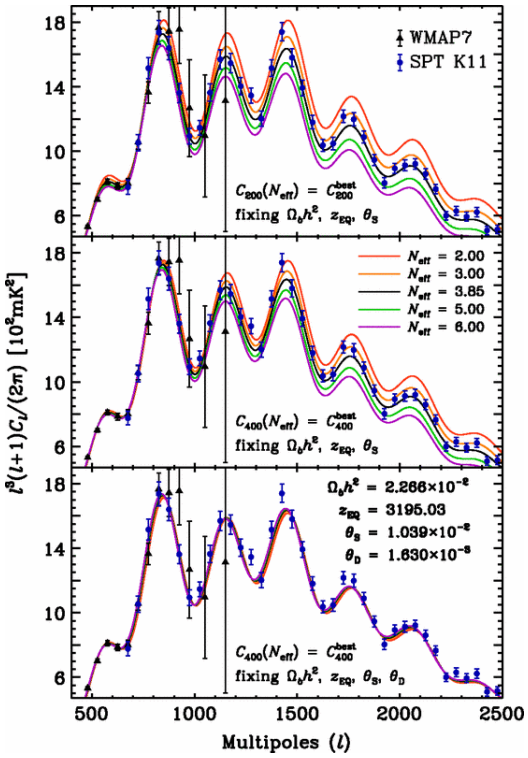

Figure 2.4: *Top: CMB anisotropy data from WMAP[136] and the South Pole Telescope (SPT)[137] and several theoretical curves with varying N_{eff} and fixed $\Omega_b h^2$, $1 + z_{EQ}$ and θ_s. Data and curves are normalised at $\ell = 200$. Middle: Same as top, except normalised at $\ell = 400$. Bottom: Same as middle, except Y_p, the helium mass fraction (a parameter from Big Bang Nucleosynthesis, see below), is varied to keep θ_d fixed. The lack of scatter indicates that N_{eff} indeed affects the CMB through diffusion damping primarily, like Y_p (see below for explanation). In addition, a phase shift forms, which is subtle and described in [138]. Image from [133].*

2.3 Big Bang Nucleosynthesis

Big Bang nucleosynthesis (BBN) describes the production of light nuclei (other than ^{1}H, which is just one proton) in the very early universe. Besides the CMB, it is the major source of information on the early universe, occuring even earlier in its evolution; during the first $\sim$ 20 minutes after the Big Bang [139]. The theory of BBN began in the 1940s with the famous Alpher-Bethe-Gamow paper[140], and has since evolved into a powerful framework with very good agreement between theory and experiment[139, 141, 142].

Standard BBN (SBBN), which assumes the Standard Model for microphysics and the ΛCDM model for cosmology, starts with protons and neutrons. When the universe cooled below the hadronisation (or Hagedorn) temperature $T_H \sim 160$ MeV, quarks became confined and formed matter [121, 143–145]. Since all other hadrons rapidly decay[viii], eventually only protons and neutrons will be present in significant amounts[147]. They are produced and destroyed the weak processes:

$$p + e \leftrightarrow n + \nu_e$$

and crossings. This keeps protons and neutrons in chemical equilibrium, with a ratio related to their masses: $n_n/n_p \equiv R_n \approx \exp(-(m_n - m_p)/T)$. At $T \approx 0.75$ MeV[148, 149], these interactions undergo freeze-out, so the equilibrium is lost. At this point, $R_n \approx 0.18 \equiv R_n^0$, but while the protons are stable, neutrons will decay, so this ratio will drop by the time other nuclei can form as such: $R_n(T) = R_n^0 \exp(-t(T)/\tau_n)$, where $\tau_n \approx$ 880s[150, 151] is the neutron lifetime.

This is important, because nucleosynthesis is delayed; the universe first has to cool down to a temperature where deuterium (^{2}H or D) doesn't get dissociated by the high-energy tail of the photon background. The reason we have to wait for deuterium, which is not very tightly bound and quite easily dissociated, is that the chances of three or more nucleons to come together to form a nuclues are negligibly small, so the main production processes for nuclei are two-body reactions. Thus, the heavier nuclei, starting with tritium (^{3}H or T) and helium-3 (^{3}He), require an abundance of deuterium. This is called the "deuterium bottleneck" [36, 152].

As it turns out, the characteristic temperature associated with nucleosynthesis is $T_{NS} \approx 75$ keV, depending logarithmically on η[102]. At this point, nuclear reactions proceed rapidly, and the interconnected reaction channels (see Figure 2.5) start to produce and burn up the different nuclei. At the end, most neutrons will be caught in helium-4 (^{4}He), because is has the largest binding energy of all the light nuclei[ix] and so the final ^{4}He

[viii] Actually, there is a significant amount of pions up until quite late, in fact dominating the protons and neutrons until $\sim$ 6 MeV, because of production from high-energy photons[146, 147]

[ix] Actually, there is also a non-trivial reason for this: burning of ^{3}He and T proceeds faster than their production from deuterium burning. If this was not the case, then the production processes of ^{4}He ($^3\text{He} + \text{D} \rightarrow^4 \text{He} + p$ and $\text{T} + \text{D} \rightarrow^4 \text{He} + n$) could not burn up the remaining ^{3}He and T after deuterium burned out and those neutrons would not end up in ^{4}He[102].

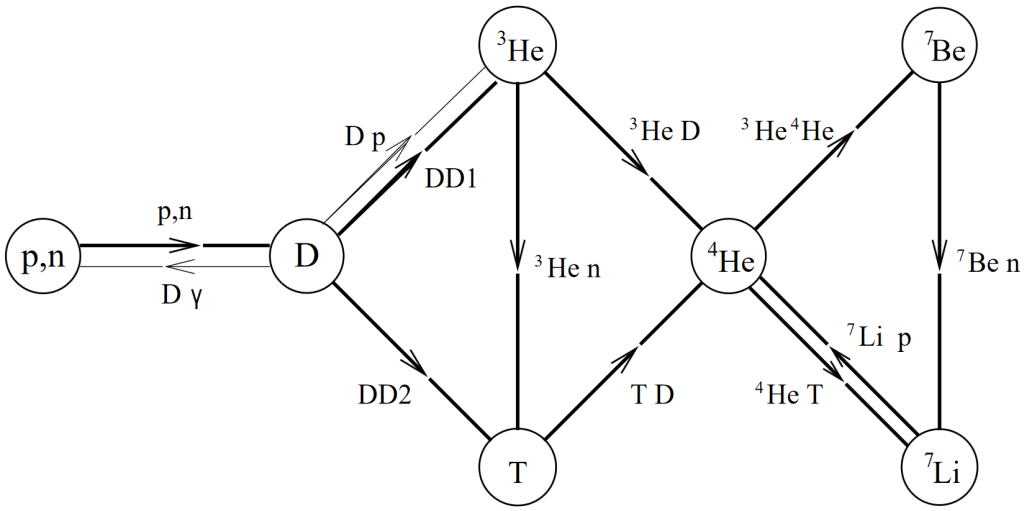

Figure 2.5: *Schematic representation of the most important reactions in BBN. Along the reaction paths only the initial elements are written, since the result can be easily inferred. From [152].*

abundance can be estimated from the neutron/proton ratio at $T_{NS} \approx 75$ keV. This is typically presented as a mass fraction $Y_p \equiv 4n_{^4\mathrm{He}}/n_B = 2R_n/(1+R_n)$. We find $R_n(T_{NS}) \approx 0.14$, which gives $Y_p \approx 0.25$.

More precise values can be found[x], but that typically requires a full numerical calculation of the entire BBN process, though detailed analytical work can also yield good results[152]. Similarly, the abundances of the other light elements, all the way up to ^{7}Be, can be calculated given the nuclear reaction rates, which can be found from experiment. Thus, the only free parameter in SBBN is η (or, equivalently, the baryon density $\Omega_B h^2$)[xi], which can be checked with the independent value from CMB[36, 141]. Then, using the CMB measured η value, the BBN predictions can be checked with the measured abundances, providing tight constraints on deviations from SBBN[141, 156].

[x] Including small but relevant corrections from several sources (including radiative, finite mass, QED plasma and neutrino decoupling effects) yields the value $Y_p = 0.24709 \pm 0.00017$ [142, 153]

[xi] N_{eff} is an example of a parameter which can vary in non-standard BBN that then becomes another imporant parameter[154, 155].

Observed Abundances: Helium

One problem that one faces when determining the primordial ^{4}He abundance is the fact that it is also produced in significant amounts post-BBN in stars. Thus, this needs to be taken into account for the different measurement methods used to determine Y_p.

A common and very effective type of measurement uses He and H emission lines in low-metallic[xii], extragalactic HII regions[36, 142, 157–159]. These are interstellar regions of ionised hydrogen, formed when stars born in giant molecular clouds become hot enough to ionise the surrounding gas[160]. Due to stellar nucleosynthesis, both increased amounts of helium and metals are found in these regions. Therefore, in order to get the primordial ^{4}He abundance, a correlation is found between abundances of helium and metallicity (typically represented by oxygen[36, 158]) with multiple measurements in these regions and this is (linearly) extrapolated down to zero metallicity. This is quite a complex method, and despite its efficacy, it does introduce significant systematic uncertainties[161, 162].

Another type of measurement uses not emission but absoption lines from intergalactic gas clouds, back-lit by quasars. These quasar absoption line systems have the potential to be near-pristine, so very low in metallicity[163, 164], which decreases the need for extrapolation. Although the application of this technique for the determination of the primordial helium abundance is of a recent origin[165], it is a promising way of providing an independent measurement from the previous method, thus countering some of the systematic uncertainties associating with it.
Finally, the CMB can be used as an independent measurement of Y_p. Instead of assuming SBBN and calculating Y_p from the measured value of η, we can allow Y_p to vary freely and derive model-indepedent constraints, because Y_p has a direct effect on the damping tail of the CMB. This can be explained as follows: helium recombines earlier than hydrogen[xiii], because it has a higher ionisation energy. Therefore, only the electrons that are not caught in helium take part in the hydrogen recombination. The electron number density around the time of recombination can thus be expressed: $n_e = (1 - Y_p)n_B$. The photon mean free path in the fluid, which is

[xii] In astronomy, all elements heavier than helium are considered metals, contributing to the metallicity Z [36].

[xiii] Actually, helium recombination proceeds in two steps, because it can catch two electrons. The second helium recombination finishes around the time hydrogen recombination begins [168–170].

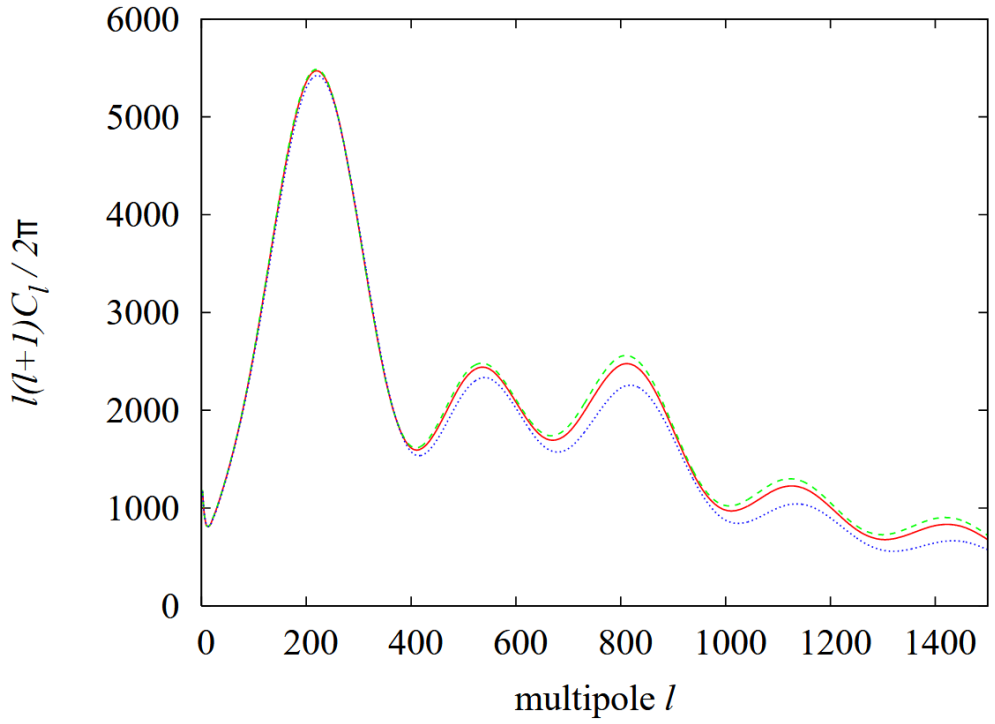

Figure 2.6: *CMB power spectrum for $Y_p = 0.1$ (green dashed line), $Y_p = 0.24$ (red line) and $Y_p = 0.5$ (blue dotted line). All other cosmological parameters are taken from the first WMAP results[166]. Image from [167].*

the characteristic length scale for diffusion damping, depends on the free electron number density $\lambda_\gamma \propto 1/n_e$, so a higher Y_p increases the damping of the CMB anisotropies[167, 170]. This is shown explicitly in Figure 2.6. In fact, since the effect of N_{eff} and Y_p on the damping tail of the CMB is partially degenerate, both can be allowed to vary, giving combined model independent constraints. Including an independent emission line measurement from [158] and using the Planck 2018 results for the CMB gives at 2σ confidence[34]:

$$Y_p = 0.2437^{+0.0077}_{-0.0080}$$
$$N_{eff} = 2.99^{+0.43}_{-0.40}$$

This is the range for N_{eff} we will be using. For Y_p, however, in concordance with [171], we will use a wider upper limit from [157]: $Y_p < 0.2573$. As we will discuss, only the upper limit will be relevant for our constraints. Since this is the largest experimentally found deviation from the SBBN value, so it will result in the most conservative bounds.

Observed Abundances: Deuterium

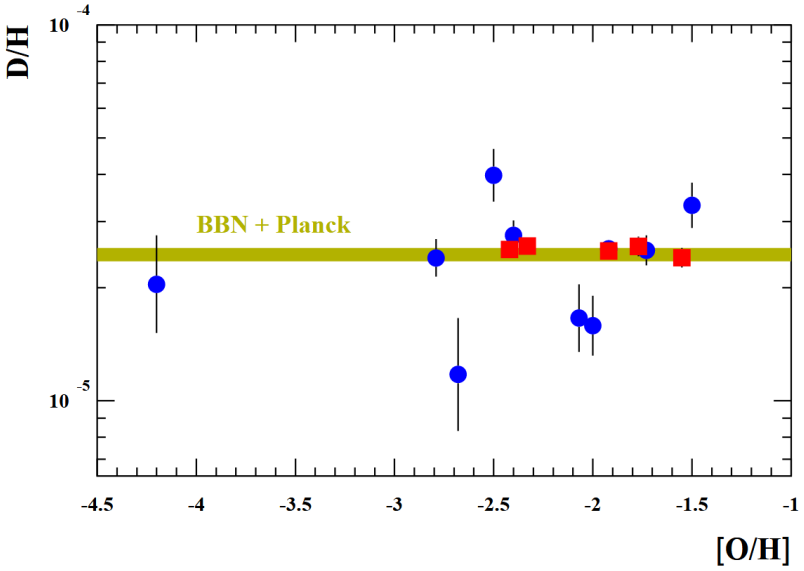

Figure 2.7: *D/H observations from [172] (blue circles) and [173] (red squares), as a function of metallicity, represented by oxygen concentration. There is no strong correlation between O/H and D/H, congruent with [165], indicating that these are indeed primordial abundances. Image from [139].*

The deuterium case is almost the opposite of the helium case, in that while helium is created in stars and not destroyed, deuterium is only destroyed in stars, and there are no known astrophysical production mechanisms for it[xiv]. As a result, all deuterium must be of primordial origin, and its abundance monotonically decreases over time. Thus, all measurements of deuterium provide a lower limit on the primordial deuterium abundance[142].

These measurements are all done using the absoption line method described above. The systems suitable for deuterium detection have to obey certain specific conditions[176], so they are few and far between. Measurement of deuterium abundance has had a tumultuous history[142] and even in the past 25 years, many measurements have shown a considerable dispersion[177–184], indicating some unaccounted systematic uncertain-

[xiv] Technically, production of deuterium is possible in proton capure of neutrons in stellar flares[174], however this is a small effect and cannot compensate for the total destruction of deuterium[175].

ties.

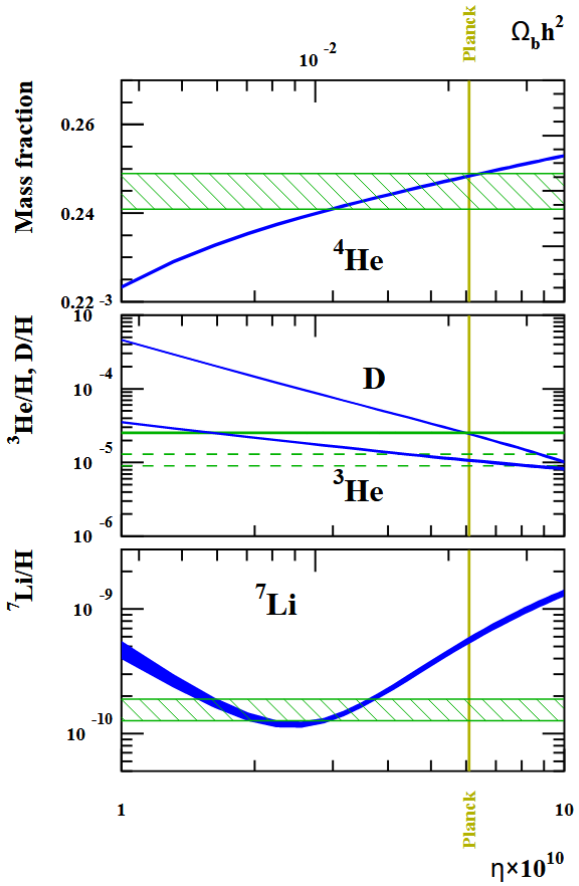

Figure 2.8: *Schramm plot, showing abundances of ^4He (by mass fraction), D, ^3He and ^7Li (by number relative to H) as a function of the baryon over photon ratio η (or equivalently the baryon density Ω_b). The green horizontal stripe corresponds to observation, while the blue curves correspond to BBN calculated values, with the measured value of η from Planck 2015 [185] shown as a vertical stripe. Data for abundances are taken from [186]. Image from [139].*

More recent works, as shown in Figure 2.7, show a significant improvement in precision[172, 173], with the most recent work showing remarkable precision and consistency[165]. These low uncertainty results are reasonably consistent with BBN calculations[139, 142, 165, 186, 187]. We use the value found in the most recent and most precise measurement: $D/H \equiv n_D/n_H = (2.527 \pm 0.030) \times 10^{-5}$ at 1σ confidence[165].

The consistency between observation of primordial abundances and measured cosmological values in conjuction with the BBN framework is shown in Figure 2.8. Notably, these is a discrepency in the ^{7}Li abundance. The characteristic dip in the BBN values over η comes from lithium production dominating the low η regime and ^{7}Be production domination the high η regime. The ^{7}Be eventually decays into ^{7}Li, which is stable, so both contribute. ^{7}Li can be both produced and destroyed in their post-BBN evolution, but using low-metallic gas clouds and metallicity correlations to approach the primoridal values, observed lithium abundance remains inconstistent with BBN calculations with the cosmological parameters from the CMB[36, 139, 142]. This cosmological lithium problem is an important unsolved issue in astrophysics, but it will not be considered in this work.

Chapter 3

The Impact of Portals

Portals could, depending on their abundance, influence the aforementioned observations measurably, through decay or annihilation into SM particles. Consequently, those measurements provide constraints on the parameters of these portals. We focus here on the effects of particle decay, but these general constraints can be straightforwardly adapted to fit an annihilating particle scenario.

3.1 X-ray Background

Increasingly detailed observations on X-ray and gamma-ray spectra put upper bounds on the luminosity from decaying or annihilating dark matter particles. I explicitly mention dark matter here, because any hidden particle that survives until present day[i] will inevitably act as at least a part of the observed dark matter, since it must interact gravitationally. In this light, much work has been done on both model-specific and general constraints on dark matter[188–195].

These constraints can be subdivided into two categories: local flux from the Milky Way halo and flux from cosmological distances, originating from the smooth distribution of dark matter throughout the universe. For decaying particles, which will be our chief interest, both of these are of similar importance[189, 196]. The local galactic contribution of decaying dark matter to the differential photon flux per unit energy is given

[i] Or rather: until the relatively recent history from which the X-ray and gamma-ray signals originate.

by[189, 195]:

$$\frac{\mathrm{d}\Phi_G}{\mathrm{d}E} = \frac{r_\odot \rho_\odot}{4\pi m_{DM}} \Gamma_{DM} \frac{\mathrm{d}N_\gamma}{\mathrm{d}E} J_{DM} \tag{3.1}$$

Here, $r_\odot \approx 8.5$ kpc is our distance to the galactic center, $\rho_\odot = 0.3\mathrm{GeV/cm}^3$ the local dark matter density, Γ_{DM} the dark matter decay rate, $\mathrm{d}N_\gamma/\mathrm{d}E$ the decay spectrum and

$$J_{DM} = \int_{\text{l.o.s.}} \frac{\rho(s)}{\rho_\odot} \mathrm{d}s\, \mathrm{d}\Omega$$

is a dimenionless number describing the density of decays along the line-of-sight (l.o.s.), where s is the distance from the sun in units of $r_\odot$[ii], over the solid angle Ω. For decays, the specific galactic density profile $\rho(s)$ is not very important[195]; we will use a Navarro-Frenk-White (NFW) profile, which can be succinctly written[197, 198]:

$$\rho_{NFW}(r) = \frac{\rho_\odot}{\frac{r}{r_c}(1+\frac{r}{r_c})^2}$$

with $r_c = 20$ kpc, the critical radius, which indicates a slope change. Importantly, r indicates a distance from the galaxy center, so there should be a conversion. Written in terms of s, as defined above, and l and b, the longitudinal and latitudinal coordinates, respectively[189]:

$$r^2(s,b,l) = r_\odot^2 \left[(s - \cos b \cos l)^2 + (1 - \cos^2 b \cos^2 l)\right]$$

Then, the extragalactic contribution is isotropic, but it comes from many different distances. As a result, because each photon is redshifted accordingly, even a monochromatic photon line would get smeared out to a continuous energy spectrum. In addition, different comsologies produce differen results. Since we are interested in recent decays, we need only consider the history of the universe after radiation domination (so only matter and a cosmological constant Λ will be relevant): $H(z) = H_0\sqrt{\Omega_\Lambda + \Omega_m(1+z)^3}$, where H_0 is the current Hubble parameter and $\Omega_{m,\Lambda}$ are the respective matter and Λ density contributions to the universe. Taking a flat universe ($\Omega_m + \Omega_\Lambda = 1$) and defining $\kappa \equiv \Omega_\Lambda/\Omega_m \approx 3$, we can then write the extragalactic differential photon flux per solid

[ii]Note that we use here the dimensionless definition for s, used in [189], and not the dimensionful distance used in [195].

Version of July 22, 2021– Created July 22, 2021 - 14:39

angle[195, 199–201]:

$$\begin{aligned}\frac{\mathrm{d}^2\Phi_{EG}}{\mathrm{d}\Omega\mathrm{d}E} &= \frac{\Gamma_{DM} n^0_{DM}}{4\pi}\int_0^\infty \frac{\mathrm{d}N_\gamma}{\mathrm{d}E(z)}\frac{1}{H(z)}\mathrm{d}z \\ &= \frac{\Gamma_{DM} n^0_{DM}}{4\pi H_0\sqrt{\Omega_m}}\int_0^\infty \frac{\mathrm{d}N_\gamma}{\mathrm{d}E(z)}\frac{1}{\sqrt{\kappa+(1+z)^3}}\mathrm{d}z\end{aligned} \tag{3.2}$$

where n^0_{DM} is the number density of dark matter presently, and $E(z) = E\cdot(1+z)$ is the energy of the photon when emitted at redshift z, when E is the energy is has at detection.
Typically, one would consider a decay to a monochromatic photon line, which yields $\mathrm{d}N_\gamma/\mathrm{d}E = \delta(E(z) - m_{DM}/2) = (1/E)\delta((1+z) - m_{DM}/2E)$. The integral in z then reduces:

$$\int_0^\infty \frac{\mathrm{d}N_\gamma}{\mathrm{d}E(z)}\frac{1}{\sqrt{\kappa+(1+z)^3}}\mathrm{d}z = \frac{1}{E}\frac{1}{\sqrt{\kappa+(\frac{m}{2E})^3}} = \frac{2}{m}\sqrt{\frac{2E}{m}}\frac{1}{\sqrt{1+\kappa(\frac{2E}{m})^3}}$$

where we omitted the DM subscript on the mass m for ease of notation. This shows clearly that a monochromatic line evolves into a continuous spectrum at detection.

Dark matter decaying into charged particles will generate additional, different photon spectra through final state radiation. For different possible decay products with different initial energy distributions, this can get quite complex. For simplicity, we will consider only masses below the electron-threshold, so these final state radiations will not apply.

Comparing these calculated signals to the observed spectra can put very general, quite strong constraints on decaying dark matter. As shown in Figure 3.1, decaying dark matter lifetime must exceed 10^{26} seconds, more than 10^8 times the age of the universe. However, a particular particle does not need to account for *all* dark matter; multiple portals may well be collectively responsible for the observed phenomena. Since we are primarily concerned with constraining these portals individually, we have to adapt these general constraints. In particular, photon flux from both sources scales as $\Phi_\gamma \propto \Gamma_{DM}\rho_{DM}$, so a constraint on the lifetime of a particle comprising all dark matter translates into a weaker constraint on the lifetime of a particles comprising only a part by exactly the ratio of densities: $\tau_{Part} = \tau_{DM}\cdot\frac{\rho_{Part}}{\rho_{DM}}$. The specifics of this with respect to certain portals will be discussed in their respective sections. Importantly, we assume in these constraints that the particle we constrain follows the density

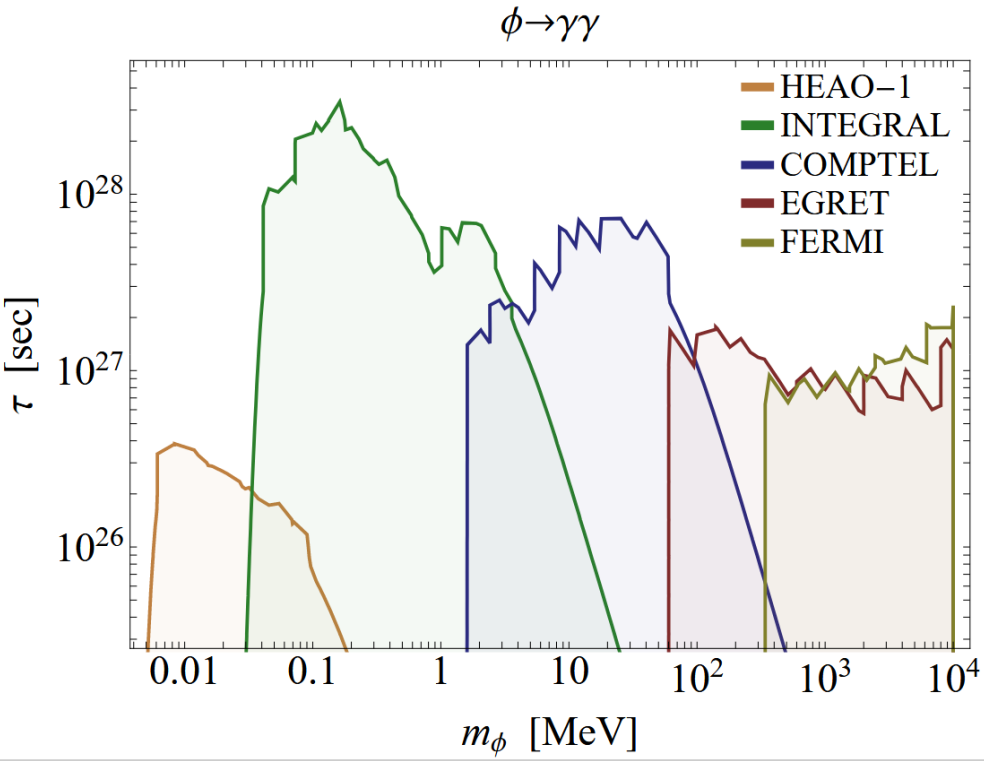

Figure 3.1: *Constraints on lifetime of a scalar dark matter particle ϕ decaying only to two photons. The ϕ particle is assumed here to be the source of all dark matter density in the universe. From [195].*

distribution of dark matter.

Following the general analysis done in [195], we use data for 3-50 keV photons from the High Energy Detector A2 onboard the High Energy Astronomical Observatory 1 (HEAO-1) [77] and data for 20-511 keV photons from the SPI instrument on INTEGRAL [202]. The well-resolved 511 keV line is removed in the latter dataset.

3.2 CMB Spectral Distortions

The impressive precision with which the CMB spectrum corresponds to a perfect blackbody[107] can be used to contrain injected energy before and during recombination (from decaying particles, for example)[203, 204]. This is because while thermalisation is very efficient at early times, several processes responsible for thermalisation eventually become slower, due to

the expansion. As a result, injection of electromagnetic energy at different times will induce different distortions in the CMB energy spectrum[205, 206].

Very early injection $z > z_\mu \simeq 2 \times 10^6$ has no measureable impact on the shape of the spectrum, because at this time, Compton scattering, double Compton scattering and Bremsstrahlung act very fast to keep everything in equilibrium; all additional energy goes into the temperature of the CMB[207]. After that point, we can distinguish two types of distortions, called μ-type and y-type distortions [**?**].
First, between $z_\mu \gtrsim z \gtrsim z_{\mu y} \simeq 5 \times 10^4$, Compton scattering is still efficient, so a kinetic equilibrium is achieved, but double Compton scattering and Bremsstrahlung become slow. These latter processes produce photons, while the former process cannot, so the number of photons at this point can change only on slow timescales. This means that for low frequencies, the situation is unchanged and full equilibrium is achieved, but for high frequencies the number of photons is effectively fixed. Therefore, at high frequencies, a change in the number of photons induces a change in the energy of the system. Thus, if electromagnetic energy is injected at this time, a frequncy-dependent chemical potential $\mu(\nu)$ forms, which is approximately constant at high frequencies and vanishes at low frequencies[206, 208].

Then, for $z \lesssim z_{\mu y}$, Compton scattering stops being very efficient, so a full equilibrium between electrons and photons can no longer be achieved. Thus, there is no effective way for photons in different frequency ranges to distribute their energy. Thus, injected energy at this time induces a decrease in temperature for the low-frequency photons and and increase for the high-frequency photons; this is called Compton y-distortion[206, 209].

These types of distortions are characterised by the dimensionless parameters μ and y. The μ parameter is simply the dimenionless chemical potential, so that the Planck law of blackbody radiation is distorted at high frequencies to become[107]:

$$S_\mu(\nu, T, \mu) = \frac{2\nu^3}{e^{\frac{\nu}{T}+\mu} - 1}$$

with ν the photon frequency.

The Compton y parameter describes the energy change throughout the Comptonisation process. Qualitatively, y is the fractional energy change

per scattering event times the number of events[209]. The former is just the electron temperature (different from the photon temperature) over the electron mass. The latter is simply the scattering rate of photons, which is the Thomson cross section times the electron number density (given non-relativistic electrons), integrated over the entire time of process. Thus, y is typically defined as[207, 210]:

$$y = \int \frac{T_e}{m_e} n_e \sigma_T \mathrm{d}t$$

where T_e, m_e and n_e are the electron temperature, mass and number density, respectively, and σ_T is the Thomson cross section.

Spectral distortion resulting from general injected electromagnetic energy are given by[204, 205]:

$$\mu = 1.401 \int_{z_{\mu y}}^{\infty} e^{-\left(\frac{z'}{z_\mu}\right)^{5/2}} \frac{\mathrm{d}(Q/\rho_\gamma)}{\mathrm{d}z'} \mathrm{d}z' \tag{3.3}$$

$$y = \frac{1}{4} \int_{z_{rec}}^{z_{\mu y}} \frac{\mathrm{d}(Q/\rho_\gamma)}{\mathrm{d}z'} \mathrm{d}z' \tag{3.4}$$

where $\mathrm{d}(Q/\rho_\gamma)$ is the infinitesimal injected energy element, normalised to the photon energy density[iii]. In the case of a non-relativistic decaying particle X, this can be cast in a more familiar form:

$$\mathrm{d}(Q/\rho_\gamma) = \frac{\mathrm{d}\rho_{EM\,inj}}{\rho_\gamma} = \frac{m_X n_X e^{-t/\tau_X}}{\rho_\gamma} Br_{EM} \frac{\mathrm{d}t}{\tau_X} \tag{3.5}$$

where m_X, n_X and τ_X are the mass, the number density and the lifetime of the decaying particles, Br_{EM} is the electromagnetic branching ratio (the sum of the branching ratios of electromagnetic final decay products) and ρ_γ is the photon energy density. Using $\mathrm{d}t = -\mathrm{d}z/((1+z)H(z))$, we can use the previous expressions. See Appendix A for a detailed derivation of those formulae, based on [205, 208].

These parameters are very tightly constrained by the FIRAS[107]:

$$|\mu| \leq 9 \cdot 10^{-5}$$
$$|y| \leq 1.5 \cdot 10^{-5}$$

These are the values we will be using.

[iii] Though this is an uncommon notation, we show it here for consistency with [66, 211].

Version of July 22, 2021– Created July 22, 2021 - 14:39

3.3 Neutrino Energy

In absence of other effects, injection of energy into the neutrino or the photon baths after neutrino decoupling raises or lowers N_{eff}, respectively. This can be readily seen from (2.1). In general, decay products can always be thought of as contributing to one or both of these baths. The neutrino bath requires neutrino decay products, but this is not too uncommon, especially from decaying muons and mesons. The photon bath increases in energy from decay into photons directly, but also electrons, which annihilate into photons eventually.

In this light, on a long enough timescale, all energy from decay products end up in either the photon or neutrino bath, so we may write $Br_\nu + Br_{EM} = 1$. Assuming decay happens well after neutrino decoupling, we can then calculate the change to N_{eff} by simply comparing the energy densities right before decay, and assume instantaneous decay. This gives the formula[66]:

$$N_{eff} = \frac{8}{7}\left(\frac{11}{4}\right)^{4/3} \frac{\rho_\nu^{SM} + \rho_X Br_\nu}{\rho_{EM}^{SM} + \rho_X Br_{EM}} \tag{3.6}$$

where $\rho_{\nu,EM}^{SM}$ are the standard model neutrino and photon energy density and ρ_X is the decaying particle energy density before decay. This is an effective formula, and it will not be applicable for decay that happens before or during neutrino decoupling, since the energy injected as different decay products will still interact mutually and complicate the result[212].

In addition, since these constraints effectively measure the energy density of the new particles with respect to the SM radiation, there will be a regime possible where the new particles dominate the radiation. In this case, the evolution of the universe will be heavily impacted, so we would like to constrain this region securely. To this end, we check the bounds from (3.6) with a numerical calculation, which includes effects on the expansion of the universe from the new particles, by solving the following series of coupled differential equations:

$$\begin{cases} \dot{\rho}_{EM} + 4H\rho_{EM} = \dfrac{\rho_X}{\tau_X} Br_{EM} \\ \dot{\rho}_\nu + 4H\rho_\nu = \dfrac{\rho_X}{\tau_X} Br_\nu \\ H^2 = \dfrac{8\pi G}{3}(\rho_{EM} + \rho_\nu + \rho_X) \end{cases} \tag{3.7}$$

Version of July 22, 2021– Created July 22, 2021 - 14:39

with $H = \dot{a}/a$ and $\rho_X = m_X n_X$.
We then track the temperature evolution of the neutrino and electromagnetic baths and use (2.1) to find N_{eff}. We can then be sure that these constraints hold, even in the case that the new particle dominates the energy density of the universe. That said, we do not include neutrino decoupling effects, using instantaneous decoupling, so these results are not reliable near neutrino decoupling.

However, there is also a somewhat counterintuitive effect occuring if neutrinos are injected sufficiently early (even shortly after neutrino decoupling). In fact, decay to relatively high-energy neutrinos can increase the energy of the photon bath relative to the neutrino bath. This happens because high-energy neutrinos will either form electron-positron pairs (together with thermal anti-neutrinos) or interact with the thermal neutrinos, which will in turn also becomes high-energy neutrinos. In addition, high-energy neutrinos can scatter off electrons or positrons and transfer part of their energy. These processes combined can result in a decreased N_{eff}, even when decay products are solely neutrinos[213, 214].

We avoid this complication, which requires sophisticated simulations or at the very least dedicated semi-analytical work to properly take into account, by considering only the effect of decays on N_{eff} after this no longer occurs. We can estimate the freeze-out of these high-energy neutrinos by taking the interaction rate [122] $\Gamma_{\text{non}-\text{eq}} \sim G_F^2 T^4 E_\nu^{\text{inj}}$ (where G_F is the fermi constant) and finding when it gets smaller than the Hubble rate:

$$\begin{aligned} G_F^2 T^4 E_\nu^{\text{inj}} < H(T) = \frac{T^2}{M_{Pl}^*} = \frac{1.66\sqrt{g_*}T^2}{M_{Pl}} \\ \Rightarrow T^2 < \frac{1.66\sqrt{g_*}}{G_F^2 M_{Pl} E_\nu^{\text{inj}}} \\ \Rightarrow t > \frac{G_F^2 M_{Pl}^2 E_\nu^{\text{inj}}}{2 \cdot 1.66^2 \cdot g_*} \end{aligned}$$

where in the last line, we used the time-temperature relation in a radiation dominated era $T^2 = M_{Pl}^*/(2t)$, with $M_{Pl}^* = M_{Pl}/(1.66\sqrt{g_*})$ the reduced Planck mass.
Thus, our contraints are only applicable after this time. In this work, we will take the upper limit $E_\nu^{\text{inj}} \leq m_X/2$ for the decay of particle X, and use the SBBN value for $g_* = 3.36$ after neutrino decoupling.

Version of July 22, 2021– Created July 22, 2021 - 14:39

3.4 BBN

With meaurements of BBN being one of the only probes we have of the very early universe and the impressive congruency with which the theory desribes the observed quantities, there has naturally been a wealth of research done applying BBN to constrain new physics (see [36, 149, 215–218] and references therein). The effect of portals on BBN can be categorised into three types: extra energy changing the expansion rates; change of neutron-proton ratio R_n; dissociation of light elements.

The first category is easily described, but rather difficult to apply. Injection of significant amounts of energy changes the expansion rate (and time-temperature relation), which changes the timescales associated with the various BBN processes. This effect cannot be well estimated; even small differences in expansion rates during BBN can drastically impact the resulting light element abundances. Thus, the entire BBN process needs to be numerically reevaluated in order to find the results of this injection[219–226]. As a result, we will not consider these effects in this work.

The second category can be split up into: change of the standard weak $n \leftrightarrow p$ rates (and thus the ratio) by injection of high-energy neutrinos or electromagnetic particles[227] and addition of new $n \leftrightarrow p$ processes through injection of hadrons (specifically mesons)[212, 226, 228].
We use constraints using this latter "meson mechanism" as derived in [171] for Heavy Neutral Leptons, specifally. These are, however, general constraints for particles decaying into mesons, particularly charged pions $\pi^{\pm}$ and kaons $K^{\pm}$. These mesons drive $n \leftrightarrow p$ conversion through the reactions:

$$\pi^- + p \to n + \pi^0$$
$$\pi^+ + n \to p + \pi^0$$

These reactions have no kinematic threshold, and their cross sections are much larger than the normal weak rates[216]. Because of approximate isotopic symmetry, conversions thus proceed the same in both directions, and thus drive R_n to unity. The effect of Kaons is similar, but slightly more involved, since there is no isotopic symmetry (because the reaction $K^+ + n \to p + X$ does have a threshold) and neutral Kaon take part in the conversion as well. As a result, the driving due to Kaons leads to a slightly

Version of July 22, 2021– Created July 22, 2021 - 14:39

different R_n value. This is discussed in detail in [171].

The injected mesons will decay quickly (lifetime $\tau \sim 10^{-8}$ s) if they do not partake in the conversions first. Therefore, the instantaneous number density of a meson m produced in decay of particle X is:

$$n_m^X(T) = n_X(T) Br_{X\to m} \frac{\tau_m}{\tau_X} \tag{3.8}$$

The total number of $n \leftrightarrow p$ reactions per nucleon (at time $t \gg \tau_X$) is then:

$$N_{n\leftrightarrow p}^X = \sum_m \int n_m^X(T(t)) \cdot \langle \sigma_{n\leftrightarrow p}^m v \rangle \mathrm{d}t \tag{3.9}$$

$$\approx \sum_m \left(\frac{a_{dec}}{a}\right)^3 \frac{n_X^{dec}}{n_B} \cdot e^{-t/\tau_S} \cdot Br_{X\to m} \cdot P_{conv}^m \tag{3.10}$$

with $P_{conv}^m = \frac{n_B \cdot \langle \sigma_{n\leftrightarrow p}^m v \rangle}{\Gamma^m}$, the probability of a meson m to take part in a $n \leftrightarrow p$ conversion before decaying. In the last line we assumed a particle thermalising at early times and decoupling at some time, but this is easily adapted to fit a non-thermalising particle.
At some point, $N_{n\leftrightarrow p}^X$ drops below unity; we name this temperature T_0. Then R_n relaxes to the SBBN value. If T_0 is sufficiently close to the freeze-out of the weak $n \leftrightarrow p$ rates (at $T_{\mathrm{f-o}} \approx 0.8$ MeV), the there is not enough time to relax all the way back to SBBN, and R_n remains increased. This directly increases the helium mass fraction Y_p. Using a measured upper bound on Y_p, we can find $T_0^{\min}$, the minimum allowed value of T_0, and translate it into an upper bound on tau_X:

$$\tau_X \lesssim \frac{t(T_0^{min})}{\ln\left[\sum_m (\frac{a_{dec}}{a})^3 \frac{n_X^{dec} P_{conv}^m Br_{X\to m}}{n_\gamma(T_0^{min})\eta}\right]} \tag{3.11}$$

In the study of [171], a value $T_0^{\min} \approx 1.5$ MeV is found, nearly independently of the mass of the particles. We assume this holds in general and apply it for our analyses. They also calculate the probabilities for pions and Kaons to take part in a conversion before decaying: $P_{conv} \sim 10^{-2} - 10^{-1}$ for $T \sim 1 - 2$ MeV. Though we will use the precise values for the constraints, it should be noted that relatively large differences (such as even order of magnitude differences) quickly become negligible, due to the logarithm. This makes this a very powerful constraint.

Version of July 22, 2021– Created July 22, 2021 - 14:39

This will hold for lifetimes up until they become so large that there will be a significant amount of mesons present after BBN. Then, these mesons could dissociate the helium, as we will discuss below, and counteract the overproduction from which we constrain the injection of mesons in the first place. This provides an upper limit to the applicability of this bound. This process may be neglected only if the number of mesons partaking in dissociation is much less than the number of helium nuclei at the earliest BBN temperature $T_{\rm BBN}$:

$$n^m_{\rm diss}(T_{\rm BBN}) \ll n_{^4{\rm He}}(T_{\rm BBN}) \tag{3.12}$$

where m is a meson species, and:

$$n^m_{\rm diss} = n_X \cdot Br_{X\to m}\frac{\Gamma^m_{\rm diss}}{\Gamma^m_{\rm decay}}$$

with X the new particle, $\Gamma^m_{\rm diss} = \langle\sigma v\rangle^m_{\rm diss} n_{^4{\rm He}}$ the dissociation rate for m. In accordance with [171], we use $T_{\rm BBN} = 84$ keV, assuming that at this point most of the nucleons are bounded in helium. We will use the conservative limit $n^m_{\rm diss}/n_{^4{\rm He}} < 0.01$, so the number of mesons must be less than one percent of the number of helium nulei.

Then, the final way to impact BBN: through dissociation of light elements. This can be either photo-dissociation, through high-energy photon decay or final state radiation, or hadro-dissociation, where hadrons (typically mesons) can dissociate the the light elements [222, 226, 229–232]. The results of this dissociation can be quite complex, because the final states are fed back into the BBN reaction network, potentially changing many different abundances. As a result, these constraints generally require sophisticated numerical methods at least, and often full BBN simulations [216]. Photo-dissociation adds complexity, because different photon energies can dissociate different elements. Since the most abundant element (helium) is also the hardest to dissociate, there is a balancing effect to consider, depending on the source of the radiation.

Taking inspiration from the semi-analytic description of BBN in [152], we can make some justified approximations to derive a bound from meson-dissociation of helium that approaches the efficacy of numerical methods on the same system.

Since the helium abundance is orders of magnitude larger than the other light elements (excluding hydrogen, of course), helium capture of

meson decay products dominates over other hadro-dissociations. We consider the two processes:

$$\pi^- + {}^4\mathrm{He} \to 2n + D \tag{3.13}$$

$$K^- + {}^4\mathrm{He} \to \Pi + D \tag{3.14}$$

where we use the cross sections $(\sigma v)_D^{\pi^-} \approx 4.1\text{mb}$ and $(\sigma v)_D^{K^-} \approx 20.4\text{mb}$ from [216]. Helium capture of pions or kaons can also result in other elements, T and ^{3}He, but the D final state is dominant, so it will give the most effective constraining power. These cross sections must first be adapted with a Coulomb interaction term, which in the non-relativistic limit (which is applicable, since BBN takes place around $T \approx 75$ keV) is given by[102, 216]:

$$F(Z, v) = \frac{2\pi\xi}{1 - \exp(-2\pi\xi)} \tag{3.15}$$

where $\xi = \frac{Z\alpha}{v}$ is the Sommerfeld parameter, with Z the nuclear charge and v the relative velocity. A good approximation is to use $\langle v \rangle \approx \sqrt{2T/\mu}$, where μ is the reduced mass of the particles involved. This Coulomb interaction is also the reason there is no effective process with positive mesons, since they have an additional Coulomb barrier from the positive nuclei.

As production of deuterium during BBN from helium dissociation will lead to the extra deuterium being partially burned in the producting of the heavier elements, we will conservatively consider only the production of deuterium after deuterium burning has ceased. Thus, we have to find the freeze-out temperature of deuterium burning. Using an estimate for the cross section [102]:

$$\langle \sigma v \rangle_{DD} \simeq 3 \cdot 10^{-15} \frac{\mathrm{cm}^3}{\mathrm{s}} \cdot T_9^{-2/3} \cdot \exp(-4.26 \cdot T_9^{-1/3}) \tag{3.16}$$

where $T_9 \approx T/(86\,\mathrm{keV})$ is the temperature in units of 10^9 K. This expression is reasonably accurate in the temperture range we are interested in. Using the approximate deuterium abundance at freeze-out from SBBN $n_D \approx 3 \cdot 10^{-5} n_H \approx 2.5 \cdot 10^{-5} n_H 0.75 n_B$, we can find the approximate temperature at freeze-out, when the interaction rate becomes the same as the

Hubble rate:

$$n_D \langle \sigma v \rangle_{DD} = \frac{T^2}{M_{Pl}^*}$$
$$3 \cdot 10^{-5} 0.75 \eta \frac{2\zeta(3)}{\pi^2} T^3 \cdot \langle \sigma v \rangle_{DD} = \frac{1.66\sqrt{g_*} T^2}{M_{Pl}}$$
$$T^{8/3} \exp(4.26(\frac{86\,\mathrm{keV}}{T})^{1/3}) = \frac{9\zeta(3)\eta M_{Pl}}{2 \cdot 1.66\sqrt{g_*}\pi^2} (86\,\mathrm{keV})^{2/3} 10^{-20} \frac{\mathrm{cm}^3}{\mathrm{s}}$$

where η is the baryon-to-photon ratio and we take $g_* = 3.36$, since this is well after neutrino decoupling. Solving for T, we arrive at $T_D^{\mathrm{f-o}} \approx 45$ keV. Thus, we will only take into account excess production of deuterium after $T_D^{\mathrm{f-o}}$. First, it is convenient to write the evolution of deuterium in terms of its mass fraction $X_D \equiv 2n_D/n_B$, because this is a comoving quantity and the comoving number density of baryons does not change in time (baryons are not created nor destroyed at this time). We can then write the evolution of this deuterium fraction in the absence of deuterium burning:

$$\frac{\mathrm{d}X_D}{\mathrm{d}t} = \sum_m \langle \sigma v \rangle_{m \to D} \frac{2 n_{^4\mathrm{He}} n_m}{n_B} \tag{3.17}$$

for both π^- and K^- mesons. Using $n_B = \eta n_\gamma$, $n_{^4\mathrm{He}} \approx n_B/16$ (assuming $Y_p \approx 1/4$ and each helium nucleus has four baryons) and $n_m = Br_{X \to m}(\tau_m/\tau_X) n_X(T)$ (as we did in the previous BBN constraint), we can then simply integrate to find the extra deuterium produced[iv]. Note that we assumed here that from the point of $T_D^{\mathrm{f-o}}$ onwards, the light element abundances do not change significantly, which is a fair assumption, as can be seen in Figure 3.2.

Knowing the extra deuterium that would be produced from hadrodissociation of helium from the decay products of our particle, we can constrain it by the small posible uncertainty there is currently between the measured value of D/H and the theoretically predicted value. Taking the measured value $D/H = (2.527 \pm 0.030) \times 10^{-5}$ from [165] and the latest theoretical value $D/H = (2.51 \pm 0.06 \pm 0.03) \times 10^{-5}$ from [187] (where the two errors are from the uncertainties in the nuclear rates and the baryon density, respectively), we can take the largest possible difference to get the most conservative bounds. Thus, we require the extra deuterium from helium dissociation to be less than 0.137×10^{-5}. We do note that, in order

[iv] After rewriting $n_D/n_H \approx n_D/(0.75 n_B) = (2/3) X_D$

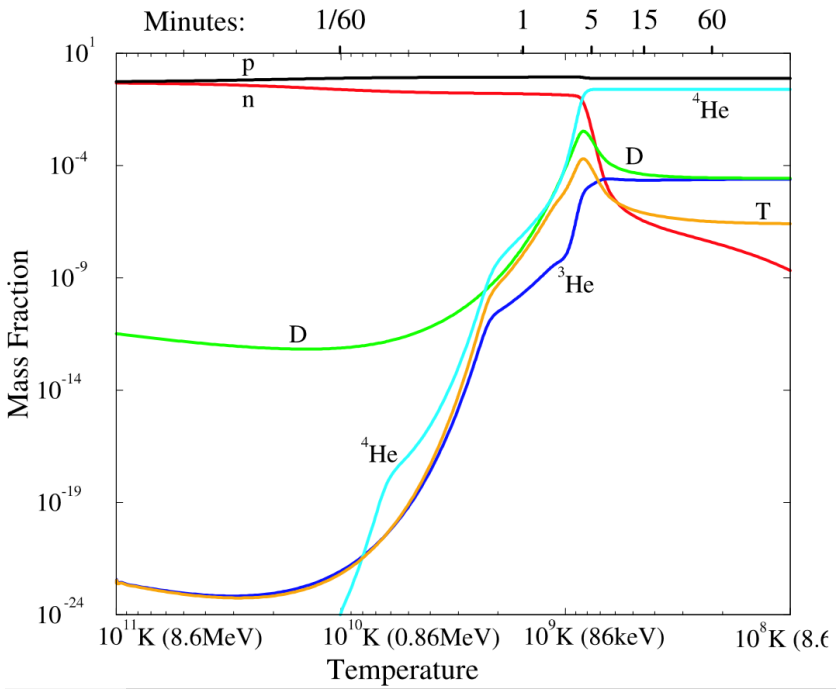

Figure 3.2: *Relative mass fractions of different particles and nuclei during BBN. From [152].*

to use the theoretical value, other deviations from SBBN must be absent or negligible. In particular, we cannot apply these bounds if the energy density of the early universe is changed significantly, which will limit the applicability of this constraint.

Chapter 4

Scalar Portal

Our first case study, the scalar portal (or Higgs portal), holds a unique position within the portal families, because of its possibility to be super-renormalizable (that is, have a coupling dimension of 3). It has been studied in connection to dark matter[233–236], inflation[237, 238] and hierarchy problems [239–241], and as a mediator to a richer dark sector [242, 243]. Following the work of Fradette *et al.*[66], we will focus on the super-renormalizable coupling and compare results.

4.1 Phenomenology

4.1.1 Higgs-like Scalar

The scalar portal describes a coupling of a scalar particle to the Higgs field. The scalar S that is introduced is chargeless, but it can have a mass term $(1/2)m_S^2S^2$ and possible self-interaction terms of the form $\lambda_3 S^3 + \lambda_4 S^4 +$ etc.. We will not consider these further interactions. The scalar part of the Lagrangian is:

$$\mathcal{L}_S = \frac{1}{2}\partial_\mu S \partial^\mu S - (1/2)m_S^2 S^2 + (AS + \alpha S^2)(H^\dagger H) \tag{4.1}$$

When the temperature of the universe cools down to below $T_c \approx 160$ GeV[244], the electro-weak symmetry is sponaneously broken, and the Higgs field gains a non-zero vacuum expectation value $v = 246$ GeV and it reduces:

$$H = \begin{pmatrix} 0 \\ \frac{v+h}{\sqrt{2}} \end{pmatrix}$$

with h the Higgs boson field. Due to this symmetry breaking, the Lagrangian in (4.1) also gets reduced (we omit the kinetic term for clarity):

$$\begin{aligned}\mathcal{L}_S &= (AS + \alpha S^2)(\frac{(v+h)^2}{2}) - (1/2)m_S^2 S^2 \\ &= \frac{1}{2}(AS + \alpha S^2)v^2 + (AS + \alpha S^2)vh + \frac{1}{2}(AS + \alpha S^2)h^2 - (1/2)m_S^2 S^2 \\ &= A(\frac{1}{2}Sh^2 + vSh) + \alpha(\frac{1}{2}S^2h^2 + vS^2h) + \frac{1}{2}\left[Av^2S + (\alpha v^2 - m_S^2)S^2\right]\end{aligned}$$

We can redefine our field and write the last term as a mass again:

$$\begin{aligned}\frac{1}{2}\left[Av^2S + (\alpha v^2 - m_S^2)S^2\right] &= \frac{1}{2}(\alpha v^2 - m_S^2)\tilde{S}^2 - \frac{A^2v^4}{8(\alpha v^2 - m_S^2)} \\ &= -\frac{\tilde{m_S}^2}{2}\tilde{S}^2 - K\end{aligned}$$

where we defined $\tilde{S} = S + Av^2/(2\alpha v^2 - m_S^2)$ and $\tilde{m_S}^2 = m_S^2 - \alpha v^2$. Because we may always redefine our field this way without loss of generality [235, 245] and the constant term K does nothing in the Lagrangian, we simply take our redefined values and call them S and m_S.
Adding also the mass of the Higgs boson, we are left with:

$$\mathcal{L}_S = -\frac{m_h^2}{2}h^2 - \frac{m_S^2}{2}S^2 + \underbrace{\frac{A}{2}h^2S}_{(a)} + \underbrace{\frac{\alpha}{2}h^2S^2}_{(b)} + \underbrace{\alpha vhS^2}_{(c)} + \underbrace{AvhS}_{(d)} \tag{4.2}$$

In this expression, while (a), (b) and (c) dictate the interaction vertices between the S and h, (d) introduces a mixing between S and h. In fact, we will consider in this work only the super-renormalizable portal, which means $\alpha = 0$, and both (b) and (c) will not be present. The addition of those quartic terms does indeed introduce new production channels, and thus change phenomenology from our case. A phenomenological analysis including the quartic coupling is done in [246].
The mixing term (d) can be combined with the masses to form a mass matrix:

$$M = \begin{pmatrix} -\frac{1}{2}m_h^2 & \frac{1}{2}Av \\ \frac{1}{2}Av & -\frac{1}{2}m_S^2 \end{pmatrix}$$

This can be diagonalised with a rotation matrix R, rotating at an angle θ, so that $R^TMR = \text{diag}(m_1, m_2)$. The condition for diagonalisation is then[37]:

$$\tan(2\theta) = \frac{2Av}{m_h^2 - m_S^2} \tag{4.3}$$

Assuming small mixing, this can be approximated to form the basic expression:

$$\theta = \frac{Av}{m_h^2 - m_S^2} \tag{4.4}$$

This means that we can use θ, called the "mixing angle", instead of A as a parameter for S.

Through this mixing, which is diagrammatically represented in Figure

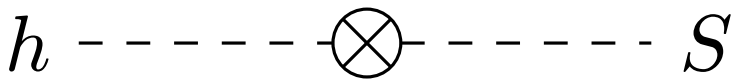

Figure 4.1: *Diagram of the mixing between h and S. Depending on the masses, free oscillation may not be efficient, but this mixing process can be though of as part of every interaction between S and the rest of the SM.*

4.1, the scalar S effectively interacts with the rest of the SM through the couplings with the Higgs. In effect, to first order, all interactions of the Higgs boson get supplemented with an interaction with S, through the transformation: $h \to h + \theta S$. This allows us to write the effective interaction Lagrangian for S with the SM:

$$\begin{aligned}\mathcal{L}_S^\theta = &- \sum_{f \in fermion} \theta \frac{m_f}{v} S\bar{f}f + 2\theta m_W^2 (\frac{1}{v} + \frac{h}{v^2}) S W^+ W^- \\ &+ \theta m_Z^2 (\frac{1}{v} + \frac{h}{v^2}) S Z^2 - \frac{3\theta m_h^2}{2v} S h^2 - \frac{\theta m_h^2}{v^2} S h^3\end{aligned} \tag{4.5}$$

where f are all fermions, and W and Z are the massive vector bosons.

4.1.2 Decay and Lifetime

If $m_S = m_h$, then the decay of S would follow exactly the branching rates of the Higgs boson, and the total rate would be surpressed by factor θ^2 [247]. However, in the case we consider, namely $m_S \ll m_h$, things get a little more complicated.

The available decay modes for S naturally depend on its mass, as decay products must always be lighter than S itself. In addition, because the coupling with SM particles, as seen in (4.5), is proportional to the mass of the particles (a result of the Higgs mixing), heavier particles generally dominate interaction with S. Because of this, as we parametrically increase the

mass m_S and new heavier decay products become possible, these heavier decay modes will quickly dominate the decay, and shown very high branching ratios (see Figure 4.2).

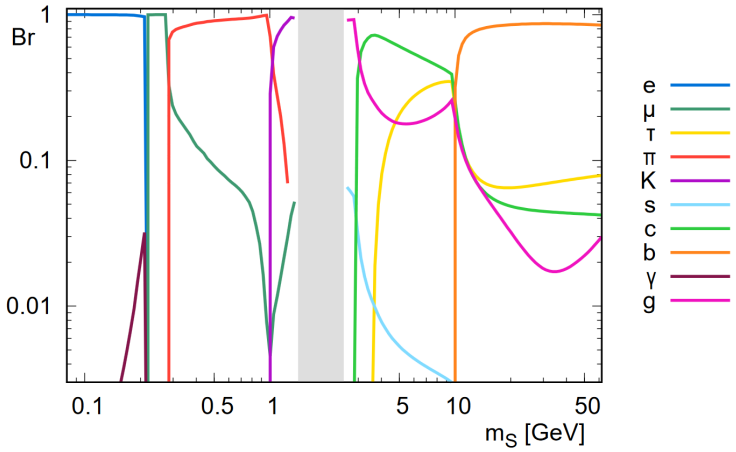

Figure 4.2: *Branching ratios for S decay as a function of m_S, for a particular value of $\theta = 10^{-6}$. The empty range shown related to theoretical uncertainties, though around $m_S \sim 1$ GeV are significant uncertainties as well (see main text). Image from [212].*

For very low masses ($m_S < 2m_e$), the only possible decay channel is to photons. Since photons are massless, there is no coupling with the Higgs (or vice versa, if you will), so the decay to photons goes through a loop of heavy charged particles[246], just like Higgs decay to photons [248]. This calculation is non-trivial, since the light quarks (u, d and s) are confined at low energies. Calculation thus involves virtual loops of pions and kaons. We follow the result presented in [66]:

$$\Gamma(S \to \gamma\gamma) = \frac{\theta^2 \alpha^2 m_S^3}{256\pi^3 v^2} \left(\frac{50}{27}\right)^2 \tag{4.6}$$

where α is the fine-structure constant.
For higher masses, leptonic decay channels, $S \to e^+e^-$ and eventually $S \to \mu^+\mu^-$ open up. These are more straightforward, with the decay rate given by[212]:

$$\Gamma(S \to l\bar{l}) = \frac{\theta^2 m_l^2}{8\pi v^2} m_S \left(1 - \frac{4m_l^2}{m_S^2}\right)^{3/2} \tag{4.7}$$

where l is just the lepton in question and v is the Higgs vaccuum expectation value.

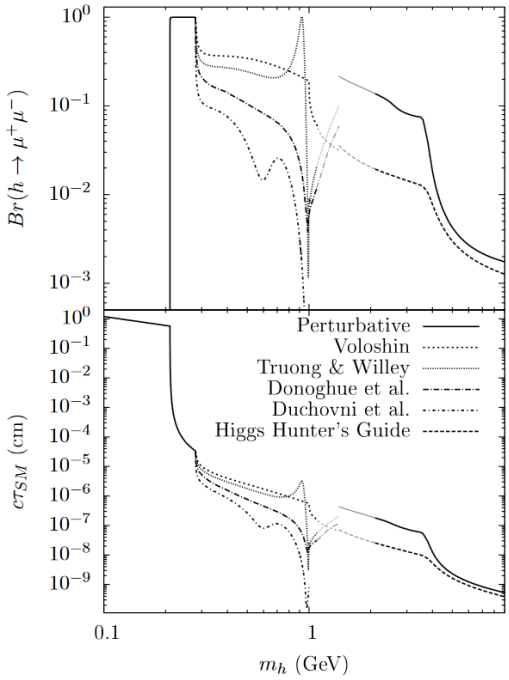

Figure 4.3: *Branching ratios for decay to muons (top) and lifetime (bottom) of a Higgs-like scalar ρ with $\theta = 1$. Comparisons between different works are shown(Voloshin[249], Truong and Willey[250], Donoghue[251], Duchovni[252] and the Higgs Hunters' Guide[253]), showing the range of uncertainty. Image from [247]*

However, the decay from S in the mass range $2m_\pi \lesssim m_S \lesssim 4$ GeV is subject to significant theoretical uncertainty[246, 247, 254, 255]. As can be seen in Figure 4.3, around 1 GeV, different models differ by as much as multiple orders of magnitude. The reason for this is the breakdown of different perturbative schemes. At low energies (well below $\Lambda_\chi \sim 1$ GeV, the chrial symmetry breaking scale), Chiral Perturbation Theory can be effectively used to find the pion interaction (a general description of the methods is given in [256]), but this fails near Λ_χ. Then, at high energies ($m_S > 2.5$ GeV), quark-gluon perturbative results are applicable. In between these regimes, dispersion relations can be matched to the low-energy results, but for $m_S > 1$ GeV, this becomes questionable, due to the lack of experimental data on high-energy meson scattering and the uncertain contributions of scalar hadronic resonances[246]. A detailed review

of the methods of computation and their uncertainties is given in [254].

In order to avoid most of the issues associated with this uncertainty, we restrict ourselves to masses $m_S < 1$ GeV, and then use the baseline lifetime and pionic decay rates presented in [212], which uses data from the $\pi\pi$ phase-shift analysis from [257] for $m_S > 600$ MeV. This lifetime graph for a particular value of $\theta = 10^{-6}$ is seen in Figure 4.4. Note that for all decay rates, we have $\Gamma_S \propto \theta^2$, because from "Fermi's Golden Rule", we know that $\Gamma \propto |\mathcal{M}|^2$, where $\mathcal{M}$ is the matrix element corresponding to the process. All interactions of S with the SM go through the mixing, so $\mathcal{M} \propto \theta$. This way, we can easily find the lifetimes for general values of θ.

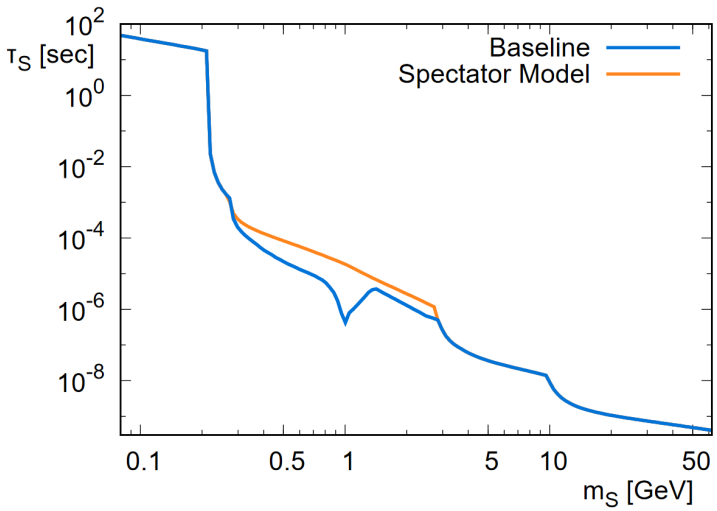

Figure 4.4: *The baseline and spectator model curves of the lifetime of a scalar S. The latter uses low-energy theorems for the pion decays until the c threshold and scales kaon and η meson decays appropriately. Shown for $\theta = 10^{-6}$. We use the baseline results up until $m_S = 1$ GeV. Figure from [212]*

4.2 Production in Early Universe

4.2.1 Freeze-out Yield

First we consider the case of complete thermalisation with the SM sector. This does require relatively strong coupling ($\theta > \theta_{\text{thermal}} \sim 10^{-6}$)[66]. It will be convenient to describe the amount of S in terms of the abundance: $Y_S \equiv n_S/\tilde{s}$, where n_S is the S number density and $\tilde{s}$ is the entropy density

of the universe. This abundance will remain constant through the expansion, because the $\tilde{s}$ scales in the same way as the number density (both remain constant in a comoving volume).
In the thermalised case, the abundance of S is maintained at its relativistic equilibrium value:

$$Y_S^{\text{eq}} = \frac{n_S^{\text{eq}}}{\tilde{s}} = \frac{45\zeta(3)}{2\pi^4 g_*} \simeq \frac{0.28}{g_*} \tag{4.8}$$

where we used the relativistic number denstiy for a boson (with one degree of freedom): $n(T) = (\zeta(3)/\pi^2)T^3$ and the entropy density $\tilde{s}(T) = (2\pi^2/45)g_* T^3$ [102].
The abundance will remain at this equilibrium value until either: it becomes inefficient due to the expansion, in which case S will decouple with the abundance (4.8); or the temperature cools down to below m_S and S becomes non-relativistic. As it turns out, the latter case does not occur for our mass range $m_S < 1$ GeV, because S interacts primarily with the heaviest particles (t, W, Z and h), which become non-relativistic well before S does. At that point, the efficiency of S production is exponentially decreased, so S freezes out with the abundance given by (4.8)[66]. At freeze-out, as we know this happens at $T \gg m_S$, we have $g_* = 61.75 - 106.75$ [121]. For conservative results, we assume the least abundance, so we take the $g_* = 106.75$ case, and arrive at $Y_S^{\text{eq}} \approx 0.025$.

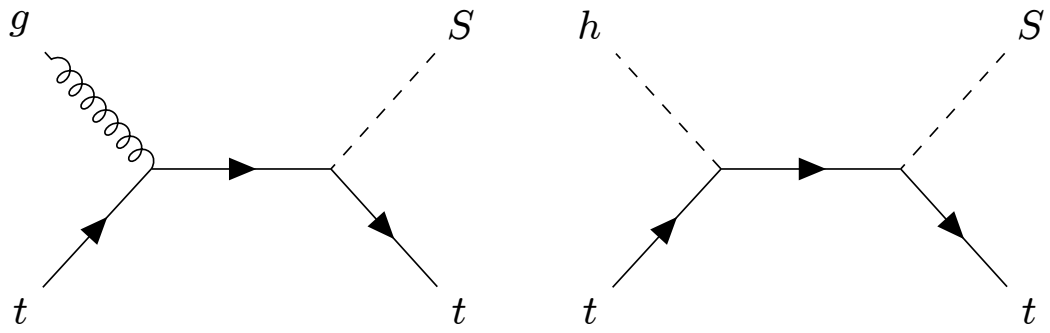

(a) *QCD production type diagram.* ***(b)*** *Compton-like scattering diagram.*

Figure 4.5: *Two examples of production processes for S, both of which show a heavy quark propagator.*

Actually, it is not quite a trivial matter that production of S is saturated around the electro-weak scale ($\sim$ 100 GeV). Indeed, the heaviest particles with the largest Yukawa couplings couple strongest to S, which seems to

imply that high-temperature production dominates. Two such dominating producting channels are shown in Figure 4.5. However, largeness of the Yukawa couplings may be compensated by the mass term in the denominator of the propagator. A large mass term in the progagator will surpress the production channel, and since all of these propagators are those of very massive particles, this could cancel out the effect of large Yukawa couplings.

However, this is resolved if we consider that this takes place in a very hot bath. As such, the masses in the propagators are replaces by the effective thermal masses, because particle interactions are screened by thermal excitations. This becomes especially relevant near the thermal mass. Notably, the Higgs boson is affected by this, which results in a change of $v(T)$. We will discuss this below, but for now it suffices to know that all SM particles get a thermal mass of the form $m_T \propto T$, with constants of proportionality of order $\mathcal{O}(0.1)$ [258]. This means the effect of the propagator is similar for all particles, and since the Yukawa couplings still dictate the interaction with S, indeed its production is dominated by high temperatures.

4.2.2 Freeze-in Yield

The other possibility is that the coupling is so weak that S never thermalises with the SM, and so gradually more S is produced during the electr-weak temperatures, until the production becomes insignificant. This is called "freeze-in" to constrast the regular freeze-out paradigm. This occurs for $\theta < \theta_{\text{thermal}}$.

We note here that there is no expected significant production coming from oscillation from the Higgs boson, nor inverse decay ($2 \to 1$) processes, because of the relative smallness of m_S. This is confirmed by analysis in [66]. Thus, we consider $2 \to 2$ channels, mainly consisting of the heaviest particles.

Taking the processes $X + Y \to Z + S$, we can do a rough estimate of the freeze-in yield using the total production interaction rate $\Gamma_X = n_Y \langle \sigma v \rangle$, with n_Y the number density of initial particle Y and $\langle \sigma v \rangle$ the thermally averaged cross-section for the process. Since we are approximating all production processes, with different cross-sections, we will simply estimate the dependence of the total cross-section with a qualitative argu-

ment: we know the cross-section scales as $|\mathcal{M}|^2$, so we expect the scaling $\langle\sigma v\rangle \propto \theta^2 y_X^2$ (with y_X the Yukawa coupling of species X). Then, from dimensional arguments, we add a temperature dependence (which follows the $\langle\sigma v\rangle \propto 1/s$ present in all processes [66], where s is the Mandelstam variable) $\langle\sigma v\rangle \sim y_X^2\theta^2/T^2$. Then, taking $n_Y \sim T^3$, we have $\Gamma_X \sim \theta^2 y_X^2 T$, though we stress that there is no reason to assume that the constant of proportionality is of order $\mathcal{O}(1)$.

Then we can find the yield using the Boltzmann equation:

$$\dot{n_S} + 3Hn_S = \tilde{s}\dot{Y_S} = \int \sum_{i=1}^{4} \left(\frac{\mathrm{d}^3 p_i}{2E_i(2\pi)^3}\right) f_1 f_2 (1 \pm f_3)(1 \pm f_4)|\mathcal{M}|^2 (2\pi)^4 \delta^{(4)}(p_1 + p_2 - p_3 - p_4) \tag{4.9}$$

where f_i the distibution function of i.

We also have a relation between the last part of (4.9) and Γ_X: we can also write:

$$\Gamma_X = n_Y \langle\sigma v\rangle = n_Y \frac{1}{2m_X 2E_Y} \int \mathrm{d}\Pi_Z \mathrm{d}\Pi_S |\mathcal{M}|^2 (2\pi)^2 \delta^{(4)}(p_X + p_Y - p_Z - p_S)$$

where $\mathrm{d}\Pi_i = \frac{\mathrm{d}^3 p_i}{2E_i(2\pi)^3}$. Using a Boltzmann approximation for the distibution functions f_Z and f_S, we can fill this in (4.9):

$$\tilde{s}\dot{Y_S} = \int \mathrm{d}\Pi_X \mathrm{d}\Pi_Y \frac{2m_X 2E_Y f_X f_Y \Gamma_X}{n_Y} = \frac{2m_X \Gamma_X}{n_Y} \int \frac{\mathrm{d}^3 p_Y}{(2\pi)^3} f_Y \int \frac{\mathrm{d}^3 p_X}{(2\pi)^3 2E_x} f_X$$

The first integral is exactly the number density (with a factor g_Y the degrees of freedom), and the second integral:

$$\int \frac{\mathrm{d}^3 p_X}{(2\pi)^3 2E_x} f_X = g_X \int_{m_X}^{\infty} \frac{\sqrt{E_X^2 - m_X^2}}{4\pi^2} e^{-E_X/T} \mathrm{d}E_X = \frac{g_X m_X T}{4\pi^2} K_1\left(\frac{m_X}{T}\right)$$

where $K_1(x)$ is the modified Bessel function of the second kind.
All together, we find:

$$\tilde{s}\dot{Y_S} \approx \frac{g_X g_Y m_X^2 \Gamma_X T K_1(m_X/T)}{2\pi^2}$$

Version of July 22, 2021– Created July 22, 2021 - 14:39

with $g_{X,Y}$ the degrees of freedom of X and Y, Γ_X the total interaction rate. Taking the standard time-temperture relation $\mathrm{d}t/\mathrm{d}T = -M^*_{Pl}/T^3$, we can integrate this function to find:

$$\begin{aligned} Y_S &\approx \frac{45 M_* g_X g_Y m_X^2 y_X^2 \theta^2}{4\pi^4 g_*} \int_0^{T_W} \frac{\mathrm{d}T}{T^4} K_1(\frac{m_X}{T}) \\ &\approx \frac{45 M_* g_X g_Y m_X^2 y_X^2 \theta^2}{4\pi^4 g_*} \left(\frac{m_X}{T_W}\right)^2 \frac{1}{m_X^3} K_2(\frac{m_X}{T_W}) \end{aligned} \tag{4.10}$$

where $T_W \approx 160$ GeV is the temperature of electro-weak symmetry breaking. When we fill in some values: using $g_* = 106.75$ as the very high temperature value and taking t for both X and Y for the dominant production channels, with $m_t = 172.76$ GeV, $y_t \approx 1$, and $g_t = 6$ (3 for the colour charge, 2 for the spin) we find:

$$Y_S \sim \frac{36 \cdot 45 M_{Pl} y_t^2 \theta^2}{4\pi^4 \cdot 1.66 g_*^{3/2} m_t} \left(\frac{m_t}{T_W}\right)^2 K_2(\frac{m_t}{T_W}) \sim 10^{14}\theta^2$$

Now, as we will see momentarily, this is a significant overestimation. One of the major factors in this is the possible prefactors. From the cross-sections per process given in [66], while most channels do indeed scale as $\langle \sigma v \rangle \propto y_X^2 \theta^2 / T^2$, there is a a prefactor of order $\mathcal{O}(0.1 - 0.01)$ for all of them, so this could account for some overestimation.

In addition, we have neglegted here to account for thermal effects. As mentioned, all particles develop an effective thermal mass term due to screening of interactions from thermal excitations. In the case of the Higgs, the mass amounts to $m_{h,T}^2(T) = c_h T^2$, with $c_h = (8\lambda_h + 4y_t^2 + 3g_W^2 + g_Y^2)/16 \approx 0.425$ [258]. Adding this term to the original Lagrangian changes the potential of the Higgs:

$$V(H) = (-\mu^2 + c_h T^2)|H|^2 + \lambda_h |H|^4$$

where μ and λ_h are the normal Higgs parameters for the mass and quartic couplings. This gives rise to a new potential minimum, and since normally this is given by $v = \mu^2/\lambda$, we redefine $v(T)$:

$$v^2(T) = \frac{\mu^2}{\lambda_h} - \frac{c_h T^2}{\lambda_h} = v_0^2 - \frac{c_h T^2}{\lambda_h}$$

And this new, thermal $v(T)$ approaches 0 as the temperature increases. The effective Higgs mass now becomes $m_h^2 = 2(\mu^2 - c_h T^2) = 2\lambda_h v^2(T)$.

This effect changes not just the Higgs mass, but the new thermal expectation value $v(T)$ also changes the SM particle masses, which are defined as $m_p = y_p v$, where p is the particle and y_p is its Yukawa coupling. In addition, the mixing angle is adapted. Naively, we would expect to find:

$$\theta(T) = \frac{Av(T)}{m_h^2(T) - m_S^2} \tag{4.11}$$

However, this expression suffers from a divergence at $m_h(T) = m_S$. This is resolved by consideration of not just the "bare" mass mixing in the Lagrangian, but also the thermal vacuum polarization.
The S self-energy is given by:

$$\Pi_S(k) = \frac{\alpha_1^2 v^2(T)}{k^2 - m_0^2(v) - \Pi_h(k)}$$

where Π_h is the thermal Higgs self energy, with $\mathrm{Re}\Pi_h = c_h T^2$ the Higgs thermal mass.
Then, in the on-shell limit:

$$\theta_{eff}^2 \equiv \Gamma_S/\Gamma_h = \frac{\alpha_1^2 v^2(T)}{(m_h^2(T) - m_S^2)^2 + (E\Gamma_h)^2}$$

where Γ_h is the Higgs width.
We can represent this diagrammatically as well: instead of only considering direct mixing (as portrayed in Figure 4.1), now we include thermal loops in the definition of the mixing angle, like we see in Figure 4.6.

Note that this Higgs width Γ_h is very different from the zero-temperature width. At high temperatures, Γ includes both decay and inverse decay processes, acting more like an equilibrium rate. In the regime of interest (around electro-weak temperatures), $\Gamma_h(T) \propto T$ and $\Gamma_h(T) \gg \Gamma_h(0) \approx 4$ MeV [66, 258]. Thus, the high-temperature behaviour of the effective thermal mixing angle is $\theta_{eff} \sim Av(T)/T^2$, which becomes quite small, due to the temperature-dependence of $v(T)$. Thus, this effect may account for part of the over-estimation of the freeze-in yield.

Fradette *et al.* have carefully considered each production mode and solved the Boltzmann equation to find the contribution from all channels individually. Additionally, production in the electro-weak symmetric phase is considered. In this case, there is no non-zero Higgs vacuum expectation value, so there is no mass mixing between the Higga and S,

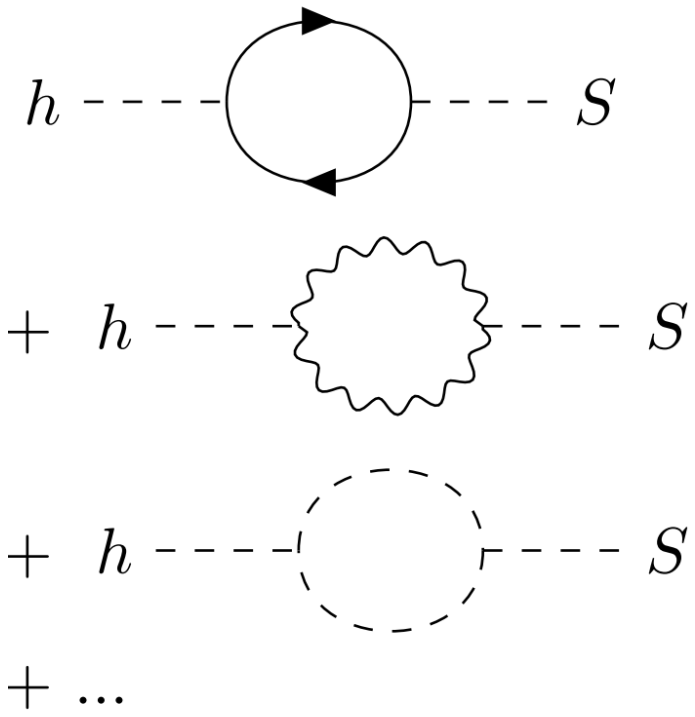

Figure 4.6: *Examples of one-loop processes in production of S from h, including fermionic and bosonic loops. Of course, S interaction with the SM always goes via mixing with h, so the additional loop contribution comes from the thermal Higgs self-energy.*

(the Lagrangian is still just (4.1)) which means the only way to produce S is through H explicitly. This greatly reduces the possible production channels, so the contribution to the total yield is relatively small.
Adding it all together, we have a total freeze-in yield of [66]:

$$Y_S \approx 2.8 - 5.2 \times 10^{11}\theta^2 \tag{4.12}$$

We will take a central value $Y_S = 4 \times 10^{11}\theta^2$.
Note that, while this does depend on θ as we expect (due to the $|\mathcal{M}|^2$ in the production interaction), there is no dependence on mass. However, we would also expect this, since the production dominantly happens around the electro-weak temperatures ($\gg m_S$)[i]. There is of course an implicit dependence on the mass: if m_S becomes larger, the assumptions made start to no longer hold, and an alternative expression must be found. In particular, for $m_S \sim 15 - 20$ GeV, the resonance with the Higgs start to become

[i] This is not ubiquitously true, as we will see in the next chapter.

important, due to the thermally adapted Higgs mass dropping down to these numbers around the electro-weak temperatures [66].

In the following constraints, we assume at the time of the cosmological effects of S, the production has ceased and settled on either (4.8) or (4.12), whichever is higher (since freeze-in production can never be larger than the thermalised abundance). Then, we describe $n_S(T) = Y_S \tilde{s}(T)$ and $\rho_S = m_S n_S$ (where we take the non-relativistic expression, which will be valid for the mass ranges and temperatures we consider for each constraint).

4.3 Experimental Limits

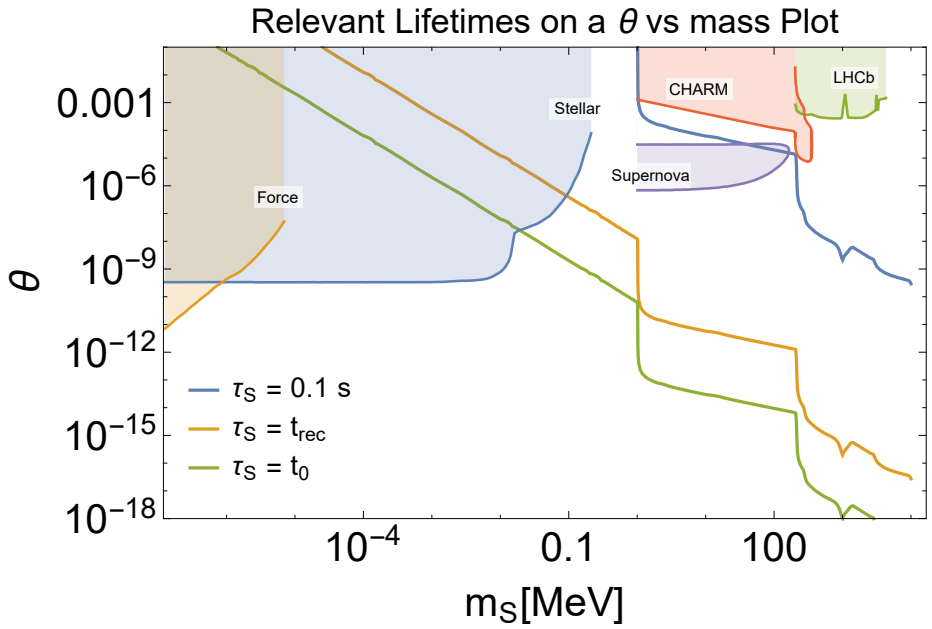

Figure 4.7: *Overview of experimental progress in constraining the parameter space of the scalar S. Includes constraints from short-range forces (Force)[259, 260], stellar cooling (Stellar)[261], supernova SN1987a (Supernova)[262, 263], beam dump experiment from the CHARM collaboration (CHARM)[255, 264] and direct search from the LHCb collaboration (LHCb)[265]. Included are curves of the lifetimes relevant for obeserved effects: 0.1 s for BBN, $t_{rec} \sim 10^{13}$ s for CMB constraints and $t_0 \sim 5 \cdot 10^{17}$ s for X-ray constraints.*

Figure 4.7 summarizes some of the main experimental constraints on the scalar parameter space. We briefly describe these constraints here. By no means is this an exhaustive list. For a more complete description of

Version of July 22, 2021– Created July 22, 2021 - 14:39

experimental status, see for example [266].

Force

Introducing a new light scalar or vector particle is expected to generate a Yukawa potential between bodies at small distances, through the exchange of these bosons [267]. This would modify the gravitational inverse square law with a Yukawa term [259, 260]:

$$V(r) == G\frac{m_1 m_2}{r}\left(1 + \alpha e^{-r/\lambda}\right)$$

where G is the gravitational constant, and the new interaction parameters are the stength α and the range λ.
These parameters are now stongly constrained, which in turn limits the possibility of a very light scalar S [259, 260].

Stellar Cooling

A new light particle (mass $\lesssim 100$ MeV) will be produced in the hot plasma in supernovae and stellar cores. As such, it will contribute in energy transport.
Though this type of constraint is typically called "stellar cooling", it more accurately refers to anomalous energy loss. The lack of this anomalous energy transportcan be used to constrain the couplings of these new particles to the SM particles that make up the start [268].

In particular, a Higgs-like scalar will mix with plasmons in the star. For masses below the plasma characteristic frequency, resonant production can occur. This leads to very stringent constraints on new scalars with small masses [261].

Supernova

A light, weakly coupled scalar will be produced in supernovae, and contribute to its energy loss. This will shorten the duration of the observed neutrino pulse emitted from core collapse. Specifically, the neutrino signal from SN1987a has been used to constrain axion-like particles [262] and scalars [263].

CHARM

If there are light scalars, they would be most efficiently produced by decay of B and K mesons. This is still very unlikely, so many events would be required to produce even a small signal. The beam dump experiment by the CHARM collaboration [264] shoots a proton beam on a fixed, thick target, producing the mesons in copious amounts.

Subsequent analysis of the CHARM data has found no scalar signal, which is used to constrain the parameters of said scalar [255].

LHCb

A direct search for scalar particles in $B^+ \to K^+ + S$, with subsequent scalar decay to muons, from the LHCb collaboration yielded an upper limit on the branching ratio of B decay to scalars [265]. This is then translated into a constraint on the parameters of the particles, be it τ_S or θ.

4.4 Results

We will directly compare our results with Fradette *et al.* [66], since the same system and the same types of constraints are used. For the X-ray and spectral distortion bounds, we expect no difference, but for the N_{eff} and BBN bounds, Fradette *et al.* used numerical solutions to the Boltzmann equations, which are computationally intesive. Our semi-analytic bounds rely on some approximations, and thus we expect there to be some difference. We will present all bounds in terms of τ_S for ease of visibility of the cosmological times associated with them. Some jittering in the curves from Fradette *et al.* comes from the inexact data extraction, but the features of the plots should still be clearly visible.

4.4.1 X-ray

Figure 4.8 shows the comparison of the constraints from X-rays, both in terms of θ and τ_S. In the left graph, included are the original constraints as derived by Essig *et al.* [195]. This bound considers the scalar S as the source of all dark matter, which puts stronger constraints on θ, but requires a larger abundance of S than we see from primordial production. Adjusting the density yields the other bound, which overlaps with that of

Fradette *et al.*.

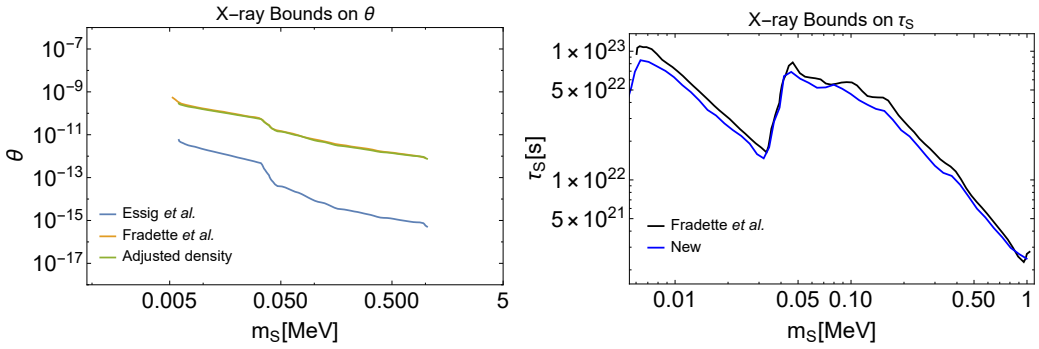

(a) ***(b)***

Figure 4.8: *Constraints from X-ray signal production in terms of mixing angle (a) and lifetime (b). The curves represent an upper bound in θ, and a lower bound in τ_S. Comparison is made with Essig et al. [195] and Fradette et al. [66]. "Adjusted density" and "New" are the same curves.*

This is the upper limit of the excluded range in terms of τ_S (the lower limit in terms of θ).

We consider the excluded region to extend down to t_0, the current age of the universe, since decays before that time cannot be detected now. Note that this does not mean that $\tau_S = t_0$ is the lower limit, because depending on the the abundance and mass, a measureable signal detected at time t_0 may be originating from particles with lifetimes less or more than t_0. Only the lifetimes for which the amount of detectable decay events at t_0 exceeds the experimental limits are excluded. This is calculated in the exact same way as the rescaled upper limit. The full range of excluded parameter space will be included in the final plot.

4.4.2 Spectral Distortions

We will first rewrite (3.3) into a more tractable form, using (3.5). For the y-paramter:

$$\begin{aligned} y &= \frac{1}{4}\int_{t(z_{\mu y})}^{t(z_{rec})} \frac{m_S Y_S \tilde{s} e^{-t/\tau_S} Br_{EM}}{\rho_\gamma \tau_S} \mathrm{d}t \\ &= \frac{1}{4}\int_{t(z_{\mu y})}^{t(z_{rec})} \frac{m_S Y_S}{\tau_S}\frac{\tilde{s}_0}{\rho_{\gamma 0}}\sqrt{\frac{t}{t_0}} e^{t/\tau_S} Br_{EM} \\ &= \frac{1}{4} m_S Y_S Br_{EM}\frac{\tilde{s}_0}{\rho_{\gamma 0}}\sqrt{\frac{\tau_S}{t_0}}\int_{\frac{t_0}{\tau_S z_{\mu y}^2}}^{\frac{t_0}{\tau_S z_{rec}^2}} \sqrt{\xi} e^{-\xi}\mathrm{d}\xi \end{aligned}$$

where we used $\tilde{s} \propto T^3 t^{-3/2}$ and $\rho_\gamma \propto T^4 \propto t^{-2}$ to write $\tilde{s} = \tilde{s}_0 (t_0/t)^{3/2}$ and $\rho_\gamma = \rho_{\gamma 0}(t_0/t)^2$, with t_0 the normalisation time-scale. In the last line we used the substitution $\xi = t/\tau_S$, and for the integration boundaries, we used $t = t_0/(z+1)^2 \approx t_0/z^2$. $\tilde{s}_0 = 2891\mathrm{cm}^{-3}$ is the current-day entropy density and $\rho_{\gamma 0} = 0.26\mathrm{eVcm}^{-3}$ the current photon energy density[66]. However, t_0 is not the current-day age of the universe. Instead, t_0 must compensate for the fact that the universe underwent an evolution, and stopped being radiation dominated at some point, which the other quantities assume. We can find t_0 by using the evolution of ρ_γ as we have just defined it:

$$\begin{aligned} \rho_\gamma = \rho_{\gamma 0}\left(\frac{t_0}{t}\right)^2 = \frac{\pi^2}{15}T^4 = \frac{\pi^2}{15}\frac{1}{g_*}\left(\frac{M_{Pl}}{2\cdot 1.66 t}\right)^2 \\ t_0 = \sqrt{\frac{\pi^2}{15}}\frac{1}{\sqrt{g_*}}\frac{M_{Pl}}{2\cdot 1.66}\frac{1}{\sqrt{\rho_{\gamma 0}}} = 2.4\times 10^1 9\mathrm{s} \end{aligned}$$

where we used $g_* = 3.36$, since this all takes place well after neutrino decoupling.
We can do exactly the same process for the μ-parameter, and arrive at:

$$\mu = 1.401 Y_S m_S \frac{\tilde{s}_0 Br_{EM}}{\rho_{\gamma 0}}\int_0^{\frac{t_0}{z_{\mu y}^2}} \sqrt{\frac{t}{t_0}} e^{-\Gamma_S t}\cdot e^{-(z_\mu^2 t/t_0)^{-5/4}}\mathrm{d}t$$

Here, we did not substitute ξ in the last equation, as we cannot get all factors of τ_S out of the integral regardless, and it would become exceedingly messy. We can now simply do these calculations and require the conditions set by the experimental values of μ and y.

Version of July 22, 2021– Created July 22, 2021 - 14:39

Figure 4.8 shows these constraints from spectral distortions in terms of τ_S, for both the μ-type distortions and y-type distortions. Fradette *et al.* do not show the full range of the excluded parameter space for masses below $2m_e$, but from the agreement between the constraints from what we can see, we assume full congruency. Since there is some overlap between the constraints from μ- and y-distortions, the combined bounds can exclude a large range of parameter space.

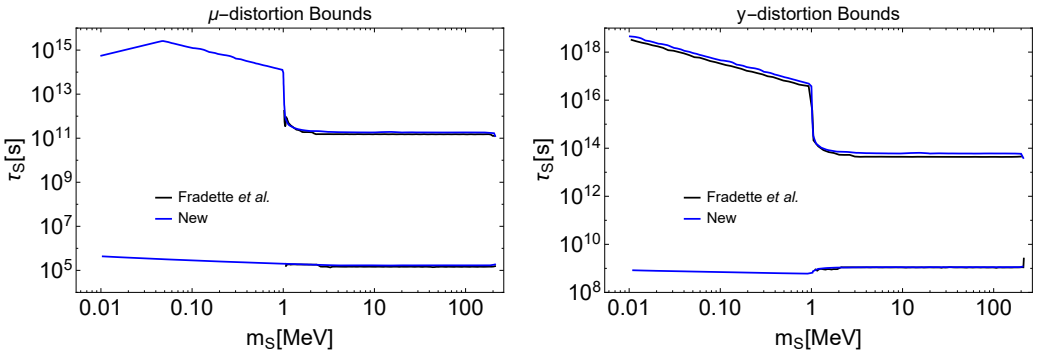

(a) ***(b)***

Figure 4.9: *Upper and lower bounds from spectral distortions: μ-type distortion (a) and y-type distortion (b). A comparison with Fradette et al. [66] is made where possible.*

4.4.3 N_{eff}

Before we apply our formulae, we will compare the energy density of the S sector with the radiation energy density:

$$\frac{\rho_S}{\rho_{rad}} = \frac{m_S n_S}{\frac{\pi^2}{30} g_* T^4} = \frac{4}{3}\frac{m_S Y_S}{T} e^{-t/\tau_S} \tag{4.13}$$

Note that this is a rough approximation, only valid in the regime where $\rho_S/\rho_{rad} \ll 1$, but we can use it to estimate the region of parameter space where ρ_S starts to become relevant. Using the standard time-temperature relation $t = M_{Pl}^*/(2T^2)$, we find a maximum of this expression at $T = T_{\max} = \sqrt{M_{Pl}^*/\tau_S}$ or $t = t_{\max} = \tau_S/2$. This point is to be expected, because earlier, the radiation energy density (scaling as $\rho_{rad} \propto T^4$) decreases faster than the S energy density (scaling as $\rho_S \propto T^3$). However, this stops when S starts to decay in great numbers, decreasing exponentially, at which point ρ_{rad} takes over again.

Version of July 22, 2021– Created July 22, 2021 - 14:39

Substituting T_{max} into (4.13), with $g_* = 3.36$ (since T_{max} is well below 1 MeV in the relevant regime), we can find our region of significant ρ_S:

$$\left.\frac{\rho_S}{\rho_{rad}}\right|_{T_{max}} \approx 0.7 Y_S \left(\frac{m_S}{1\text{MeV}}\right) \sqrt{\frac{\tau_S}{1\text{s}}} \gtrsim 1$$

This region is shown in Figure 4.10.

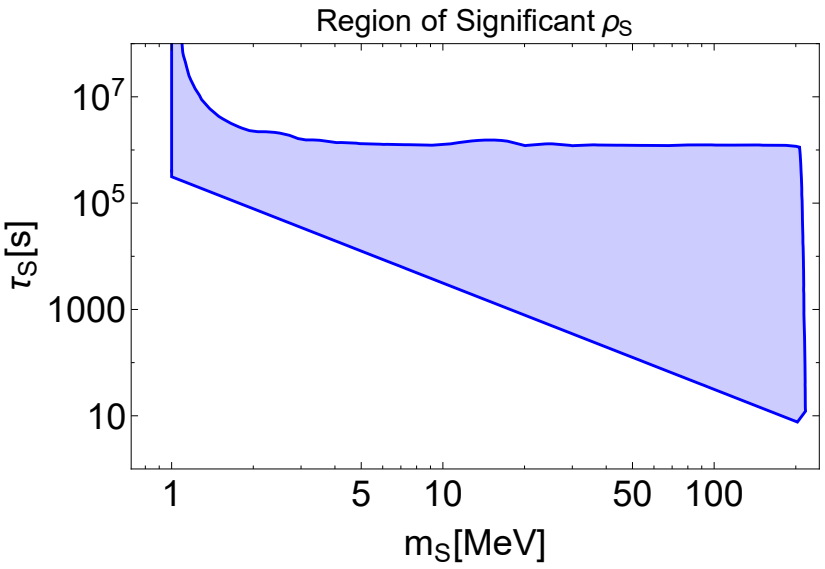

Figure 4.10: *Region of parameter space where $\rho_S \gtrsim \rho_{rad}$ in terms of τ_S and m_S. For higher masses, the lifetime starts to drop dramatically, due to new decays opening up.*

We will first show the results from our numerical description. In Figure 4.11 we show these bounds. We can notice that these bounds show qualitatively the same features, with the exception of the high mass, low lifetime part of the lower boundary. Here we see the curve from Fradette *et al.* bend upwards, while the new results cut through. Since in this regime decay happens quite shortly after neutrino decoupling, we can assume this is caused by decoupling effects, which are taken into account by [212], which is where the early-time bounds from Fradette *et al.* are taken from.

In addition, we can notice that the new constraints are weaker than those from Fradette *et al.*. This is because they used a stonger constraint on $N_{eff} = 3.04 \pm 0.33$, from Planck 2015 [185]. We point out that this constraint assumes SBBN, and is thus less broadly applicable than the values

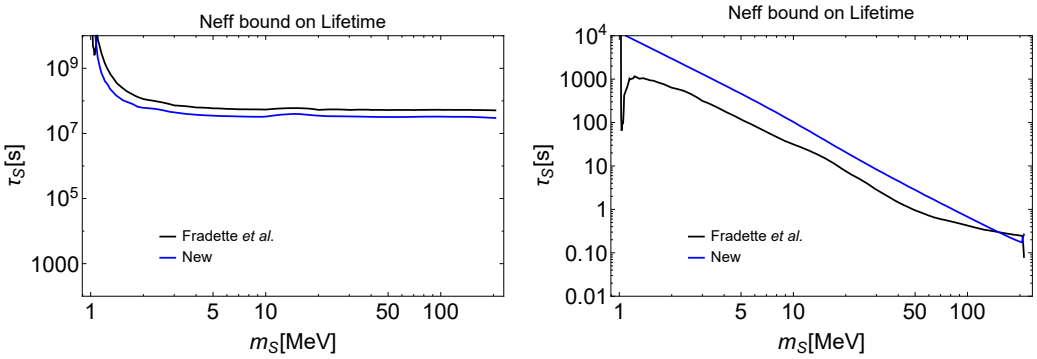

(a) ***(b)***

Figure 4.11: *Upper (a) and lower (b) bounds on the S lifetime from N_{eff}. These constraints are somewhat weaker than those from Fradette et al. [66], owing to the different range of N_{eff} used (see text). Here, we use $N_{eff} > 2.56$*

of N_{eff} we consider. We show the results of our bounds, assuming this stronger constraint, in Figure 4.12. Here, we see good agreement between the curves, at the very least within the uncertainty range of Y_S.

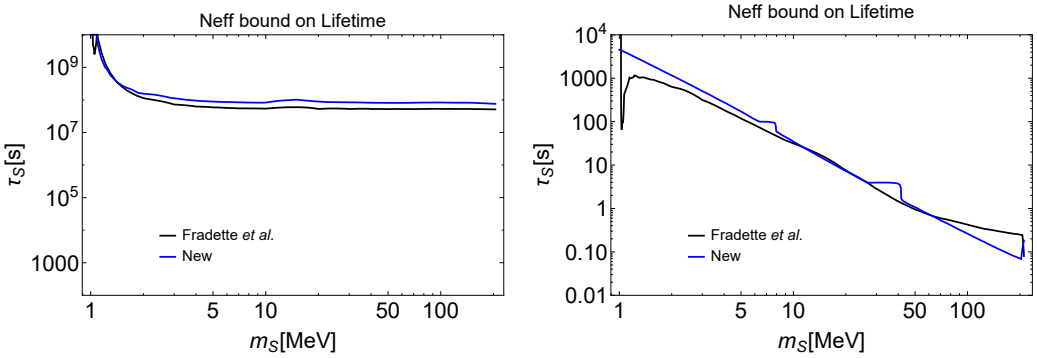

(a) $y = x$ ***(b)*** $y = 3sinx$

Figure 4.12: *Same as Figure 4.11, except we use the same range of N_{eff} as Fradette et al., namely $N_{eff} > 2.71$. The strange bumps in the lower bound are artefacts of the numerical analysis, and will disappear when more detail is used to obtain the curve.*

Finally, we will show the excluded region we get from a simple application of the formula in (3.6). We can note that, since we consider only decay to electromagnetic particles (e^+e^- and $\gamma\gamma$), $Br_{EM} = 1$. As such, N_{eff} can only decrease as a result of S, so we use th lower bound $N_{eff} > 2.56$.

Then, we can rewrite (3.6):

$$N_{eff} = \frac{8}{7}\left(\frac{11}{4}\right)^{4/3}\frac{\rho_\nu^{SM}}{\rho_{EM}^{SM}+\rho_S} < 2.56$$
$$\frac{1}{2.56}\frac{8}{7}\left(\frac{11}{4}\right)^{4/3}\frac{\rho_\nu^{SM}}{\rho_S} < \frac{\rho_{EM}^{SM}}{\rho_S}+1$$
$$1 > \frac{\rho_{EM}^{SM}}{\rho_S}\left(\frac{3}{2.56}-1\right) = \frac{2}{g_*^{SM}}\left(\frac{3}{2.56}-1\right)\frac{\rho_{rad}}{\rho}$$
$$\frac{\rho_S}{\rho_{rad}} > \frac{2}{g_*^{SM}}\left(\frac{3}{2.56}-1\right) \approx 0.1$$

where we used $\rho_\nu^{SM} = 3(7/8)(4/11)^{4/3}\rho_{EM}^{SM}$ and $g_*^{SM} = 3.36$.
As we can see, N_{eff} constrains the density ratio from (4.13) to be smaller than ≈ 0.1. Since (3.6) assumes instantaneous decay, and the densities are evaluated right before this decay happens, the strongest constraints come from this comparison at $T_{\max}$.

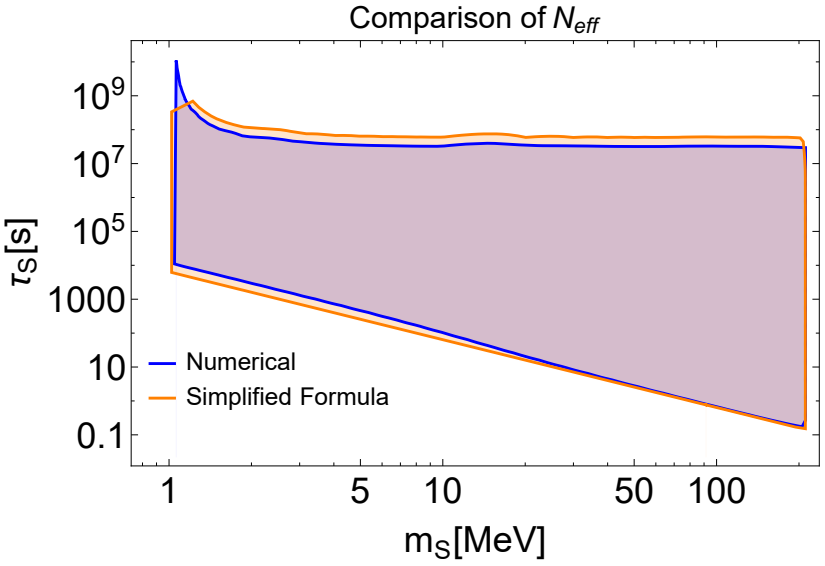

Figure 4.13: *Excluded region of S parameter space from our numerical description of the system and the simplified formula (3.6). In the latter case, time is taken at $t = t_{\max} = \tau_S/2$, so that ρ_S/ρ_{rad} is largest.*

These "stongest constraints" are shown in Figure 4.13 in comparison with the constraints we found earlier from our numerial considerations. It seems that the simplified formula actually overestimates the strength

of the N_{eff} constraint. The physical reason for this is such: the simplified formula assumes instantaneous decay. At $t = t_{\max} = \tau_S/2$, though the energy density is relatively largest, already $1 - \exp(-1/2) \approx 40\%$ of the S particles have decayed. Therefore, at this time, there should already be a significant injection of energy in the SM baths (photon bath, in this case). But the simplified formula takes the SM baths as they were *before* any injection. Thus, this method underestimates the SM baths, and so it overestimates the effect of S on N_{eff}.

One solution is to simply take the values at an earlier time, such that the approximation of instantaneous decay is more accurate. As it turns out, we find a nice agreement between the numerics and the formula, if we take $t = \tau_S/10$, which is also the value used in [66]. The comparison is shown in Figure 4.14, and now we find a much better agreement. In addition, we see a small deviation in the high-mass, low-lifetime corner, like we saw in the comparisons with Fradette *et al.*. This indicates that this simplified formula may actually be more accurate in that regime, likely per chance.

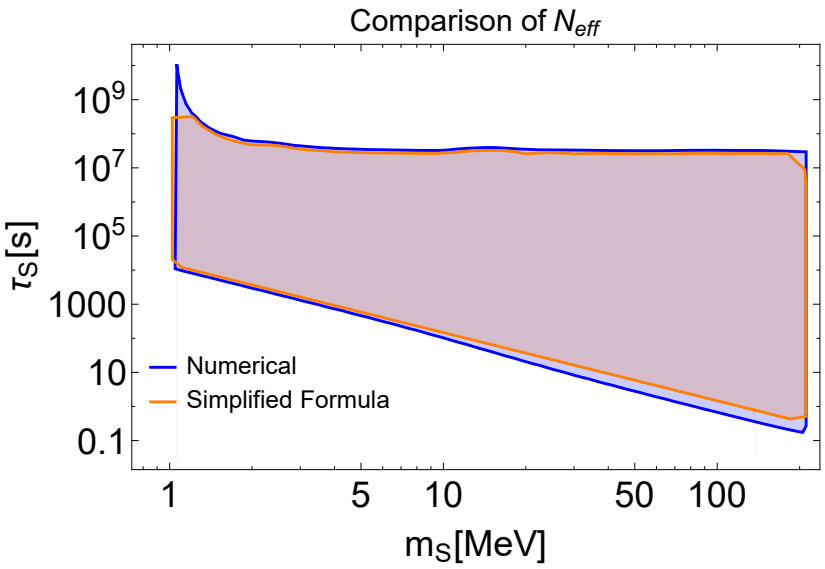

Figure 4.14: *Same as Figure 4.13, except the simplified formula is applied at a time $t = \tau_S/10$.*

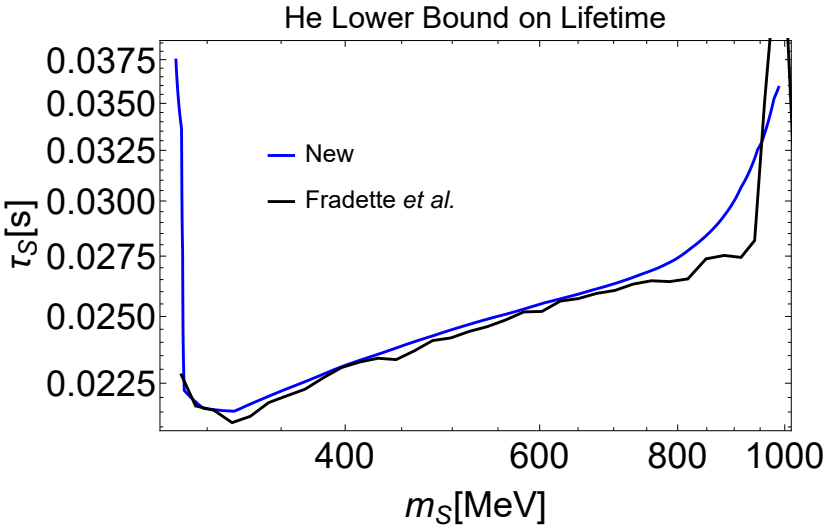

Figure 4.15: *Comparison between our upper bound (meaning the lifetime is less than this) and the bound as given by Fradette et al.. The jittery behaviour in the latter bound is not intrinsic, but an artefact produced by data extraction.*

4.4.4 BBN

The application of (3.11) is not directly obvious, so we present some short calculations first. We can rewrite:

$$\left(\frac{a_{dec}}{a}\right)^3 \frac{n_S^{dec}}{n_\gamma(T_0^{min})} = \frac{n_S^{dec}}{n_\gamma(T_{dec})} \left(\frac{a_{dec}T_{dec}}{a_0 T_0^{min}}\right)^3$$

Then we can write:

$$\frac{n_S^{dec}}{n_\gamma(T_{dec})} = \frac{Y_S g_*^{dec} \frac{2\pi^2}{45} T^3)dec}{\frac{2\zeta(3)}{\pi^2} T_{dec}^3} = \frac{\pi^4 Y_S g_*^{dec}}{45\zeta(3)}$$

and since all SM particles are in local equilibrium at $T \gtrsim 1$ MeV:

$$\left(\frac{a_{dec}T_{dec}}{a_0 T_0^{min}}\right)^3 = \frac{g_*^0}{g_*^{dec}}$$

It is then straightforward to find the constraint from helium overproduction.

Figure 4.15 shows the comparison of these constraints. Considering that Fradette *et al.* used a detailed numerical calculation scheme solving

Version of July 22, 2021– Created July 22, 2021 - 14:39

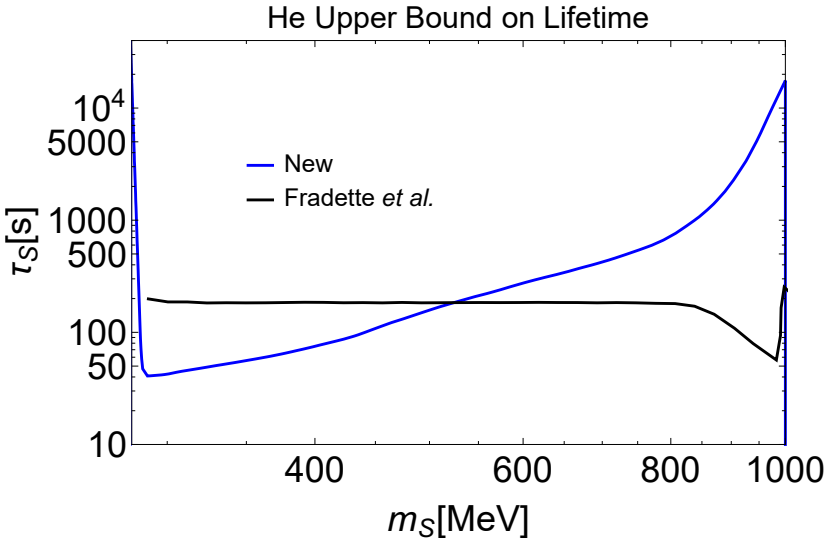

Figure 4.16: *Comparison between upper limit of the excluded space from helium overproduction and the bound as given by Fradette et al.. While the curves are is the same order of magnitude range, there is a significant difference.*

the dynamical Boltzmann equations, and we use a very understandable, semi-analytical argument, the resemblence between the curves is exceptional.

Then, for the upper limit to this contraint, we may simply use (3.12), with a 1% limit specifically. We note first that the cross section of the process (3.13), which we cited as $(\sigma v)^{\pi^-}_D \approx 4.1$ mb, is specific to the product of the reaction being deuterium. While this is the most common result, the reaction could also produce tritium or hydrogen. In this case, we are interested in the total cross section of the dissociation process, irrespective of the products. Then, we have $(\sigma v)^{\pi^-}_{\text{diss}} \approx 6.5$ mb [216].

Then, taking into account the correction from (3.15), which amounts to a factor of ~ 2.8 at $T = 84$ keV, we arrive at the upper limit, shown in Figure 4.16. Here, the agreement between the limit as given by Fradette *et al.* is much worse. However, the limits are of a similar order of magnitude, and such a discrepancy is not unexpected, given the very different methods for obtaining the constraints.

For the deuterium bound, (3.17) is simply applied using the parameters of S we discussed. The resulting bound is shown in Figure 4.17. While the

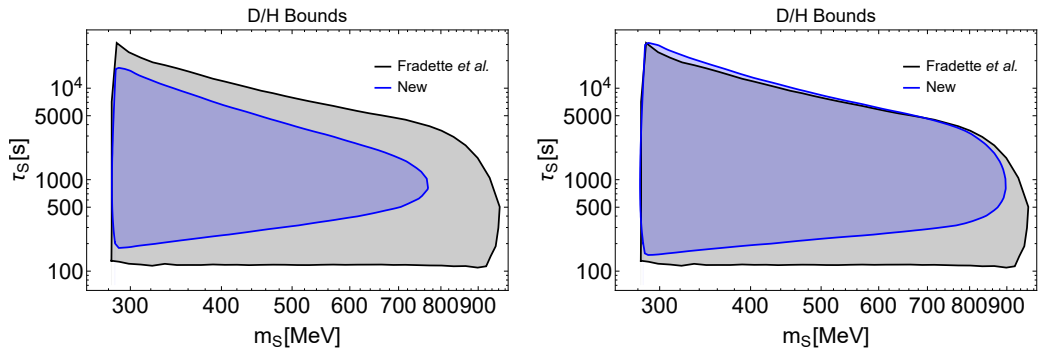

(a) ***(b)***

Figure 4.17: *(a): Comparison between our excluded region from deuterium overproduction, compared to Fradette et al.. We see that the full BBN simulation analysis unambiguously trumps our analytical bound, but the two exclusion ranges do fully overlap, which indicates the accuracy, if not the efficacy, of the analytical bound. Here, we let the extra deuterium production not exceed* $\Delta D/H \leq 0.137 \times 10^{-5}$. *(b): Another comparison, except now we let the extra deuterium production not exceed* $\Delta D/H \leq 0.047 \times 10^{-5}$.

constraint does agree with Fradette *et al.*, is it significantly weaker. This is to be expected, since we are only considering extra deuterium production after deuterium burning is frozen-out, and we take the most conservative limit on the allowed extra deuterium.

To show the potential constraining power of our technique, we also present in Figure 4.17 the same bound, except with a different limit on the allowed extra deuterium. In this case, we take not the maximum possible difference between the theoretical value and the measured value as in the regular bound, but a smaller range. We take the central value for the theoretical value: $D/H = 2.51 \times 10^{-5}$ [187] and use the largest deviation between that and the measured range from [165] to find $\Delta D/H \leq 0.047 \times 10^{-5}$. Now, this coincides much better with Fradette *et al.*, which is not too surprising, because in a sense, using a BBN simulation code is very similar to using the central value of a theoretical prediction. Nevertheless, we stick with the weaker, but more conservative constraint.

4.4.5 Total Constraints

Finally, Figure 4.18 shows all of the constraints we previously discussed in the same plot. Here, we can clearly see the overlap and non-overlap

Version of July 22, 2021– Created July 22, 2021 - 14:39

between different bounds, excluding a significant part of parameter space.

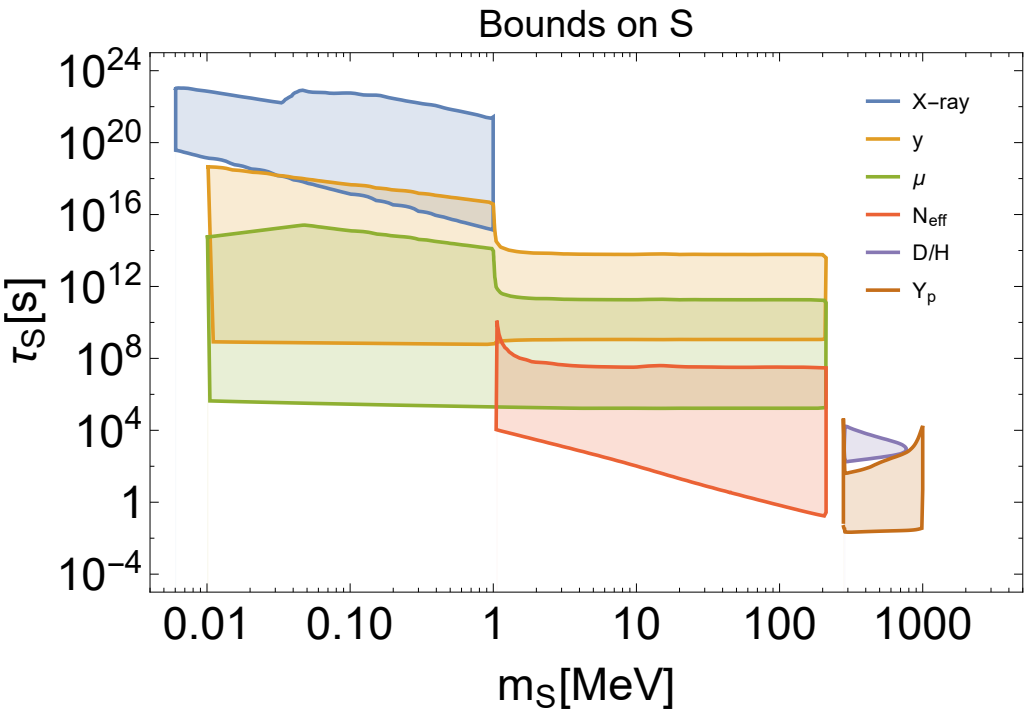

Figure 4.18: *All constraints on S as previously discussed together in the same plot. For details on each constraint individually, see text.*

Chapter 5

Neutrino Portal

Our second case study, the neutrino portal, is one of the most well studied new couplings in physics. It is a promising candidate for the explanation of neutrino masses [266], but it is also studied for possibilities of describing dark matter [201, 269, 270] and baryon asymmetry [37, 271]. An especially interesting model in which this portal plays the main role, it the Neutrino Minimal Standard Model (νMSM), which aims to solve all three main beyond standard model problems in one unified framework [272–274]. We will not consider these applications in particular, focusing instead on the most general "no strings attached" form of the neutrino portal.

5.1 Phenomenology

5.1.1 Heavy Neutral Leptons

The neutrino portal describes a coupling of one or more fermions to the gauge-invariant operator: $(\bar{L}_{\alpha,a}\epsilon_{ab}H^*_b)$. Often a more compact notation is used in literature, with suppressed indices: $(\bar{L}_\alpha \cdot \tilde{H})$[266]. Here, $L_\alpha = (\nu_\alpha, \alpha)^T$ are the SM lepton doublets, with $\alpha \in \{e, \mu, \tau\}$; H is the Higgs doublet, and ϵ_{ab} is the 2-dimensional Levi-Civita (or antisymmetric) symbol, sometimes represented as a Pauli matrix $i\sigma_2$. In full, the neutrino portal looks like this:

$$\mathcal{L}_{\text{NeutrinoPortal}} = F_{\alpha I}(\epsilon_{ab}\bar{L}_{\alpha,a}H^*_b)N_I + \text{h.c.} \tag{5.1}$$

with $F_{\alpha I}$ a Yukawa coupling term. Describing $\mathcal{N}$ new particles, we have $I \in \{1, ..., \mathcal{N}\}$. This coupling term fixes all gauge charges of N_I to be

Version of July 22, 2021– Created July 22, 2021 - 14:39

zero [37]. This is why this type of particles is typically refered to as *sterile neutrino* or Heavy Neutral Lepton (HNL). Uniquely, the lack of charges allows for the introduction of Majorana masses M_I. This Majorana mass matrix may be chosen diagonally without loss of generality [54]. The full Lagrangian then becomes:

$$\mathcal{L} = \mathcal{L}_{SM} + i\overline{N}_I \not{\partial} N_I - (F_{\alpha I}\bar{L}_\alpha \tilde{H} N_I + \frac{1}{2}\overline{N^c}_I M_I N_I + \text{h.c.}) \tag{5.2}$$

After the electro-weak transition, this becomes:

$$\mathcal{L} = \mathcal{L}_{SM} + i\overline{N}_I \not{\partial} N_I - (\underbrace{M^D_{\alpha I}\bar{\nu}_\alpha N_I}_{(A)} + \underbrace{\frac{1}{2}\overline{N^c}_I M_I N_I}_{(B)} + \underbrace{\frac{F_{\alpha I}}{\sqrt{2}}\bar{\nu}_\alpha h^* N_I}_{(C)} + \text{h.c.}) \tag{5.3}$$

Here, we defined $M^D_{\alpha I} \equiv F_{\alpha I} v/\sqrt{2}$, with $v = 246$ GeV. The (C) term (and its conjugate) describe vertices of a neutrino, HNL and Higgs boson, and is usually omitted (MAYBE FIGURE?). Processes involving these vertices will not be relevant for the phenomenology of the HNL's in the range of masses considered in this work, as we will see.
Similarly to the mass mixing we saw in the Higgs portal, there is a mass mixing term (A). The mass part of the Lagrangian may be written as:

$$\mathcal{L}_{mass} = -\frac{1}{2}\begin{pmatrix}\overline{\nu} & \overline{N^c}\end{pmatrix}\begin{pmatrix}0 & M_D \\ M_D^T & M_I\end{pmatrix}\begin{pmatrix}\nu^c \\ N\end{pmatrix} + \text{h.c.} \tag{5.4}$$

where $\nu = (e, \mu, \tau)^T$ and $N = (N_1, ..., N_{\mathcal{N}})^T$. This leads us to a set of natural dimensionless parameters to describe the mixing strengths, the mixing angles:

$$U_{\alpha I} \equiv M^D_{\alpha,I} M_I^{-1} \tag{5.5}$$

Now the interaction of N_I with the rest of the SM is like active neutrinos, but suppressed by the mixing angles:

$$\mathcal{L}_{int} = \frac{g}{2\sqrt{2}} W^+_\mu \overline{N^c_I} \sum_\alpha U^*_{\alpha I}\gamma^\mu(1-\gamma_5)\ell^-_\alpha + \frac{g}{4\cos\theta_W} Z_\mu \overline{N^c_I} \sum_\alpha U^*_{\alpha I}\gamma^\mu(1-\gamma_5)\nu_\alpha + \text{h.c.} \tag{5.6}$$

with θ_W the Weinberg angle.

Up until this point, we've shown general formulae with multiple possible species. The number of parameters increases rapidly with the number of HNLs. Specifically, a model with $\mathcal{N}$ sterile neutrinos has $7\mathcal{N} - 3$ parameters [37]. However, they are not all important for phenomenology.

This is determined only by the masses and the mixing angles U_α (so 4 parameters per HNL). Moreover, if they are not degenerate in mass, they are produced and decay fully independently, without oscillating between eachother (unlike active neutrinos) [275]. Thus, it will be sufficient to find general constraints on the 4 parameters of just one sterile neutrino, which we will simply call N from now on. In this case, the mass matrix M_I reduces to a single numbers, which we call m_N; similarly, we have just U_α for the three mixing angles.

One note: in the literature, one typically comes across a distinction between Majorana HNLs and Dirac HNLs. This could be the cause of some confusion to newcomers to the field. The distinction is important as well, since Majorana particles are their own anti-particles, and thus include charge-conjugated channels in all their interactions.
First, we point out here that this distinction does not come from the presence of Dirac or Majorana mass terms. SM particles cannot have intrinsic mass (Majorana mass), due to gauge charges, and as a result, the left and right chiral Weyl spinors may be combined to form Dirac spinors. However, this can also happen if there is a Majorana mass term. One good example is the two heavy HNLs from the νMSM: because of their mass degeneracy, they can be combined to form a single Dirac HNL. This is why such an particle is often considered. On the other hand, one can just as well split such a Dirac spinor into two Majorana spinors, which will be degenerate in some way [271].

We will consider a single Majorana HNL, but the phenomenology of a Dirac HNL is very similar. In fact, assuming the parameters are the same, the effect on cosmology of one Dirac HNL is exactly the same as the effect of two Majorana HNLs. As a result, one may write $U_D = \sqrt{2}U_M$, where U_D is the Dirac HNL mixing angle and U_M is the Majorana mixing angle [224]. Since we will show constraints using the lifetime τ_N (which scales like $\tau_S \propto U^{-2}$), this effect is compensated for in the plots; they will look the same for both Majorana and Dirac HNLs. Since the 4-dimensional parameter space is difficult to represent visually, whenever different mixing scenarios are relevant, we will use the following: pure e-mixing: $U_\mu = U_\tau = 0$; pure μ-mixing: $U_e = U_\tau = 0$; τ-mixing: pure $U_e = U_\mu = 0$.

5.1.2 Decay and Lifetime

Decay of N goes through the weak interactions, which means decay products may be leptons and quarks, which come in the form of mesons, because of quark confinement. Since the different leptons and mesons have different masses, to which decay opens up if the m_N is high enough, the decay rates are non-trivially dependent on the mixing ratio $U_e : U_\mu : U_\tau$. We will show results for pure mixing for all of the three species (so $1:0:0$ for e-mixing, $0:1:0$ for μ-mixing and $0:0:1$ for τ-mixing).

The various decay modes, depending on the mass m_N, are given in, for example, [274–276]. We can directly use these decay rates. In some cases, the results from these works differ slightly (typically some numerical factor difference). We defer to the most recent work [275] in case of disagreement[i].

Of particular importance is the decay of N for masses below the electron threshold $2m_e$. In this case, the dominant decay channel is $N \to \nu\nu\nu$, with a decay rate given by:

$$\Gamma(N \to \nu_\alpha \nu_\beta \bar{\nu}_\beta) = (1 + \delta_{\alpha\beta}) \frac{G_F^2 m_N^5}{384\pi^3} |U_\alpha|^2 \tag{5.7}$$

$$\Gamma(N \to \sum_{\alpha,\beta} \nu_\alpha \nu_\beta \bar{\nu}_\beta) = \frac{G_F^2 m_N^5}{96\pi^3} U^2 \tag{5.8}$$

where we have defined in the last line $U^2 = \sum_\alpha |U_\alpha|^2$, the total mixing angle.
For these small masses, there is also a one-loop radiative decay channel to a photon (and a neutrino). The decay rate is given by [277]:

$$\Gamma(N \to \gamma\nu) = \frac{9\alpha G_F^2 m_N^5}{256\pi^4} U^2 \tag{5.9}$$

While this decay rate is less than one hundreth that of the main channel, and so does not contribute significantly to the lifetime of N, this decay will be important for its cosmological implications, since it produces a photon with energy $E = m_N/2$ [270].

[i] Note that, although the branching ratios will be unchanged, we have to multiply the total decay rate, as given in [275], by 2 to account for charge-conjugation symmetry of the Majorana HNL.

Version of July 22, 2021– Created July 22, 2021 - 14:39

This leads us into a discussion of the electromagnetic branching ratio, Br_{EM}. When discussing constraints on the scalar portal, we considered Br^S_{EM} only for $m_S < 2m_\mu$, so that the only possible decays are electron-positron pairs and photons. Thus, in this regime, $Br^S_{EM} = 1$. In the case of the neutrino portal, we need to consider this matter more carefully.

We can find the electromagnetic branching ratio by weighting the average energy carried by decay products by their respective branching ratios. If a decay product of N is not either a photon, electron (or positron) or neutrino, it will decay itself. We can then weight their branching ratios from N by the electromagnetic branching ratios of the decay products themselves. The electromagnetic branching ratios of each decay product of N are given in Appendix B.

We approximate the average energy from the decay products as follows. Two-body decays have fixed energies; for the process $N \to A + B$, we have $E_A/m_N = (1 + R_A^2 - R_B^2/2)$ and $E_B/m_N = (1 + R_B^2 - R_A^2)/2$, where $R_X = m_X/m_N$ the mass ratio.

The relativistic kinematics of general three-body decays are non-trivial. Taking the process $N \to A + B + C$, the energy of the decay products depends on the angles. In this case, we make some approximations. For the mass hierarchy $m_A \approx m_B \gg m_C$, we take C as massless, and then the energy of the other two is given by:

$$\frac{E_A}{m_N} = \frac{1}{2\sin^2\theta} + \frac{1}{2}\sqrt{\frac{1}{\sin^4\theta} - \frac{1 + 4R_A^2\cos^2\theta}{\sin^2\theta}} \tag{5.10}$$

where θ is half the angle between A and B, running from $0 < \theta \leq \pi/2$. To find the average energy, we just average over all angles[ii].
Similarly, for the case of $m_A \gg m_B \approx m_C$, we assume the light particles are massless and find:

$$\frac{E_A}{m_N} = -\frac{\cos^2\theta}{\sin^2\theta} + \sqrt{\frac{\cos^4\theta}{\sin^4\theta} + \frac{\cos^2\theta + R_A^2}{\sin^2\theta}} \tag{5.11}$$

[ii]We note that the assumption of uniform probability distribution for the angles is not well founded, and most definitely incorrect. However, the result of this calculation will at least be between the limits $1/3 < E_A/m_N < 1/2$, and show qualitatively the same behaviour; namely that the light (massless) particle gets less energy than the heavy particles. This will be a sufficient approximation.

where we average over all angles again. Here, θ describes half the angle between B and C.

The resulting electromagnetic branching ratios are shown in Figure 5.1. Important features visible are: the low, but present, decay to a photon below the electron threshold; the splitting of the lines for different mixing schemes, due to the different lepton masses; at some point, Br_{EM} actually goes over 0.5, which means in that range, most of the decay energy goes into the photon bath.

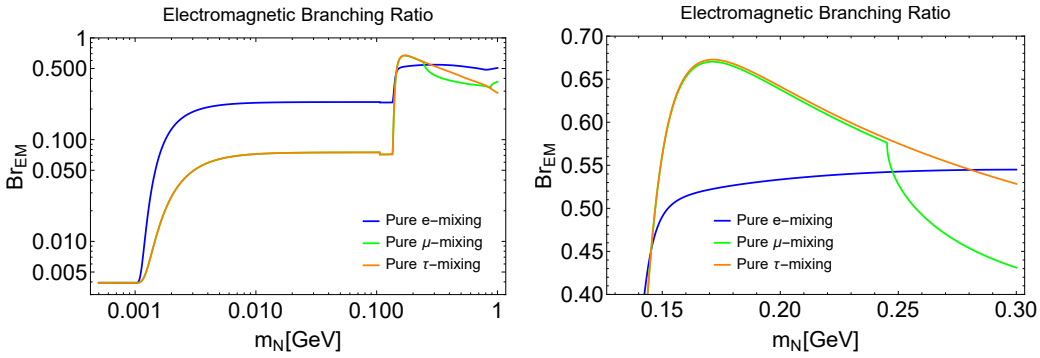

(a) ***(b)***

Figure 5.1: *Electromagnetic branching ratios from decay of N, depending on the masses, for different mixing scenarios. Decay rates are taken primarily from [275]. (b) is a zoomed in version of (a), so that the regime where $Br_{EM} > 0.5$ becomes clearer.*

5.2 Production in Early Universe

Before calculating the primordial yield of HNLs, it is of vital importance to know the temperature dependence of the mixing angle. As we will see, the suppression of the mixing in the very hot plasma of the early universe determines the peak of HNL production, being much lower than what we saw for the scalar portal[iii].

[iii]For much of this section, I follow closely unpublished work done by Maksym Ovchynnikov, to whom I am indebted.

5.2.1 Thermal Mixing Angle

Taking u^μ the 4-velocity of the plasma and p the neutrino momentum, with no lepton asymmetry, the thermal self-energy is given by [278, 279]:

$$\Sigma(p) = -A\left[(p\cdot u)\not{u} - \frac{1}{4}\not{p}\right](1-\gamma_5) = -A\not{e}(1-\gamma_5)$$
$$A = \frac{16\sqrt{2}\langle E_e\rangle n_e G_F}{3m_W^2}\left[1+\frac{m_W^2}{2m_Z^2}\right]$$

with $\langle E_e\rangle = (7\pi^4/180\zeta(3))T \approx 3.15T$ is the average electron energy (assuming $T \gg m_e$) and $n_e = (3\zeta(3)/4\pi^2)T^3$ the (ultra-relativistic) electron number density.
Thus, the neutrino propagator gets modified in the thermal bath:

$$D_\nu(p) = \frac{1}{\not{p}}\sum_n\left(-\Sigma(p)\frac{1}{\not{p}}\right)^n = \frac{1}{\not{p}-\Sigma(p)} \tag{5.12}$$

where the ν subscript denotes the neutrino aspect, not an index.

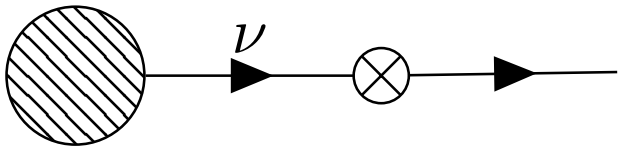

Figure 5.2: *Diagram of N production process. The blob on the left is some general interaction process that results in a neutrino. The crossed dot denotes the mixing of ν into N.*

Recalling the interaction part of the Lagrangian 5.3, specifically term (A), we find that the process from Figure 5.2 is represented by matrix element

$$\mathcal{M} = U_\alpha m_N \bar{N}(p) D_{\nu_\alpha}(p)\gamma^\mu(1-\gamma_5)... \tag{5.13}$$

where (...) represents the rest of the interaction, $\gamma^\mu(1-\gamma_5)$ comes from the neutrino interaction and α represents the different neutrino species.

After some tedious calculation, we find:

$$\begin{aligned}\mathcal{M} &\approx U_\alpha m_N \bar{N}(p)\frac{\not{p}}{p^2+4A(p\cdot c)}\gamma^\mu(1-\gamma_5)... \\ &\approx U_\alpha^M \bar{N}(p)\gamma^\mu(1-\gamma_5)...\end{aligned}$$

with:

$$U_\alpha^M = \frac{U_\alpha}{1+4A\left(\frac{(p\cdot u)^2}{m_N^2}-\frac{1}{4}\right)}$$

where we used the on-shell condition $p^2 = m_N^2$ and the Dirac equation $\bar{N}\not{p} = m_N\bar{N}$.

Then we assume relativistic momenta ($p_N \gg m_N$), so we neglect the $1/4$ term, and fill in the values for A, to arrive at the thermal mixing angle U_α^M:

$$U_\alpha^M(T) = \frac{U_\alpha}{1+2.2\cdot 10^{-7}\left(\frac{T}{1\,\mathrm{GeV}}\right)^6\left(\frac{1\,\mathrm{GeV}}{m_N}\right)^2} \tag{5.14}$$

This is congruent with the literature [280, 281].

5.2.2 Freeze-out Abundance

At temperatures $T \gg m_N$, our HNL interacts in much the same way an active neutrino would, and its total interaction rate is similarly given by:

$$\Gamma_N^{\mathrm{int}} \approx bG_F^2T^5U^2 \tag{5.15}$$

where b is some constant to be determined by the specific processes.
From this, we can already find the peak of production by finding the maximum of the quantity $\chi = \Gamma_N^{\mathrm{int}}/H$. Already at first glance, we can see that this fraction scales as $\chi \propto T^3$ at low temperatures, when the thermal effects on the mixing angle are negligible, but as $\chi \propto T^{-9}$ at high temperatures. This implies that there is some "sweet spot" for production in between these regimes.

We can find the maximum of χ by setting $\mathrm{d}\chi/\mathrm{d}T = 0$, which is a straighforward calculation. The result gives:

$$T_{max} = \frac{1}{(3\cdot 2.2\cdot 10^{-7})^{1/6}}\left(\frac{m_N}{1\,\mathrm{GeV}}\right)^{1/3}\mathrm{GeV} \approx 11\left(\frac{m_N}{1\,\mathrm{GeV}}\right)^{1/3}\mathrm{GeV} \tag{5.16}$$

Version of July 22, 2021– Created July 22, 2021 - 14:39

This is significantly lower than the bulk of production for the scalar portal, which happened near electro-weak temperatures. However, it is significantly higher than m_N in the range we consider, which means that () holds.

The relativistic equilibrium abundance is then given, similarly to the scalar portal (4.8), as:

$$Y_N^{\text{eq}} = \frac{n_N^{\text{eq}}}{\tilde{s}} = \frac{3}{2}\frac{45\zeta(3)}{2\pi^4 g_*} \simeq \frac{0.42}{g_*} \tag{5.17}$$

where the extra factor $3/2$ comes from the fact that N is a fermion (which introduces a factor $3/4$ from integration of the Fermi-Dirac distribution[102]) and the 2 spin degrees of freedom. We use two values of g_*: for $m_N > 1$ MeV, we have most production occuring at temperatures $T > 1.1$ GeV, so we use $g_* = 86.25$; for $m_N < 1$ MeV, we take instead $g_* = 61.75$ [121].

If N is still relativistic during decoupling, then (5.17) gives its abundance. The lower production temperatures, however, also create the possibility of decoupling while N is already non-relativistic. As it turns out, we do not have to worry about this, since for the range of mixing angle we consider, $m_N \ll T_{dec}$, where $T_{dec} \approx (G_F^2 M_{Pl}^* U^2)^{-1/3}$ in the relativistic limit. In terms of lifetime, it is true that for very small lifetimes, HNLs with small masses[iv] would decouple non-relativistically. However, those small lifetimes HNLs will only impact cosmology through BBN, and for our BBN constraints, we use only use heavy masses that can decay into mesons, in which case, the HNLs still decouple relativistically[v] [171].

5.2.3 Freeze-in Abundance

For the freeze-in abundance, we may rewrite (4.9) to find [171, 282]:

$$\frac{\mathrm{d}Y_N}{\mathrm{d}t} = -\Gamma_N^{\text{int}}(Y_N - Y_N^{eq}) \tag{5.18}$$

[iv] Note that small masses and small lifetimes imply very large mixing angles.

[v] Strictly, there is small range $100\,\text{MeV} \lesssim m_N \lesssim 200\,\text{MeV}$, wherein non-relativistic decoupling could happen in the lifetime range of interest for BBN, which is considered in [171]. We neglect this effect and, as we will see, arrive at qualitatively the same bounds.

Using the standard time-temperature relation, this can be integrated over all temperatures to find:

$$
\begin{aligned}
-\int_0^\infty \frac{\Gamma_N^{\text{int}}}{TH(T)}\mathrm{d}T &= -bG_F^2 M_{Pl}^* U^2 \int_0^\infty \frac{T^2}{\left[1+2.2\cdot 10^7 \left(\frac{T}{1\,\text{GeV}}\right)^6 \left(\frac{1\,\text{GeV}}{m_N}\right)^2\right]^2}\mathrm{d}T \\
&= -bG_F^2 M_{Pl}^* U^2 \frac{\pi}{12\sqrt{\frac{2.2\cdot 10^7}{1\,\text{GeV}}}\left(\frac{1\,\text{GeV}}{m_N}\right)^2} \\
&= -\frac{2.8\cdot 10^7 \cdot b}{\sqrt{2.2\cdot 10^7}}\frac{m_N}{1\,\text{GeV}}U^2
\end{aligned}
$$

where in the last line, we used $g_* = 86.25$[vi].

Then the complete freeze-in abundance is given by:

$$
Y_N = Y_N^{eq}\left(1-\exp\left[-6.0\cdot 10^3 \cdot b\frac{m_N}{1\,\text{GeV}}U^2\right]\right) \tag{5.19}
$$

The prefactor b will be relevant here, so we must find it by looking at the matrix elements for individual processes $A+B\to C+N$. From the matrix elements in [224], we arrive at $b\approx 18$ for the bulk of production happening above $T = 1$ GeV (so $m_N > 1$ MeV) and $b\approx 12$ for production between 1 GeV and $\Lambda_{QCD}\sim 200$ MeV (so $m_N < 1$ MeV).

5.3 Experimental Limits

Experimental limits on HNLs are strongly dependent on the hierarchy of the mixing angles. Owing to the different scales of the lepton flavours, it is more difficult to constrain a τ-coupling than e- or μ-mixing. Many experimental searches, including for example at ATLAS [283], Belle[284] and LHCb [285] have yielded good constraints on HNLs of masses up to even $\mathcal{O}(100\,\text{GeV})$, but we only present sub-GeV bounds, which typically come from beam-dump experiments. Figure 5.3 shows some of these constraints, for pure e- and μ-mixing, which we briefly describe. For a more complete description of experimental status, see for example [266].

[vi] We use this here for all masses, because g_* is under a square root, so the difference between 61.75 and 86.25 is negligible.

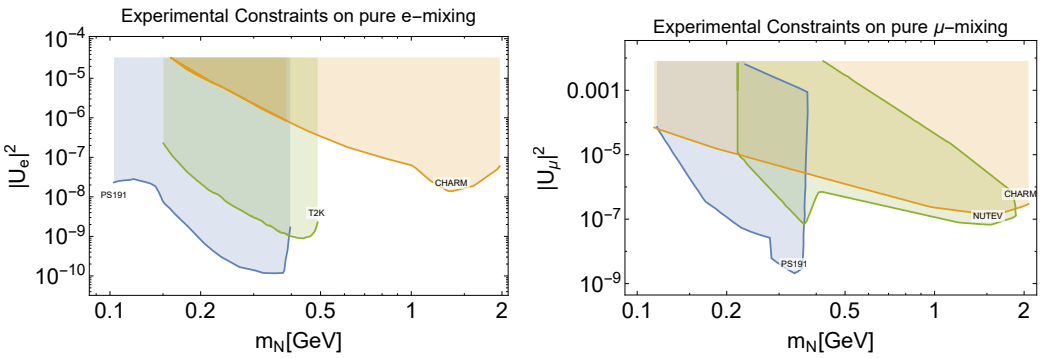

(a) *Pure e-mixing* **(b)** *Pure μ-mixing*

Figure 5.3: *Results of several particle experiments aiming to constrain the available parameter space of N. Including results from the PS191 experiment (PS191) from CERN [286], the CHARM collaboration (CHARM) [287], the T2K collaboration (T2K) [288] and the NuTeV experiment (NUTEV) from Fermilab [289]. See text for details.*

We do not show here constraints from specific applications, such as a "see-saw" bound, which comes from the observed pattern of neutrino oscillations, or phase-space limits from dark matter.

PS191

The PS191 CERN experiment [286] was a dedicated search for signs of heavy neutrino decays in a low-energy neutrino beam. Lack of any decay events allows to constrain the mixing. All three pure-mixing case are somewhat constrained, but the most stringent bounds belong to the e- and μ-mixing.

CHARM

The CHARM collaboration [287] performed a beam-dump experiment, where protons were dumped into a fixed target of copper. Decays from HNLs were searched for, specifically electrons in the final state. No detection of any decay event puts constraints on the mixing.

Version of July 22, 2021– Created July 22, 2021 - 14:39

NuTeV

The NuTeV (E-815) experiment at Fermilab [289] searched for decay signals of HNLs in another beam-dump experiment. Protons were dumped into a fixed Berillium-oxide target, with the specific aim of searching for muonic final states. This puts constraints on the μ-mixing case.

T2K

The T2K collaboration [288] searched for signatures of HNL decay, specifically to leptons. The HNLs could be produced from kaon decay in the standard neutrino beam, which is produced by dumping protons on a graphite target. This puts constraints on mixing for all flavours, although only the pure e-mixing bound is given in [288] (other bounds are marginalised).

5.4 Results

Having discussed these constraints in detail, we now simply present the obtained bounds.

5.4.1 X-ray

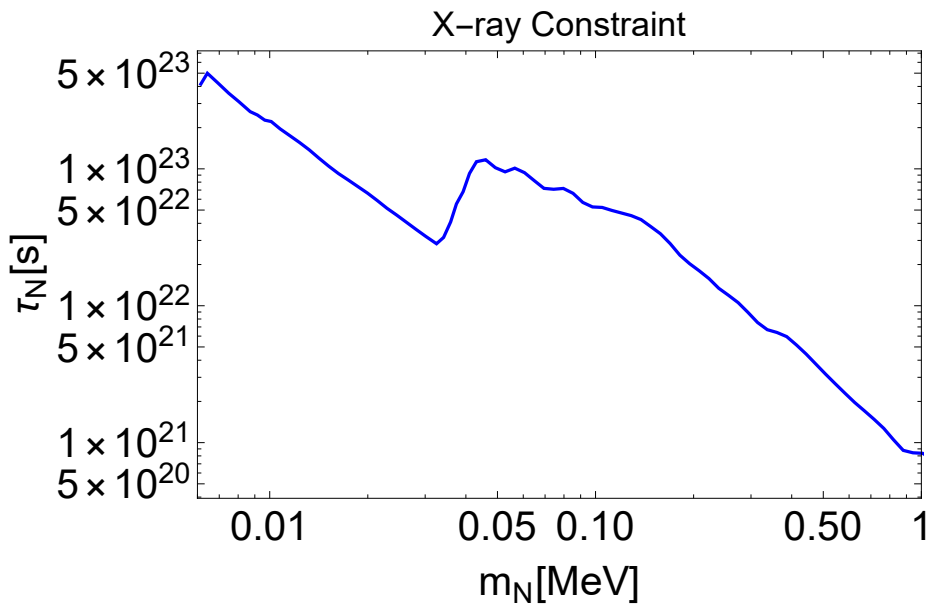

Figure 5.4: *Lower limit on allowed lifetime of N.*

Figure 5.4 shows the constraint from X-rays in terms of τ_N. Since in this case the decay rate responsible for X-ray production is not the same as the decay rate that determines the lifetime, we first find a limit in terms of the mixing angles U, and then translate it into a lifetime. This is straightforward, since neither rate in this mass range depends on the mixing hierarchy.

Similarly to the scalar portal, we apply this constraint down to time t_0. More specifically, down to the lifetimes at which the decay into photons at t_0 becomes too small to be distinguished. We show this in the final plot.

5.4.2 Spectral Distortions

Here, the constraints are slightly different, depending on which mixing scheme is used. We show results for all three mixing schemes in Figure 5.5. Both plots show a particular "pointed" shape in the low mass regime, coming from the equilibrium abundance. We cut off the plots at $m_N = 1$ keV, since around this mass, the assumptions we used for the production will cease to be valid.

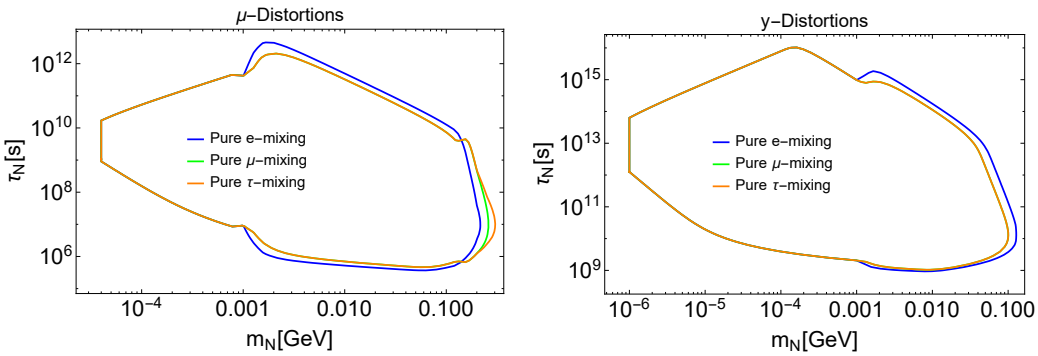

(a) ***(b)***

Figure 5.5: *Excluded regions from spectral distortions: μ-type distortion (a) and y-type distortion (b). Excluded area is not filled for clarity. There is significant overlap, particularly in the μ- and τ curves.*

5.4.3 N_{eff}

Like we discussed for the scalar portal, it is prudent to check the relative energy density contributions to the universe first. Applying (4.13) to the N particle, we find a large range of significant ρ_N, shown in Figure 5.6. Note that the comparison with ρ_{rad} is less relevent for very long lifetimes, since at late stages of universal evolution, radiation starts to become but a small fraction of the dominant consituents of the univers (namely matter, and then dark energy).

Nevertheless, there is a large amount of overlap between this region of significant ρ_N and the excluded regions from spectral distortions. Since those bounds assumed a standard universal composition, this is troubling. However, this will be resolved by considering contraints from N_{eff}.

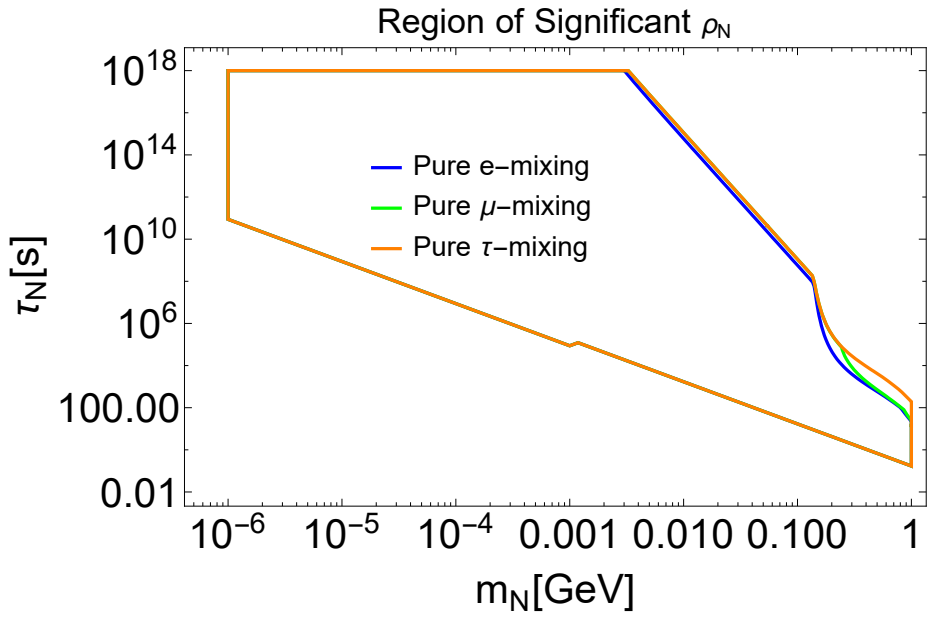

Figure 5.6: *Region of parameter space where ρ_N exceeds ρ_{rad} when the ratio between the two is at its maximum.*

First, we show the numerical constraints in Figure 5.7. We see that N_{eff} constrains the parameter space such that most of the region where ρ_N is very large, is excluded. This is not unexpected, since N_{eff} almost directly constrains the energy density. Contrary to what we saw in the scalar portal, here, the N_{eff} is bound both from below ($N_{eff} > 2.56$) and from above ($N_{eff} < 3.42$), since N can decay primarily into the neutrino- or photon baths, depending on its mass.

Note also the low-lifetime, high-mass corner, where there is a sharp cut-off in the excluded region from N_{eff}. As discussed, this comes from the effects of neutrino injection in this region being difficult to predict, so we omit it from our analysis.

Unfortunately, in this case, we cannot make a nice expression of the expected bound in terms of ρ_N/ρ_{rad}, because the electromagnetic branching ratio depends non-trivially on the mass. However, we may still use our simplified formula and compare results. Like the scalar portal, we apply the formula at a time $t = \tau_N/10$ and show the resulting excluded area in comparison to the numerical results in Figure 5.8. Barring some slight differences, likely due to the granularity of the data we produced, there is a very good agreement again.

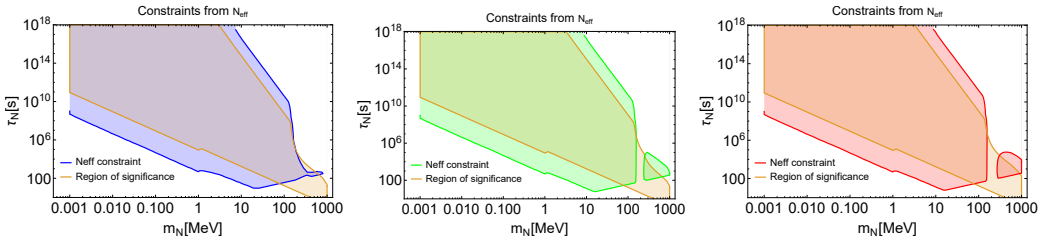

(a) *Pure e-mixing* ***(b)*** *Pure μ-mixing* ***(c)*** *Pure τ-mixing*

Figure 5.7: *Excluded region from numerically considering the impact on N_{eff}, compared with the region from Figure 5.6.*

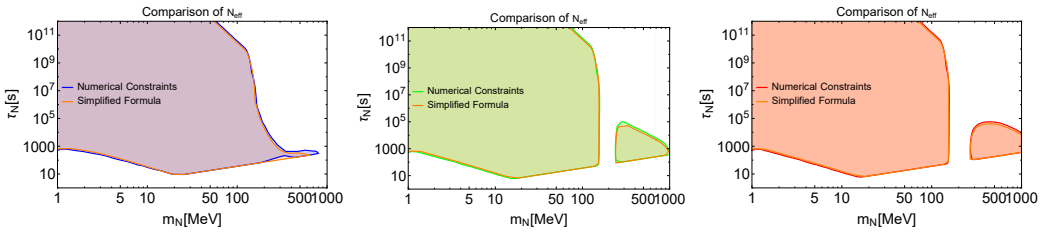

(a) *Pure e-mixing* ***(b)*** *Pure μ-mixing* ***(c)*** *Pure τ-mixing*

Figure 5.8: *Excluded region from numerical consideration and the simplified formula from the impact on N_{eff}. We find a good agreement between the two methods.*

Importantly, since N_{eff} is measured from the CMB, there is a kink at very high lifetimes, after which decay would not affect the CMB. We simply find the effect of decaying HNLs on N_{eff} at the time of recombination, even if the lifetime exceeds the age of the universe at that point, taking into account the differing abundances. This will be shown in the final plot.

5.4.4 BBN

Our method for the constraint from helium overproduction is directly based on an application of it to the neutrino portal in particular [171]. Therefore, we can apply this bound directly, without any caveats.

In Figure 5.9, we show these bounds for the different mixing scenarios. This is in good agreement with the original work, which cited $\tau_N \lesssim 0.020$ s for the lower bound and $\tau_N \gtrsim 20$ s for the upper bound [171].

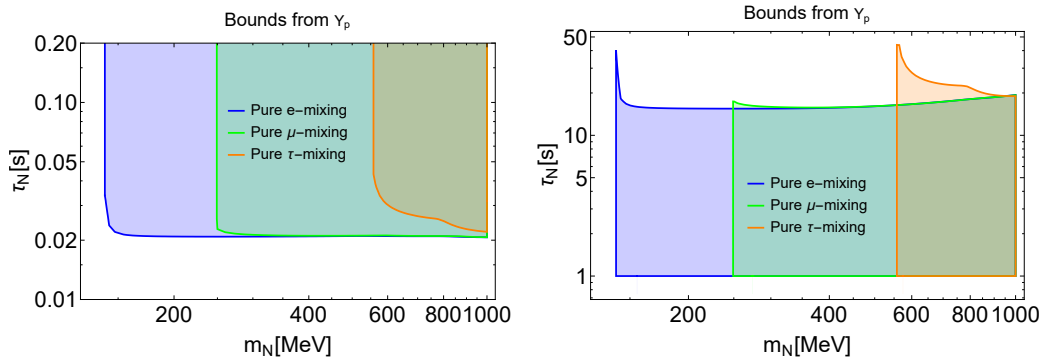

(a) ***(b)***

Figure 5.9: *(a): Upper limits on lifetime of N from helium overproduction, constrained by measurement of Y_p. (b): Lower limits that require that the number of dissociating mesons is less than one percent of the number of helium nuclei.*

For the bounds from deuterium overproduction, we need to be careful. As shown in Figure 5.10a, the excluded regions from D/H partially overlap with the region of significant ρ_N from Figure 5.6. Note that we show here the bounds from all mixing schemes, compared with the region of significance from only e-mixing. The regions associated with each mixing scenario look very similar, so for clarity, only one is shown. Since we assume SBBN in these bounds, and deviations during BBN can have a large impact on final light element abundances, these bounds are not applicable in that region. Thus, we have to cut this region out of the excluded range. For this, we do use the large ρ_N region from each mixing individually.

Figure 5.10b shows the adjusted constraints, where the large ρ_N regions have been cut out of the excluded range. Despite this, we are still left with a sizeable constraint.

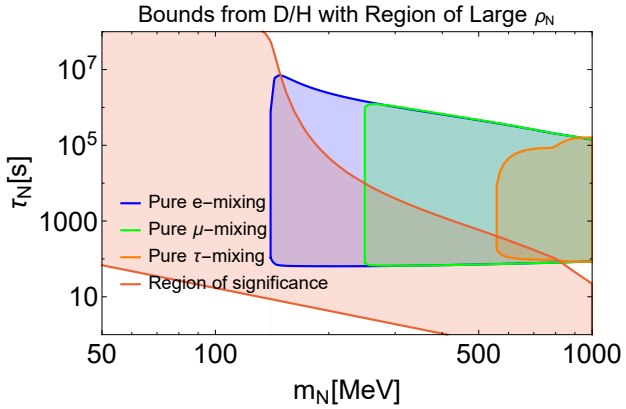

(a) *Excluded region of parameter space from deuterium overproduction (using $\Delta D/H < 0.137 \times 10^{-5}$) for different mixing scenarios, plotted together with the region of large ρ_N from Figure 5.6 for pure e-mixing to show roughly where the constraints do not apply.*

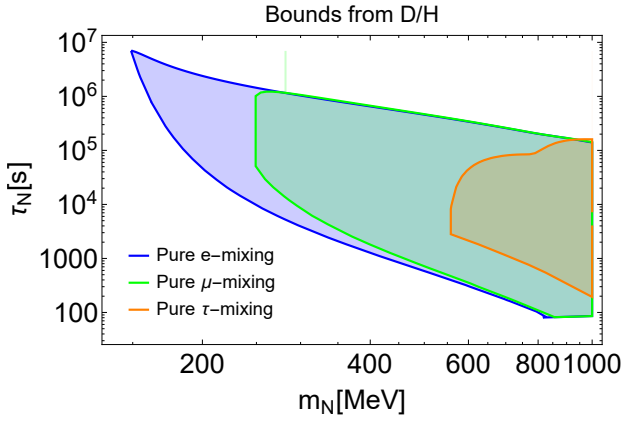

(b) *Excluded region of parameter space from deuterium overproduction (using $\Delta D/H < 0.137 \times 10^{-5}$), where the regions from Figure 5.6 have been cut out of the excluded region.*

Figure 5.10

5.4.5 Total Constraints

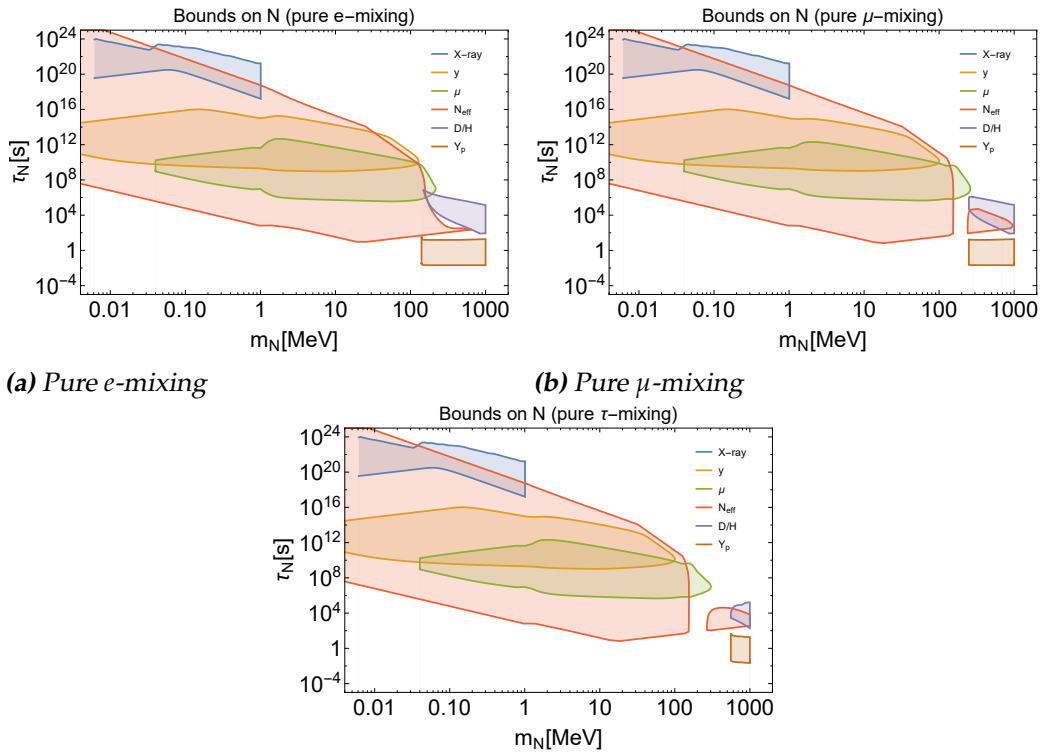

(a) *Pure e-mixing*

(b) *Pure μ-mixing*

(c) *Pure τ-mixing*

Figure 5.11: *Summary of all constraints on N previously discussed.*

In Figure 5.11, we show together all the constraints on N. Notable is the kink in the upper limit of the N_{eff} constraint, visible at a lifetime of around 10^14 s and mass of roughly 30 MeV. Without concern for the fact that N_{eff} is measured at recombination, the excluded range from N_{eff} would fully engulf the range from X-ray. Now all contraints we considered play a role, albeit a rather small one for the spectral distortions, in limiting the available parameter space.

Chapter 6

Conclusion and Outlook

In conclusion, this work presents a series of general techniques and principles based on cosmological and astrophysical observations that can be used to constrain the parameters of different classes of portals. We have described qualitatively each of these methods and applied them to two case studies: the scalar and neutrino portals, where our results match well with previous work.

This approach lends well to generalisation to other portals, such as the vector or axion portals. Of course, there will be different physics at play. However, the qualitative description given in this work focused on the physical understanding of the methods, so it should aid in expansion of these constraints.

Each constraint used deserves a more detailed consideration in a dedicated work, and several could well be expanded beyond the applications outlined here. The X-ray constraint could be expanded to incorporate final state radiation and be applied to heavier masses. The N_{eff} constraint could be considered more precisely and include neutrino decoupling effects. Additional BBN constraints could be considered, like photo-dissociation of light elements. The list goes on.

Clearly, there is much potential in cosmological constraints on weakly coupled portal, and plenty of room for future research. With ever more precise measurements, both in particle experiments on the ground, and astrophysical observations in the sky, and the right researchers working on them, solutions to our current problems are sure to come soon.

Version of July 22, 2021– Created July 22, 2021 - 14:39

Bibliography

[1] M. J. Herrero, *The Standard Model*, in *Lectures presented at the NATO ASI 98 School, Techniques and Concepts of High Energy Physics*, Universidad Autonoma de Madrid, 1998.

[2] M. E. Peskin and D. V. Schroeder, *An Introduction to quantum field theory*, Addison-Wesley, Reading, USA, 1995.

[3] A. Salam and J. C. Ward, *Weak and electromagnetic interactions*, Il Nuovo Cimento Series 10 **11**, 568 (1959).

[4] S. L. Glashow, *Partial-symmetries of weak interactions*, Nuclear Physics **22**, 579 (1961).

[5] S. Weinberg, *A model of leptons*, Physical Review Letters **19**, 1264 (1967).

[6] H. Fritzsch, M. Gell-Mann, and H. Leutwyler, *Advantages of the color octet gluon picture*, Physics Letters B **47**, 365 (1973).

[7] D. J. Gross and F. Wilczek, *Ultraviolet behavior of non-abelian gauge theories*, Physical Review Letters **30**, 1343 (1973).

[8] H. D. Politzer, *Reliable perturbative results for strong interactions?*, Physical Review Letters **30**, 1346 (1973).

[9] M. K. Gaillard, P. D. Grannis, and F. J. Sciulli, *The standard model of particle physics*, Reviews of Modern Physics **71**, S96 (1999).

[10] M. Banner et al., *Observation of very large transverse momentum jets at the CERN pp collider*, Physics Letters B **118**, 203 (1982).

[11] L. Di Lella and C. Rubbia, *The Discovery of the W and Z Particles*, in *60 Years of CERN Experiments and Discoveries*, chapter 7, pages 137–163, World Scientific, 2015.

[12] J. J. Aubert, U. Becker, P. J. Biggs, J. Burger, M. Chen, G. Everhart, P. Goldhagen, J. Leong, T. McCorriston, T. G. Rhoades, M. Rohde, S. C. Ting, S. L. Wu, and Y. Y. Lee, *Experimental observation of a heavy particle J*, Physical Review Letters **33**, 1404 (1974).

[13] J. E. Augustin et al., *Discovery of a narrow resonance in e+e- annihilation*, Physical Review Letters **33**, 1406 (1974).

[14] M. L. Perl et al., *Evidence for anomalous lepton production in e+-e- annihilation*, Physical Review Letters **35**, 1489 (1975).

[15] S. W. Herb, D. C. Hom, L. M. Lederman, J. C. Sens, H. D. Snyder, J. K. Yoh, J. A. Appel, B. C. Brown, C. N. Brown, W. R. Innes, K. Ueno, T. Yamanouchi, A. S. Ito, H. Jöstlein, D. M. Kaplan, and R. D. Kephart, *Observation of a dimuon resonance at 9.5 GeV in 400-GeV proton-nucleus collisions*, Physical Review Letters **39**, 252 (1977).

[16] F. Abe et al., *Observation of top quark production in $p^{-}p$ collisions with the collider detector at fermilab*, Physical Review Letters **74**, 2626 (1995).

[17] S. Abachi et al., *Observation of the top quark*, Physical Review Letters **74**, 2632 (1995).

[18] K. Kodama et al., *Observation of tau neutrino interactions*, Physics Letters, Section B: Nuclear, Elementary Particle and High-Energy Physics **504**, 218 (2001).

[19] P. Söding, *On the discovery of the gluon*, European Physical Journal H **35**, 3 (2010).

[20] G. Aad et al., *Observation of a new particle in the search for the Standard Model Higgs boson with the ATLAS detector at the LHC*, Physics Letters, Section B: Nuclear, Elementary Particle and High-Energy Physics **716**, 1 (2012).

[21] S. Chatrchyan et al., *Observation of a new boson at a mass of 125 GeV with the CMS experiment at the LHC*, Physics Letters, Section B: Nuclear, Elementary Particle and High-Energy Physics **716**, 30 (2012).

[22] G. Aad et al., *Combined search for the Standard Model Higgs boson using up to 4.9 fb-1 of pp collision data at s=7TeV with the ATLAS detector at the LHC*, Physics Letters, Section B: Nuclear, Elementary Particle and High-Energy Physics **710**, 49 (2012).

[23] S. Chatrchyan et al., *Combined results of searches for the standard model Higgs boson in pp collisions at s=7 TeV*, Physics Letters, Section B: Nuclear, Elementary Particle and High-Energy Physics **710**, 26 (2012).

[24] F. Jegerlehner, M. Kalmykov, and B. A. Kniehl, *Self-consistence of the Standard Model via the renormalization group analysis*, in *Journal of Physics: Conference Series*, volume 608, page 12074, Institute of Physics Publishing, 2015.

[25] S. Hossenfelder, *Experimental search for quantum gravity*, in *Classical and Quantum Gravity: Theory, Analysis and Applications*, pages 257–282, Nova Science Publishers, Inc., 2012.

[26] T. Rothman and S. Boughn, *Can gravitons be detected?*, Foundations of Physics **36**, 1801 (2006).

[27] C. M. Will, *The confrontation between general relativity and experiment*, Living Reviews in Relativity **9**, 3 (2006).

[28] D. Griffiths, *Introduction to Elementary Particles Second, Revised Edition*, Wiley, 2008.

[29] J. N. Bahcall and M. H. Pinsonneault, *Standard solar models, with and without helium diffusion, and the solar neutrino problem*, Reviews of Modern Physics **64**, 885 (1992).

[30] P. F. de Salas, D. V. Forero, C. A. Ternes, M. Tórtola, and J. W. Valle, *Status of neutrino oscillations 2018: 3σ hint for normal mass ordering and improved CP sensitivity*, Physics Letters, Section B: Nuclear, Elementary Particle and High-Energy Physics **782**, 633 (2018).

[31] Z. Maki, M. Nakagawa, and S. Sakata, *Remarks on the Unified Model of Elementary Particles*, Progress of Theoretical Physics **28**, 870 (1962).

[32] A. Y. Smirnov, *Neutrino mass and new physics*, Journal of Physics: Conference Series **53**, 44 (2006).

[33] A. G. Cohen, A. De Rújula, and S. L. Glashow, *A Matter-Antimatter Universe?*, The Astrophysical Journal **495**, 539 (1998).

[34] N. Aghanim et al., *Planck 2018 results: VI. Cosmological parameters*, Astronomy and Astrophysics **641** (2020).

[35] G. Steigman, *Primordial Nucleosynthesis in the Precision Cosmology Era*, Annual Review of Nuclear and Particle Science **57**, 463 (2007).

[36] F. Iocco, G. Mangano, G. Miele, O. Pisanti, and P. D. Serpico, *Primordial nucleosynthesis: From precision cosmology to fundamental physics*, **472**, 1 (2009).

[37] K. Bondarenko, *Plan B for particle physics: finding long lived particles at CERN*, PhD thesis, Leiden University, 2018.

[38] A. D. Sakharov, *Violation of cp in variance, C asymmetry, and baryon asymmetry of the universe*, Pisma Zh. Eksp. Teor. Fiz. **5**, 32 (1967).

[39] V. Kuzmin, V. Rubakov, and M. Shaposhnikov, *On Anomalous Electroweak Baryon-Number Non-Conservation in the Early Universe*, volume 8, pages 254–260, Elsevier, 1991.

[40] C. S. Wu, E. Ambler, R. W. Hayward, D. D. Hoppes, and R. P. Hudson, *Experimental test of parity conservation in beta decay [5]*, 1957.

[41] J. L. Rosner, *CP violation-a brief review*, in *AIP Conference Proceedings*, volume 540, pages 283–304, AIP Publishing, 2003.

[42] M. B. Gavela, P. Hernandez, J. Orloff, O. Péne, and C. Quimbay, *Standard model CP-violation and baryon asymmetry (II). Finite temperature*, Nuclear Physics, Section B **430**, 382 (1994).

[43] P. Huet and E. Sather, *Electroweak baryogenesis and standard model CP violation*, Physical Review D **51**, 379 (1995).

[44] K. Kajantie, M. Laine, K. Rummukainen, and M. Shaposhnikov, *Is there a hot electroweak phase transition at mH≥mW*, Physical Review Letters **77**, 2887 (1996).

[45] K. Rummukainen, M. Tsypin, K. Kajantie, M. Laine, and M. Shaposhnikov, *The universality class of the electroweak theory*, Nuclear Physics B **532**, 283 (1998).

[46] G. Aad et al., *Combined Measurement of the Higgs Boson Mass in pp Collisions at s =7 and 8 TeV with the ATLAS and CMS Experiments*, Physical Review Letters **114**, 191803 (2015).

[47] E. Corbelli and P. Salucci, *The extended rotation curve and the dark matter halo of M33*, Monthly Notices of the Royal Astronomical Society **311**, 441 (2000).

[48] S. W. Allen, A. E. Evrard, and A. B. Mantz, *Cosmological parameters from observations of galaxy clusters*, Annual Review of Astronomy and Astrophysics **49**, 409 (2011).

[49] A. Refregier, *Weak Gravitational Lensing by Large-Scale Structure*, in *Annual Review of Astronomy and Astrophysics*, volume 41, pages 645–668, Annual Reviews 4139 El Camino Way, P.O. Box 10139, Palo Alto, CA 94303-0139, USA, 2003.

[50] P. Natarajan, U. Chadayammuri, M. Jauzac, J. Richard, J. P. Kneib, H. Ebeling, F. Jiang, F. van den Bosch, M. Limousin, E. Jullo, H. Atek, A. Pillepich, C. Popa, F. Marinacci, L. Hernquist, M. Meneghetti, and M. Vogelsberger, *Mapping substructure in the HST Frontier Fields cluster lenses and in cosmological simulations*, Monthly Notices of the Royal Astronomical Society **468**, 1962 (2017).

[51] J. Lesgourgues and S. Pastor, *Massive neutrinos and cosmology*, **429**, 307 (2006).

[52] S. D. M. White, C. S. Frenk, and M. Davis, *Clustering in a neutrino-dominated universe*, The Astrophysical Journal **274**, L1 (1983).

[53] S. Tremaine and J. E. Gunn, *Dynamical role of light neutral leptons in cosmology*, Physical Review Letters **42**, 407 (1979).

[54] A. Boyarsky, O. Ruchayskiy, and D. Iakubovskyi, *A lower bound on the mass of dark matter particles*, Journal of Cosmology and Astroparticle Physics **2009**, 005 (2009).

[55] E. Ma, *Pathways to naturally small neutrino masses*, Physical Review Letters **81**, 1171 (1998).

[56] A. G. Cohen, D. B. Kaplan, and A. E. Nelson, *Progress in electroweak baryogenesis*, Annual Review of Nuclear and Particle Science **43**, 27 (1993).

[57] M. Trodden, *Electroweak baryogenesis*, Reviews of Modern Physics **71**, 1463 (1999).

[58] D. Clowe, M. Bradač, A. H. Gonzalez, M. Markevitch, S. W. Randall, C. Jones, and D. Zaritsky, *A Direct Empirical Proof of the Existence of Dark Matter*, The Astrophysical Journal **648**, L109 (2006).

[59] G. D. Starkman, *Modifying gravity: You cannot always get what you want*, Philosophical Transactions of the Royal Society A: Mathematical, Physical and Engineering Sciences **369**, 5018 (2011).

[60] H. Niikura, M. Takada, N. Yasuda, R. H. Lupton, T. Sumi, S. More, T. Kurita, S. Sugiyama, A. More, M. Oguri, and M. Chiba, *Microlensing constraints on primordial black holes with Subaru/HSC Andromeda observations*, Nature Astronomy **3**, 524 (2019).

[61] B. C. Lacki and J. F. Beacom, *Primordial black holes as dark matter: Almost all or almost nothing*, Astrophysical Journal Letters **720**, 67 (2010).

[62] J. R. Espinosa, D. Racco, and A. Riotto, *Cosmological Signature of the Standard Model Higgs Vacuum Instability: Primordial Black Holes as Dark Matter*, Physical Review Letters **120**, 121301 (2018).

[63] S. Clesse and J. García-Bellido, *Seven hints for primordial black hole dark matter*, Physics of the Dark Universe **22**, 137 (2018).

[64] M. S. Turner, *Dark matter: Theoretical perspectives*, in *Proceedings of the National Academy of Sciences of the United States of America*, volume 90, pages 4827–4834, National Academy of Sciences, 1993.

[65] J. Alexander et al., *Dark Sectors 2016 Workshop: Community Report*, **1**, 18 (2016).

[66] A. Fradette, M. Pospelov, J. Pradler, and A. Ritz, *Cosmological beam dump: Constraints on dark scalars mixed with the Higgs boson*, Physical Review D **99**, 075004 (2019).

[67] R. Giacconi, H. Gursky, F. R. Paolini, and B. B. Rossi, *Evidence for x rays from sources outside the solar system*, Physical Review Letters **9**, 439 (1962).

[68] A. E. Metzger, E. C. Anderson, M. A. Van Dilla, and J. R. Arnold, *Detection of an interstellar flux of gamma-rays [1]*, Nature **204**, 766 (1964).

[69] K. Gendreau, R. Mushotzky, A. Fabian, S. Holt, T. Kii, P. Serlemitsos, Y. Ogasaka, Y. Tanaka, M. Bautz, Y. Fukazawa, Y. Ishisaki,

Y. Kohmura, K. Makishima, M. Tashiro, Y. Tsusaka, H. Kunieda, G. Ricker, and R. Vanderspek, *ASCA Observations of the Spectrum of the X-Ray Background*, Publications of the Astronomical Society of Japan **47**, 5 (1995).

[70] G. Hasinger, R. Burg, R. Giacconi, M. Schmidt, J. Trümper, and G. Zamorani, *The ROSAT Deep Survey I. X-ray sources in the Lockman Field*, Astronomy and Astrophysics **329**, 482 (1998).

[71] P. Sreekumar et al., *EGRET Observations of the Extragalactic Gamma-Ray Emission*, The Astrophysical Journal **494**, 523 (1998).

[72] B. A. Cooke, R. E. Griffiths, and K. A. Pounds, *Evidence for a Galactic Component of the Diffuse X-Ray Background*, in *Non-Solar X- and Gamma-Ray Astronomy*, pages 280–288, Springer Netherlands, 1970.

[73] R. D. Bleach, E. A. Boldt, S. S. Holt, D. A. Schwartz, and P. J. Serlemitsos, *X-Ray Emission from the Galactic Disk*, The Astrophysical Journal **174**, L101 (1972).

[74] M. Revnivtsev, S. Sazonov, M. Gilfanov, E. Churazov, and R. Sunyaev, *Origin of the Galactic ridge X-ray emission*, Astronomy and Astrophysics **452**, 169 (2006).

[75] M. Revnivtsev, A. Vikhlinin, and S. Sazonov, *Resolving the Galactic ridge X-ray background*, Astronomy and Astrophysics **473**, 857 (2007).

[76] M. Revnivtsev, S. Sazonov, E. Churazov, W. Forman, A. Vikhlinin, and R. Sunyaev, *Discrete sources as the origin of the Galactic X-ray ridge emission*, Nature **458**, 1142 (2009).

[77] D. E. Gruber, J. L. Matteson, L. E. Peterson, and G. V. Jung, *The Spectrum of Diffuse Cosmic Hard X-Rays Measured with HEAO 1*, The Astrophysical Journal **520**, 124 (1999).

[78] P. Madau, G. Ghisellini, and A. C. Fabian, *The unified Seyfert scheme and the origin of the cosmic X-ray background*, Monthly Notices of the Royal Astronomical Society **270**, L17 (1994).

[79] T. Shanks, I. Georgantopoulos, G. C. Stewart, K. A. Pounds, B. J. Boyle, and R. E. Griffiths, *The origin of the cosmic X-ray background*, Nature **353**, 315 (1991).

[80] G. Hasinger, *The X-ray background and AGNs*, in *Nuclear Physics B - Proceedings Supplements*, volume 132, pages 86–96, Elsevier, 2004.

[81] L.-S. The, M. D. Leising, and D. D. Clayton, *The cosmic gamma-ray background from Type IA supernovae*, The Astrophysical Journal **403**, 32 (1993).

[82] K. Watanabe, D. H. Hartmann, M. D. Leising, and L. S. The, *The Diffuse Gamma-Ray Background from Supernovae*, The Astrophysical Journal **516**, 285 (1999).

[83] W. T. Vestrand, J. G. Stacy, and P. Sreekumar, *High-Energy Gamma Rays from the BL Lacertae Object PKS 2155-304*, The Astrophysical Journal **454**, L93 (1995).

[84] F. W. Stecker, O. C. de Jager, and M. H. Salamon, *Predicted Extragalactic T[CLC]e[/CLC]V Gamma-Ray Sources*, The Astrophysical Journal **473**, L75 (1996).

[85] B. Z. Kapanadze, *X-ray Selected BL Lacertae Objects: Catalogue and Statistical Properties*, in *Young Scientists' Conference on Astronomy and Space Physics (YSC 2011)*, Kyiv, 2011, Taras Shevchenko National University of Kyiv.

[86] E. Bulbul, M. Markevitch, A. Foster, R. K. Smith, M. Loewenstein, and S. W. Randall, *Detection of an unidentified emission line in the stacked x-ray spectrum of galaxy clusters*, Astrophysical Journal **789**, 13 (2014).

[87] A. Boyarsky, O. Ruchayskiy, D. Iakubovskyi, and J. Franse, *Unidentified line in X-ray spectra of the andromeda galaxy and perseus galaxy cluster*, Physical Review Letters **113**, 251301 (2014).

[88] J. P. Conlon, F. Day, N. Jennings, S. Krippendorf, and M. Rummel, *Consistency of Hitomi, XMM-Newton, and Chandra 3.5 keV data from Perseus*, Physical Review D **96**, 123009 (2017).

[89] N. Cappelluti, E. Bulbul, A. Foster, P. Natarajan, M. C. Urry, M. W. Bautz, F. Civano, E. Miller, and R. K. Smith, *Searching for the 3.5 keV Line in the Deep Fields with Chandra : The 10 Ms Observations*, The Astrophysical Journal **854**, 179 (2018).

[90] E. Carlson, T. Jeltema, and S. Profumo, *Where do the 3.5 keV photons come from? A morphological study of the Galactic Center and of Perseus*, Journal of Cosmology and Astroparticle Physics **2015**, 009 (2015).

[91] L. Gu, J. Kaastra, A. J. Raassen, P. D. Mullen, R. S. Cumbee, D. Lyons, and P. C. Stancil, *A novel scenario for the possible X-ray line feature at ∼ 3.5 keV: Charge exchange with bare sulfur ions*, Astronomy and Astrophysics **584**, 11 (2015).

[92] A. Boyarsky, J. Franse, D. Iakubovskyi, and O. Ruchayskiy, *Checking the Dark Matter Origin of a 3.53 keV Line with the Milky Way Center*, Physical Review Letters **115**, 161301 (2015).

[93] T. Jeltema and S. Profumo, *Discovery of a 3.5 keV line in the Galactic Centre and a critical look at the origin of the line across astronomical targets*, Monthly Notices of the Royal Astronomical Society **450**, 2143 (2015).

[94] S. Riemer-Sørensen, *Constraints on the presence of a 3.5 keV dark matter emission line from Chandra observations of the Galactic centre*, Astronomy and Astrophysics **590**, 71 (2016).

[95] C. Dessert, N. L. Rodd, and B. R. Safdi, *The dark matter interpretation of the 3.5-keV line is inconsistent with blank-sky observations*, Science **367**, 1465 (2020).

[96] D. Iakubovskyi, *Observation of the new emission line at ˜3.5 keV in X-ray spectra of galaxies and galaxy clusters*, Advances in Astronomy and Space Physics **6**, 3 (2016).

[97] A. A. Penzias and R. W. Wilson, *A Measurement of Excess Antenna Temperature at 4080 Mc/s.*, The Astrophysical Journal **142**, 419 (1965).

[98] A. McKellar, *Molecular Lines from the Lowest States of Diatomic Molecules Composed of Atoms Probably Present in Interstellar Spac*, Publications of the Dominion Astrophysical Observatory **7**, 251 (1941).

[99] C. L. Bennett et al., *Nine-year Wilkinson Microwave Anisotropy Probe (WMAP) observations: Final maps and results*, Astrophysical Journal, Supplement Series **208**, 20 (2013).

[100] P. J. E. Peebles, *Recombination of the Primeval Plasma*, The Astrophysical Journal **153**, 1 (1968).

[101] Y. Zeldovich, V. Kurt, and R. Syunyaev, *Recombination of Hydrogen in the Hot Model of the Universe*, Zhurnal Eksperimentalnoi i Teoreticheskoi Fiziki **55**, 278 (1968).

[102] D. S. Gorbunov and V. A. Rubakov, *Introduction to the theory of the early universe: Hot big bang theory*, World Scientific Publishing Co., 2011.

[103] N. W. Boggess, J. C. Mather, R. Weiss, C. L. Bennett, E. S. Cheng, E. Dwek, S. Gulkis, M. G. Hauser, M. A. Janssen, T. Kelsall, S. S. Meyer, S. H. Moseley, T. L. Murdock, R. A. Shafer, R. F. Silverberg, G. F. Smoot, D. T. Wilkinson, and E. L. Wright, *The COBE mission - Its design and performance two years after launch*, The Astrophysical Journal **397**, 420 (1992).

[104] G. F. Smoot, *The Cosmic Microwave Background Spectrum*, in *Strasbourg NATO school on the CMB and Cosmology*, 1997.

[105] M. White, *Anisotropies in the CMB*, in *Meeting of the Division of Particles and Fields of the American Physical Society (DPF 99)*, edited by K. Arisaka and Z. Bern, Los Angeles, 1999, University of California.

[106] J. C. Mather et al., *Measurement of the cosmic microwave background spectrum by the COBE FIRAS instrument*, The Astrophysical Journal **420**, 439 (1994).

[107] D. J. Fixsen, E. S. Cheng, J. M. Gales, J. C. Mather, R. A. Shafer, and E. L. Wright, *The Cosmic Microwave Background Spectrum from the Full COBE FIRAS Data Set*, The Astrophysical Journal **473**, 576 (1996).

[108] E. L. Wright, J. C. Mather, D. J. Fixsen, A. Kogut, R. A. Shafer, C. L. Bennett, N. W. Boggess, E. S. Cheng, R. F. Silverberg, G. F. Smoot, and R. Weiss, *Interpretation of the COBE FIRAS CMBR spectrum*, The Astrophysical Journal **420**, 450 (1994).

[109] R. H. Brandenberger, *Formation of Structure in the Universe*, in *Cosmology and gravitation II : VIII Brazilian School of Cosmology and Gravitation*, edited by M. Novello, Rio de Janeiro, 1995, Editions Frontieres.

[110] W. Hu and M. White, *The Damping Tail of Cosmic Microwave Background Anisotropies*, The Astrophysical Journal **479**, 568 (1997).

[111] E. L. Wright, *Theoretical Overview of Cosmic Microwave Background Anisotropy*, Carnegie Observatories Astrophysics Series **2** (2003).

[112] J. Silk, *Cosmic Black-Body Radiation and Galaxy Formation*, The Astrophysical Journal **151**, 459 (1968).

[113] W. Hu, N. Sugiyama, and J. Silk, *The physics of microwave background anisotropies*, Nature **386**, 37 (1997).

[114] R. K. Sachs and A. M. Wolfe, *Perturbations of a Cosmological Model and Angular Variations of the Microwave Background*, The Astrophysical Journal **147**, 73 (1967).

[115] M. J. Rees and D. W. Sciama, *Large-scale density inhomogeneities in the universe*, Nature **217**, 511 (1968).

[116] R. Barkana and A. Loeb, *In the beginning: The first sources of light and the reionization of the universe*, Physics Report **349**, 125 (2001).

[117] J. P. Ostriker and E. T. Vishniac, *Generation of microwave background fluctuations from nonlinear perturbations at the ERA of galaxy formation*, The Astrophysical Journal **306**, L51 (1986).

[118] E. T. Vishniac, *Reionization and small-scale fluctuations in the microwave background*, The Astrophysical Journal **322**, 597 (1987).

[119] N. Aghanim, F. X. Désert, J. L. Puget, and R. Gispert, *Ionization by early quasars and cosmic microwave background anisotropies*, Astronomy and Astrophysics **311**, 1 (1996).

[120] R. Sunyaev and Y. Zeldovich, *The Observations of Relic Radiation as a Test of the Nature of X-Ray Radiation from the Clusters of Galaxies*, Comments on Astrophysics and Space Physics **4**, 173 (1972).

[121] L. Husdal, *On effective degrees of freedom in the early Universe*, Galaxies **4**, 78 (2016).

[122] A. D. Dolgov, *Neutrinos in cosmology*, Physics Report **370**, 333 (2002).

[123] B. Follin, L. Knox, M. Millea, and Z. Pan, *First Detection of the Acoustic Oscillation Phase Shift Expected from the Cosmic Neutrino Background*, Physical Review Letters **115**, 091301 (2015).

[124] S. Betts et al., *Development of a Relic Neutrino Detection Experiment at PTOLEMY: Princeton Tritium Observatory for Light, Early-Universe, Massive-Neutrino Yield*, (2013).

[125] K. Ichikawa, T. Sekiguchi, and T. Takahashi, *Probing the effective number of neutrino species with the cosmic microwave background*, Physical Review D - Particles, Fields, Gravitation and Cosmology **78**, 083526 (2008).

[126] S. Riemer-Sorensen, D. Parkinson, and T. M. Davis, *What is half a neutrino? reviewing cosmological constraints on neutrinos and dark radiation*, 2013.

[127] G. Mangano, G. Miele, S. Pastor, T. Pinto, O. Pisanti, and P. D. Serpico, *Relic neutrino decoupling including flavour oscillations*, Nuclear Physics B **729**, 221 (2005).

[128] P. F. De Salas and S. Pastor, *Relic neutrino decoupling with flavour oscillations revisited*, Journal of Cosmology and Astroparticle Physics **2016**, 051 (2016).

[129] N. Fornengo, C. W. Kim, and J. Song, *Finite temperature effects on the neutrino decoupling in the early Universe*, Physical Review D - Particles, Fields, Gravitation and Cosmology **56**, 5123 (1997).

[130] G. Mangano, G. Miele, S. Pastor, and M. Peloso, *A precision calculation of the effective number of cosmological neutrinos*, Physics Letters, Section B: Nuclear, Elementary Particle and High-Energy Physics **534**, 8 (2002).

[131] P. Langacker, S. T. Petcov, G. Steigman, and S. Toshev, *Implications of the mikheyev-smirnov-wolfenstein (MSW) mechanism of amplification of neutrino oscillations in matter*, Nuclear Physics, Section B **282**, 589 (1987).

[132] S. Hannestad, *Oscillation effects on neutrino decoupling in the early universe*, Physical Review D - Particles, Fields, Gravitation and Cosmology **65**, 830061 (2002).

[133] Z. Hou, R. Keisler, L. Knox, M. Millea, and C. Reichardt, *How massless neutrinos affect the cosmic microwave background damping tail*, Physical Review D - Particles, Fields, Gravitation and Cosmology **87**, 083008 (2013).

[134] W. Hu and M. White, *Acoustic Signatures in the Cosmic Microwave Background*, The Astrophysical Journal **471**, 30 (1996).

[135] M. Zaldarriaga and D. D. Harari, *Analytic approach to the polarization of the cosmic microwave background in flat and open universes*, Physical Review D **52**, 3276 (1995).

[136] E. Komatsu et al., *Seven-year wilkinson microwave anisotropy probe (WMAP*) observations: Cosmological interpretation*, Astrophysical Journal, Supplement Series **192**, 18 (2011).

[137] R. Keisler et al., *A measurement of the damping tail of the cosmic microwave background power spectrum with the South Pole Telescope*, Astrophysical Journal **743**, 28 (2011).

[138] S. Bashinsky and U. Seljak, *Signatures of relativistic neutrinos in CMB anisotropy and matter clustering*, Physical Review D - Particles, Fields, Gravitation and Cosmology **69**, 35 (2004).

[139] A. Coc and E. Vangioni, *Primordial nucleosynthesis*, International Journal of Modern Physics E **26** (2017).

[140] R. A. Alpher, H. Bethe, and G. Gamow, *The origin of chemical elements [1]*, Physical Review **73**, 803 (1948).

[141] R. H. Cyburt, B. D. Fields, and K. A. Olive, *Primordial nucleosynthesis with CMB inputs: Probing the early universe and light element astrophysics*, Astroparticle Physics **17**, 87 (2002).

[142] R. H. Cyburt, B. D. Fields, K. A. Olive, and T. H. Yeh, *Big bang nucleosynthesis: Present status*, Reviews of Modern Physics **88**, 015004 (2016).

[143] R. Hagedorn and J. Ranft, *Statistical thermodynamics of strong interactions at high energies*, Nuovo Cimento, Suppl. **3**, 147 (1966).

[144] R. Hagedorn, *Boiling Primordial Matter: 1968*, in *Melting Hadrons, Boiling Quarks - From Hagedorn Temperature to Ultra-Relativistic Heavy-Ion Collisions at CERN*, pages 125–138, Springer International Publishing, 2016.

[145] R. Hagedorn, *Thermodynamics of Strong Interactions at High Energy and its Consequences for Astrophysics*, Astronomy and Astrophysics **5**, 184 (1970).

[146] I. Kuznetsova and J. Rafelski, *Unstable hadrons in hot hadron gas: In the laboratory and in the early Universe*, Physical Review C - Nuclear Physics **82**, 035203 (2010).

[147] M. J. Fromerth, I. Kuznetsova, L. Labun, J. Letessier, and J. Rafelski, *From quark-gluon universe to neutrino decoupling: $200 < T < 2$ MeV*, Acta Physica Polonica B **43**, 2261 (2012).

[148] J. Bernstein, L. S. Brown, and G. Feinberg, *Cosmological helium production simplified*, Reviews of Modern Physics **61**, 25 (1989).

[149] S. Sarkar, *Big bang nucleosynthesis and physics beyond the standard model*, Reports on Progress in Physics **59**, 1493 (1996).

[150] P. A. Zyla et al., *Review of particle physics*, Progress of Theoretical and Experimental Physics **2020**, 1 (2020).

[151] P. Mumm, *Resolving the neutron lifetime puzzle*, Science **360**, 605 (2018).

[152] V. Mukhanov, *Nucleosynthesis without computer*, in *International Journal of Theoretical Physics*, volume 43, pages 669–693, Springer, 2004.

[153] C. Pitrou, A. Coc, J. P. Uzan, and E. Vangioni, *Precision big bang nucleosynthesis with improved Helium-4 predictions*, 2018.

[154] J. Hamann, J. Lesgourgues, and G. Mangano, *Using big bang nucleosynthesis in cosmological parameter extraction from the cosmic microwave background: A forecast for PLANCK*, Journal of Cosmology and Astroparticle Physics **2008**, 004 (2008).

[155] G. Steigman, *Primordial helium and the cosmic background radiation*, Journal of Cosmology and Astroparticle Physics **2010**, 029 (2010).

[156] R. H. Cyburt, B. D. Fields, and K. A. Olive, *Primordial nucleosynthesis in light of WMAP*, Physics Letters, Section B: Nuclear, Elementary Particle and High-Energy Physics **567**, 227 (2003).

[157] Y. I. Izotov, T. X. Thuan, and N. G. Guseva, *A new determination of the primordial He abundance using the He I λ10830 Å emission line: Cosmological implications*, Monthly Notices of the Royal Astronomical Society **445**, 778 (2014).

[158] E. Aver, K. A. Olive, and E. D. Skillman, *The effects of He i λ10830 on helium abundance determinations*, Journal of Cosmology and Astroparticle Physics **2015**, 011 (2015).

[159] A. Peimbert, M. Peimbert, and V. Luridiana, *The primordial helium abundance and the number of neutrino families*, Revista Mexicana de Astronomia y Astrofisica **52**, 419 (2016).

[160] L. D. Anderson, T. M. Bania, J. M. Jackson, D. P. Clemens, M. Heyer, R. Simon, R. Y. Shah, and J. M. Rathborne, *The molecular properties of galactic h II regions*, Astrophysical Journal, Supplement Series **181**, 255 (2009).

[161] Y. I. Izotov and T. X. Thuan, *The primordial abundance of 4He: Evidence for non-standard big bang nucleosynthesis*, Astrophysical Journal Letters **710**, 67 (2010).

[162] E. Aver, K. A. Olive, and E. D. Skillman, *A new approach to systematic uncertainties and self-consistency in helium abundance determinations*, Journal of Cosmology and Astroparticle Physics **2010**, 003 (2010).

[163] M. Fumagalli, J. M. O'Meara, and J. X. Prochaska, *Detection of pristine gas two billion years after the big bang*, Science **334**, 1245 (2011).

[164] R. J. Cooke, M. Pettini, and C. C. Steidel, *Discovery of the most metal-poor damped Lyman α system*, Monthly Notices of the Royal Astronomical Society **467**, 802 (2017).

[165] R. J. Cooke, M. Pettini, and C. C. Steidel, *One Percent Determination of the Primordial Deuterium Abundance*, The Astrophysical Journal **855**, 102 (2018).

[166] C. L. Bennett et al., *First-Year Wilkinson Microwave Anisotropy Probe (WMAP) Observations: Preliminary Maps and Basic Results*, The Astrophysical Journal Supplement Series **148**, 1 (2003).

[167] K. Ichikawa and T. Takahashi, *Reexamining the constraint on the helium abundance from the CMB*, Physical Review D - Particles, Fields, Gravitation and Cosmology **73**, 063528 (2006).

[168] W. Hu, D. Scott, N. Sugiyama, and M. White, *Effect of physical assumptions on the calculation of microwave background anisotropies*, Physical Review D **52**, 5498 (1995).

[169] S. Seager, D. D. Sasselov, and D. Scott, *A New Calculation of the Recombination Epoch*, The Astrophysical Journal **523**, L1 (1999).

[170] R. Trotta and S. H. Hansen, *Constraining the helium abundance with CMB data*, Physical Review D - Particles, Fields, Gravitation and Cosmology **69**, 023509 (2004).

[171] A. Boyarsky, M. Ovchynnikov, O. Ruchayskiy, and V. Syvolap, *Improved BBN constraints on Heavy Neutral Leptons*, (2020).

[172] M. Pettini and R. Cooke, *A new, precise measurement of the primordial abundance of deuterium*, Monthly Notices of the Royal Astronomical Society **425**, 2477 (2012).

[173] R. J. Cooke, M. Pettini, R. A. Jorgenson, M. T. Murphy, and C. C. Steidel, *Precision measures of the primordial abundance of deuterium*, Astrophysical Journal **781**, 31 (2014).

[174] D. J. Mullan and J. L. Linsky, *Nonprimordial Deuterium in the Interstellar Medium*, The Astrophysical Journal **511**, 502 (1999).

[175] T. Prodanović and B. D. Fields, *On Nonprimordial Deuterium Production by Accelerated Particles*, The Astrophysical Journal **597**, 48 (2003).

[176] T. Adams, *The detectability of deuterium Lyman alpha in QSOs*, Astronomy and Astrophysics **50**, 461 (1976).

[177] S. Burles and D. Tytler, *The Deuterium Abundance toward QSO 1009+2956*, The Astrophysical Journal **507**, 732 (1998).

[178] J. M. O'Meara, D. Tytler, D. Kirkman, N. Suzuki, J. X. Prochaska, D. Lubin, and A. M. Wolfe, *The Deuterium to Hydrogen Abundance Ratio toward a Fourth QSO: HS 0105+1619*, The Astrophysical Journal **552**, 718 (2001).

[179] M. Pettini and D. V. Bowen, *A New Measurement of the Primordial Abundance of Deuterium: Toward Convergence with the Baryon Density from the Cosmic Microwave Background?*, The Astrophysical Journal **560**, 41 (2001).

[180] S. A. Levshakov, M. Dessauges-Zavadsky, S. D'Odorico, and P. Molaro, *Molecular Hydrogen, Deuterium, and Metal Abundances in the Damped Lyα System at z abs = 3.025 toward Q0347 − 3819*, The Astrophysical Journal **565**, 696 (2002).

[181] D. Kirkman, D. Tytler, N. Suzuki, J. M. O'Meara, and D. Lubin, *The Cosmological Baryon Density from the Deuterium-to-Hydrogen Ratio in QSO Absorption Systems: D/H toward Q1243+3047*, The Astrophysical Journal Supplement Series **149**, 1 (2003).

[182] J. M. O'Meara, S. Burles, J. X. Prochaska, G. E. Prochter, R. A. Bernstein, and K. M. Burgess, *The Deuterium-to-Hydrogen Abundance Ratio toward the QSO SDSS J155810.16-003120.0*, The Astrophysical Journal **649**, L61 (2006).

[183] R. Srianand, N. Gupta, P. Petitjean, P. Noterdaeme, and C. Ledoux, *Detection of 21-cm, H2 and deuterium absorption at $z > 3$ along the line of sight to J1337+3152*, Monthly Notices of the Royal Astronomical Society **405**, 1888 (2010).

[184] P. Noterdaeme, S. López, V. Dumont, C. Ledoux, P. Molaro, and P. Petitjean, *Deuterium at high redshift: Primordial abundance in the z abs = 2.621 damped Ly-α system towards CTQ 247*, 2012.

[185] P. A. Ade et al., *Planck 2015 results: XIII. Cosmological parameters*, Astronomy and Astrophysics **594**, A13 (2016).

[186] A. Coc, P. Petitjean, J. P. Uzan, E. Vangioni, P. Descouvemont, C. Iliadis, and R. Longland, *New reaction rates for improved primordial D/H calculation and the cosmic evolution of deuterium*, Physical Review D - Particles, Fields, Gravitation and Cosmology **92**, 123526 (2015).

[187] O. Pisanti, G. Mangano, G. Miele, and P. Mazzella, *Primordial Deuterium after LUNA: Concordances and error budget*, Journal of Cosmology and Astroparticle Physics **2021** (2021).

[188] J. M. Overduin and P. S. Wesson, *Dark matter and background light*, Physics Reports **402**, 267 (2004).

[189] G. Bertone, W. Buchmüller, L. Covi, and A. Ibarra, *Gamma-rays from decaying dark matter*, Journal of Cosmology and Astroparticle Physics **2007**, 003 (2007).

[190] A. Boyarsky, J. Nevalainen, and O. Ruchayskiy, *Constraints on the parameters of radiatively decaying dark matter from the dark matter halos of the Milky Way and Ursa Minor*, Astronomy and Astrophysics **471**, 51 (2007).

[191] J. A. Cembranos and L. E. Strigari, *Diffuse MeV gamma rays and galactic 511 keV line from decaying WIMP dark matter*, Physical Review D - Particles, Fields, Gravitation and Cosmology **77**, 123519 (2008).

[192] H. Yüksel and M. D. Kistler, *Circumscribing late dark matter decays model-independently*, Physical Review D - Particles, Fields, Gravitation and Cosmology **78**, 023502 (2008).

[193] A. Boyarsky, D. Malyshev, A. Neronov, and O. Ruchayskiy, *Constraining dark matter properties with SPI*, Monthly Notices of the Royal Astronomical Society **387**, 1345 (2008).

[194] A. Boyarsky and O. Ruchayskiy, *Bounds on light dark matter*, in *Proceedings of the 4th Patras Workshop on Axions, WIMPs and WISPs, PATRAS 2008*, edited by A. Lindner, J. Redondo, and A. Ringwald, pages 31–34, Hamburg, 2008, Verlag Deutsches Elektronen-Synchrotron.

[195] R. Essig, E. Kuflik, S. D. McDermott, T. Volansky, and K. M. Zurek, *Constraining light dark matter with diffuse X-ray and gamma-ray observations*, Journal of High Energy Physics **2013**, 193 (2013).

[196] T. Asaka, J. Hashiba, M. Kawasaki, and T. Yanagida, *Spectrum of background x-rays from moduli dark matter*, Physical Review D - Particles, Fields, Gravitation and Cosmology **58**, 235071 (1998).

[197] J. F. Navarro, C. S. Frenk, and S. D. M. White, *The Structure of Cold Dark Matter Halos*, The Astrophysical Journal **462**, 563 (1996).

[198] J. F. Navarro, C. S. Frenk, and S. D. M. White, *A Universal Density Profile from Hierarchical Clustering*, The Astrophysical Journal **490**, 493 (1997).

[199] R. Toldrà, *Photon spectrum produced by the late decay of a cosmic neutrino background*, Physical Review D - Particles, Fields, Gravitation and Cosmology **60**, 083503 (1999).

[200] K. Abazajian, G. M. Fuller, and W. H. Tucker, *Direct Detection of Warm Dark Matter in the X-Ray*, The Astrophysical Journal **562**, 593 (2001).

[201] A. Boyarsky, A. Neronov, O. Ruchayskiy, and M. Shaposhnikov, *Constraints on sterile neutrinos as dark matter candidates from the diffuse X-ray background*, Monthly Notices of the Royal Astronomical Society **370**, 213 (2006).

[202] L. Bouchet, E. Jourdain, J.-P. Roques, A. Strong, R. Diehl, F. Lebrun, and R. Terrier, *INTEGRAL SPI All-Sky View in Soft Gamma Rays: A Study of Point-Source and Galactic Diffuse Emission*, The Astrophysical Journal **679**, 1315 (2008).

[203] W. Hu and J. Silk, *Thermalization constraints and spectral distortions for massive unstable relic particles*, Physical Review Letters **70**, 2661 (1993).

[204] J. Chluba and D. Jeong, *Teasing bits of information out of the CMB energy spectrum*, Monthly Notices of the Royal Astronomical Society **438**, 2065 (2014).

[205] W. Hu and J. Silk, *Thermalization and spectral distortions of the cosmic background radiation*, Physical Review D **48**, 485 (1993).

Version of July 22, 2021– Created July 22, 2021 - 14:39

[206] J. Chluba and R. A. Sunyaev, *The evolution of CMB spectral distortions in the early Universe*, Monthly Notices of the Royal Astronomical Society **419**, 1294 (2012).

[207] C. Burigana, L. Danese, and G. De Zotti, *Formation and evolution of early distortions of the microwave background spectrum : a numerical study*, Astronomy and astrophysics (Berlin. Print) **246**, 49 (1991).

[208] R. A. Sunyaev and Y. B. Zeldovich, *Small-scale fluctuations of relic radiation*, Astrophysics and Space Science **7**, 3 (1970).

[209] Y. B. Zeldovich and R. A. Sunyaev, *The interaction of matter and radiation in a hot-model universe*, Astrophysics and Space Science **4**, 301 (1969).

[210] P. Zhang, U. L. Pen, and H. Trac, *The temperature of the intergalactic medium and the Compton y parameter*, Monthly Notices of the Royal Astronomical Society **355**, 451 (2004).

[211] J. Chluba, *Distinguishing different scenarios of early energy release with spectral distortions of the cosmic microwave background*, Monthly Notices of the Royal Astronomical Society **436**, 2232 (2013).

[212] A. Fradette and M. Pospelov, *BBN for the LHC: Constraints on lifetimes of the Higgs portal scalars*, Physical Review D **96**, 075033 (2017).

[213] S. Hannestad, *What is the lowest possible reheating temperature?*, Physical Review D - Particles, Fields, Gravitation and Cosmology **70**, 043506 (2004).

[214] A. Boyarsky, M. Ovchynnikov, N. Sabti, and V. Syvolap, *When FIMPs Decay into Neutrinos: The $N_{\rm eff}$ Story*, (2021).

[215] K. Jedamzik and M. Pospelov, *Big Bang nucleosynthesis and particle dark matter*, New Journal of Physics **11**, 105028 (2009).

[216] M. Pospelov and J. Pradler, *Metastable GeV-scale particles as a solution to the cosmological lithium problem*, Physical Review D - Particles, Fields, Gravitation and Cosmology **82**, 103514 (2010).

[217] M. Pospelov and J. Pradler, *Big bang nucleosynthesis as a probe of new physics*, Annual Review of Nuclear and Particle Science **60**, 539 (2010).

[218] M. Kawasaki, K. Kohri, T. Moroi, and Y. Takaesu, *Revisiting big-bang nucleosynthesis constraints on long-lived decaying particles*, Physical Review D **97**, 023502 (2018).

[219] D. N. Schramm and R. V. Wagoner, *Element Production in the Early Universe*, Annual Review of Nuclear Science **27**, 37 (1977).

[220] J. Yang, M. S. Turner, D. N. Schramm, G. Steigman, and K. A. Olive, *Primordial nucleosynthesis - A critical comparison of theory and observation*, The Astrophysical Journal **281**, 493 (1984).

[221] R. J. Scherrer and M. S. Turner, *Primordial nucleosynthesis with decaying particles. I - Entropy-producing decays. II - Inert decays*, The Astrophysical Journal **331**, 19 (1988).

[222] P. F. Depta, M. Hufnagel, K. Schmidt-Hoberg, and S. Wild, *BBN constraints on the annihilation of MeV-scale dark matter*, Journal of Cosmology and Astroparticle Physics **2019**, 029 (2019).

[223] J. Alvey, N. Sabti, M. Escudero, and M. Fairbairn, *Improved BBN constraints on the variation of the gravitational constant*, European Physical Journal C **80**, 148 (2020).

[224] N. Sabti, A. Magalich, and A. Filimonova, *An extended analysis of Heavy Neutral Leptons during Big Bang Nucleosynthesis*, Journal of Cosmology and Astroparticle Physics **2020**, 056 (2020).

[225] N. Sabti, A. Magalich, and A. Filimonova, *An extended analysis of Heavy Neutral Leptons during Big Bang Nucleosynthesis*, Journal of Cosmology and Astroparticle Physics **2020**, 056 (2020).

[226] K. Bondarenko, A. Boyarsky, T. Bringmann, M. Hufnagel, K. Schmidt-Hoberg, and A. Sokolenko, *Direct detection and complementary constraints for sub-GeV dark matter*, Journal of High Energy Physics **2020**, 118 (2020).

[227] A. D. Dolgov, S. H. Hansen, G. Raffelt, and D. V. Semikoz, *Cosmological and astrophysical bounds on a heavy sterile neutrino and the KARMEN anomaly*, Nuclear Physics B **580**, 331 (2000).

[228] K. Kohri, *Primordial nucleosynthesis and hadronic decay of a massive particle with a relatively short lifetime*, Physical Review D **64**, 043515 (2001).

[229] D. Lindley, *Cosmological constraints on the lifetime of massive particles*, The Astrophysical Journal **294**, 1 (1985).

[230] J. Ellis, D. V. Nanopoulos, and S. Sarkar, *The cosmology of decaying gravitinos*, Nuclear Physics, Section B **259**, 175 (1985).

[231] J. Audouze, D. Lindley, and J. Silk, *Big bang photosynthesis and pregalactic nucleosynthesis of light elements*, The Astrophysical Journal **293**, L53 (1985).

[232] M. Kawasaki and K. Sato, *Decay of gravitinos and photo-destruction of light elements*, Physics Letters B **189**, 23 (1987).

[233] O. Bertolami and R. Rosenfeld, *The higgs portal and an unified model for dark energy and dark matter*, International Journal of Modern Physics A **23**, 4817 (2008).

[234] M. Pospelov, A. Ritz, and M. Voloshin, *Bosonic super-WIMPs as keV-scale dark matter*, Physical Review D - Particles, Fields, Gravitation and Cosmology **78**, 115012 (2008).

[235] F. Piazza and M. Pospelov, *Sub-eV scalar dark matter through the super-renormalizable Higgs portal*, Physical Review D - Particles, Fields, Gravitation and Cosmology **82**, 043533 (2010).

[236] S. Heeba, F. Kahlhoefer, and P. Stöcker, *Freeze-in production of decaying dark matter in five steps*, Journal of Cosmology and Astroparticle Physics **2018**, 048 (2018).

[237] F. Bezrukov and D. Gorbunov, *Light inflaton hunter's guide*, Journal of High Energy Physics **2010**, 10 (2010).

[238] F. Bezrukov and D. Gorbunov, *Light inflaton after LHC8 and WMAP9 results*, Journal of High Energy Physics **2013**, 140 (2013).

[239] Z. Chacko, H. S. Goh, and R. Harnik, *Natural electroweak breaking from a mirror symmetry*, Physical Review Letters **96**, 231802 (2006).

[240] N. Craig and K. Howe, *Doubling down on naturalness with a supersymmetric twin Higgs*, Journal of High Energy Physics **2014**, 140 (2014).

[241] T. Flacke, C. Frugiuele, E. Fuchs, R. S. Gupta, and G. Perez, *Phenomenology of relaxion-Higgs mixing*, Journal of High Energy Physics **2017**, 50 (2017).

[242] M. Ahlers, J. Jaeckel, J. Redondo, and A. Ringwald, *Probing hidden sector photons through the Higgs window*, Physical Review D - Particles, Fields, Gravitation and Cosmology **78**, 075005 (2008).

[243] J. Berger, K. Jedamzik, and D. G. Walker, *Cosmological constraints on decoupled dark photons and dark Higgs*, Journal of Cosmology and Astroparticle Physics **2016**, 032 (2016).

[244] M. D'Onofrio and K. Rummukainen, *Standard model cross-over on the lattice*, Physical Review D **93**, 025003 (2016).

[245] D. O'Connell, M. J. Ramsey-Musolf, and M. B. Wise, *Minimal extension of the standard model scalar sector*, Physical Review D - Particles, Fields, Gravitation and Cosmology **75**, 037701 (2007).

[246] I. Boiarska, K. Bondarenko, A. Boyarsky, V. Gorkavenko, M. Ovchynnikov, and A. Sokolenko, *Phenomenology of GeV-scale scalar portal*, Journal of High Energy Physics **2019**, 1 (2019).

[247] J. D. Clarke, R. Foot, and R. R. Volkas, *Phenomenology of a very light scalar (100MeV $<$ mh $<$ 10 GeV) mixing with the SM Higgs*, Journal of High Energy Physics **2014**, 1 (2014).

[248] A. Djouadi, *The anatomy of electroweak symmetry breaking. Tome I: The Higgs boson in the Standard Model*, Physics Reports **457**, 1 (2008).

[249] M. Voloshin, *Once more on the role of the gluon mechanism in the interaction of a light Higgs boson with hadrons*, in *The Standard Model Higgs Boson*, edited by M. EINHORN, volume 8 of *Current Physics-Sources and Comments*, pages 91–95, Elsevier, 1991.

[250] T. N. Truong and R. S. Willey, *Branching ratios for decays of light Higgs bosons*, Physical Review D **40**, 3635 (1989).

[251] J. F. Donoghue, J. Gasser, and H. Leutwyler, *The decay of a light Higgs boson*, Nuclear Physics, Section B **343**, 341 (1990).

[252] E. Duchovni, E. Gross, and G. Mikenberg, *Motivation and technique for light-Higgs-boson search*, Physical Review D **39**, 365 (1989).

[253] J. F. Gunion, H. E. Haber, G. L. Kane, and S. Dawson, *The Higgs Hunter's Guide*, Brookhaven Nat. Lab., 1989.

[254] A. Monin, A. Boyarsky, and O. Ruchayskiy, *Hadronic decays of a light Higgs-like scalar*, Physical Review D **99**, 015019 (2019).

[255] M. W. Winkler, *Decay and detection of a light scalar boson mixing with the Higgs boson*, Physical Review D **99**, 015018 (2019).

[256] A. Pich, *Chiral perturbation theory*, Reports on Progress in Physics **58**, 563 (1995).

[257] B. Hyams, C. Jones, P. Weilhammer, W. Blum, H. Dietl, G. Grayer, W. Koch, E. Lorenz, G. Lütjens, W. Männer, J. Meissburger, W. Ochs, U. Stierlin, and F. Wagner, *$\pi\pi$ Phase-shift analysis from 600 to 1900 MeV*, Nuclear Physics, Section B **64**, 134 (1973).

[258] D. Besak, *Thermal particle production in the early Universe*, PhD thesis, Bielefeld University, 2010.

[259] D. J. Kapner, T. S. Cook, E. G. Adelberger, J. H. Gundlach, B. R. Heckel, C. D. Hoyle, and H. E. Swanson, *Tests of the gravitational inverse-square law below the dark-energy length scale*, Physical Review Letters **98**, 021101 (2007).

[260] A. O. Sushkov, W. J. Kim, D. A. R. Dalvit, and S. K. Lamoreaux, *New Experimental Limits on Non-Newtonian Forces in the Micrometer Range*, Physical Review Letters **107**, 171101 (2011).

[261] E. Hardy and R. Lasenby, *Stellar cooling bounds on new light particles: plasma mixing effects*, Journal of High Energy Physics **2017**, 1 (2017).

[262] R. Essig, R. Harnik, J. Kaplan, and N. Toro, *Discovering new light states at neutrino experiments*, Physical Review D - Particles, Fields, Gravitation and Cosmology **82**, 113008 (2010).

[263] G. Krnjaic, *Probing light thermal dark matter with a Higgs portal mediator*, Physical Review D **94**, 073009 (2016).

[264] F. Bergsma et al., *Search for axion-like particle production in 400 GeV proton-copper interactions*, Physics Letters B **157**, 458 (1985).

[265] R. Aaij et al., *Search for long-lived scalar particles in $B^+ \to K^+\chi(\mu^+\mu^-)$ decays*, Physical Review D **95**, 071101 (2017).

[266] S. Alekhin et al., *A facility to search for hidden particles at the CERN SPS: The SHiP physics case*, Reports on Progress in Physics **79**, 124201 (2016).

[267] E. G. Adelberger, B. R. Heckel, and A. E. Nelson, *Tests of the Gravitational Inverse-Square Law*, Annual Review of Nuclear and Particle Science **53**, 77 (2003).

[268] G. G. Raffelt, *Stars as laboratories for fundamental physics: The astrophysics of neutrinos, axions, and other weakly interacting particles*, 1996.

[269] S. Dodelson and L. M. Widrow, *Sterile neutrinos as dark matter*, Physical Review Letters **72**, 17 (1994).

[270] A. Boyarsky, M. Drewes, T. Lasserre, S. Mertens, and O. Ruchayskiy, *Sterile neutrino Dark Matter*, Progress in Particle and Nuclear Physics **104**, 1 (2019).

[271] M. Drewes, *The phenomenology of right handed neutrinos*, International Journal of Modern Physics E **22** (2013).

[272] T. Asaka, S. Blanchet, and M. Shaposhnikov, *The νMSM, dark matter and neutrino masses*, Physics Letters B **631**, 151 (2005).

[273] T. Asaka and M. Shaposhnikov, *The νMSM, dark matter and baryon asymmetry of the universe*, Physics Letters B **620**, 17 (2005).

[274] D. Gorbunov and M. Shaposhnikov, *How to find neutral leptons of the νMSM?*, Journal of High Energy Physics **2007**, 015 (2007).

[275] K. Bondarenko, A. Boyarsky, D. Gorbunov, and O. Ruchayskiy, *Phenomenology of GeV-scale heavy neutral leptons*, Journal of High Energy Physics **2018**, 1 (2018).

[276] A. Atre, T. Han, S. Pascoli, and B. Zhang, *The search for heavy Majorana neutrinos*, Journal of High Energy Physics **2009**, 030 (2009).

[277] P. B. Pal and L. Wolfenstein, *Radiative decays of massive neutrinos*, Physical Review D **25**, 766 (1982).

[278] D. Nötzold and G. Raffelt, *Neutrono dispersion at finite temperature and density*, Nuclear Physics, Section B **307**, 924 (1988).

[279] P. Elmfors, D. Grasso, and G. Raffelt, *Neutrino dispersion in magnetized media and spin oscillations in the early Universe*, Nuclear Physics B **479**, 3 (1996).

[280] K. Abazajian, G. M. Fuller, and M. Patel, *Sterile neutrino hot, warm, and cold dark matter*, Physical Review D - Particles, Fields, Gravitation and Cosmology **64**, 22 (2001).

[281] G. B. Gelmini, P. Lu, and V. Takhistov, *Cosmological dependence of non-resonantly produced sterile neutrinos*, Journal of Cosmology and Astroparticle Physics **2019**, 047 (2019).

[282] J. Edsjö and P. Gondolo, *Neutralino relic density including coannihilations*, Physical Review D - Particles, Fields, Gravitation and Cosmology **56**, 1879 (1997).

[283] G. Aad et al., *Search for heavy Majorana neutrinos with the ATLAS detector in pp collisions at s = 8 sqrts = 8 TeV*, Journal of High Energy Physics 2015 2015:7 **2015**, 1 (2015).

[284] D. Liventsev et al., *Search for heavy neutrinos at Belle*, Physical Review D - Particles, Fields, Gravitation and Cosmology **87**, 071102 (2013).

[285] *Search for heavy neutral leptons in $W^+ \to \mu^+\mu^\pm$*jet *decays*, The European Physical Journal C **81** (2021).

[286] G. Bernardi, G. Carugno, J. Chauveau, F. Dicarlo, M. Dris, J. Dumarchez, M. Ferro-Luzzi, J. M. Levy, D. Lukas, J. M. Perreau, Y. Pons, A. M. Touchard, and F. Vannucci, *Further limits on heavy neutrino couplings*, Physics Letters B **203**, 332 (1988).

[287] J. Dorenbosch et al., *A search for decays of heavy neutrinos in the mass range 0.5-2.8 GeV*, Physics Letters B **166**, 473 (1986).

[288] K. Abe et al., *Search for heavy neutrinos with the T2K near detector ND280*, Physical Review D **100**, 052006 (2019).

[289] A. Vaitaitis et al., *Search for neutral heavy leptons in a high-energy neutrino beam*, Physical Review Letters **83**, 4943 (1999).

[290] A. S. Kompaneets, *The Establishment of Thermal Equilibrium between Quanta and Electrons**, in *J. Exptl. Theoret. Phys. (U.S.S.H.)*, volume 4, pages 876–885, 1957.

[291] L. Danese and G. de Zotti, *Double Compton process and the spectrum of the microwave background*, Astronomy and Astrophysics **107**, 39 (1982).

Appendix A

Appendix A: Derivation of Spectral Distortion Formulae

A.1 Chemical Potential Distortion

The kinetic equation governing elastic Compton scattering, called the Kompaneets equation[290], is:

$$\left(\frac{\partial f}{\partial t}\right)_K = n_e \sigma_T \frac{T_e}{m_e} \frac{1}{x_e^2} \frac{\partial}{\partial x_e} \left[x_p^4 \left(\frac{\partial f}{\partial x_e} + f + f^2 \right) \right] \tag{A.1}$$

where $x_e \equiv \nu / T_e$ the dimensionless photon frequency[i], $f(x_e, t)$ the photon occupation number, n_e the electron density, σ_T the Thompson cross section, and T_e the electron temperature.
The equilibrium solution is a Bose-Einstein distrubution at the electron temperature [205] (which is the same as the photon temperature, since it is equilibrium), and since Compton scattering is very efficient during μ-distortion formation, we start by taking a Bose-Einstein distribution with a small chemical potential due to some injection:

$$f_{BE}(\mu) = \frac{1}{e^{x_e + \mu} - 1} \overset{\mu \ll 1}{\approx} f_{BE}(0) \left(1 - \mu \frac{e^{x_e}}{e^{x_e} - 1} \right) \tag{A.2}$$

Then, the energy density can be found:

$$\rho_\gamma(\mu) = \frac{1}{\pi^2} \int f_{BE}(\mu) \nu^3 \mathrm{d}\nu = \rho_\gamma(0) \left(1 - \frac{\zeta(3)}{\zeta(4)} \mu \right) \tag{A.3}$$

[i] Note that in Planck units, this is also the dimensionless photon energy.

Version of July 22, 2021– Created July 22, 2021 - 14:39

where $\rho_\gamma(0) = (\pi^2/15)T_e^4$ is the photon energy density without chemical potential and $\zeta(n)$ is the Riemann zeta function, with $\zeta(4) = \pi^4/90$.
Similarly for the number density:

$$n_\gamma(\mu) = \frac{1}{\pi^2}\int f_{BE}(\mu)\nu^2 \mathrm{d}\nu = n_\gamma(0)\left(1 - \frac{\zeta(2)}{\zeta(3)}\mu\right) \tag{A.4}$$

where $n_\gamma(0) = (2\zeta(3)/\pi^2)T_e^3$ is the photon number density without chemical potential and $\zeta(2) = \pi^2/6$.
Taking the initial temperature before injection T_i and the injected energy $\delta\rho$, in order to satisfy conservation of energy, we must equate the total energy before and after injection, so:

$$\begin{aligned}\rho_\gamma|_{\text{before}} + \delta\rho &= \frac{\pi^2}{15}T_i^4\left(1 + \frac{\delta\rho}{\rho_\gamma}\right)\\ &= \rho_\gamma|_{\text{after}} = \frac{\pi^2}{15}T_e^4\left(1 - \frac{\zeta(3)}{\zeta(4)}\mu\right)\end{aligned} \tag{A.5}$$

And similarly, with the injected number of photons δn, in order to satisfy number conservation (which Compton scattering obeys), we have:

$$\begin{aligned}n_\gamma|_{\text{before}} + \delta n &= \frac{2\zeta(3)}{\pi^2}T_i^3\left(1 + \frac{\delta n}{n_\gamma}\right)\\ &= n_\gamma|_{\text{after}} = \frac{2\zeta(3)}{\pi^2}T_e^3\left(1 - \frac{\zeta(2)}{\zeta(3)}\mu\right)\end{aligned} \tag{A.6}$$

We can combine the two equations to get an expression for μ in terms of $\delta\rho$ and δn:

$$\begin{aligned}\frac{T_e^4}{T_i^4} &= \frac{1 + \frac{\delta\rho}{\rho_\gamma}}{1 - \frac{\zeta(3)}{\zeta(4)}\mu}\\ &= \left(\frac{T_e^3}{T_i^3}\right)^{4/3} = \left(\frac{1 + \frac{\delta n}{n_\gamma}}{1 - \frac{\zeta(2)}{\zeta(3)}\mu}\right)^{4/3} \approx \frac{1 + \frac{4\delta n}{3n_\gamma}}{1 - \frac{4\zeta(2)}{3\zeta(3)}\mu}\\ \Rightarrow (1 + \frac{\delta\rho}{\rho_\gamma})(1 - \frac{4\zeta(2)}{3\zeta(3)}\mu) &= (1 + \frac{4\delta n}{3n_\gamma})(1 - \frac{\zeta(3)}{\zeta(4)}\mu)\\ \mu\left[\frac{\zeta(3)}{\zeta(4)}(1 + \frac{4\delta n}{3n_\gamma}) - \frac{4\zeta(2)}{3\zeta(3)}(1 + \frac{\delta\rho}{\rho_\gamma})\right] &= 1 + \frac{4\delta n}{3n_\gamma} - (1 + \frac{\delta\rho}{\rho_\gamma}) = \frac{4\delta n}{3n_\gamma} - \frac{\delta\rho}{\rho_\gamma}\end{aligned}$$

Now we can approximate $\mu\delta n/n_\gamma \approx 0 \approx \mu\delta\rho/\rho_\gamma$, since $\mu \ll 1$ and $\delta n/n_\gamma \ll 1$, as well as $\delta\rho/\rho_\gamma \ll 1$. So finally, we have:

$$\mu = \frac{\frac{4\delta n}{3n_\gamma} - \frac{\delta\rho}{\rho_\gamma}}{\frac{\zeta(3)}{\zeta(4)} - \frac{4\zeta(2)}{3\zeta(3)}} = \frac{1}{4\frac{\zeta(2)}{\zeta(3)} - 3\frac{\zeta(3)}{\zeta(4)}}(3\frac{\delta\rho}{\rho_\gamma} - 4\frac{\delta n}{n_\gamma}) = \frac{1}{2.14185}(3\frac{\delta\rho}{\rho_\gamma} - 4\frac{\delta n}{n_\gamma}) \tag{A.7}$$

For our purposes, that is, decaying particles injecting both photons and heavier electromagnetic decay products, the injected number density will be negligible with respect to the injected energy density (because a non-relativistic particle decaying into photons means that the photons will be much more energetic than the background). Thus, we may safely ignore the number injection, and are left with:

$$\mu = \frac{3}{2.14185}\frac{\delta\rho}{\rho_\gamma} = 1.401\frac{\delta\rho}{\rho_\gamma} \tag{A.8}$$

We note here that the assumption that only Compton scattering takes part is only valid in the high-frequency spectrum, as stated in the main text, so these results apply only in that regime.
However, on longer timescales, the other processes are relevant as well, particularly double Compton scattering[ii], and the chemical potential evolves as a function of time. Neglecting Bremsstrahlung effects, an established chemical potential, without injection, will evolve according to [291]:

$$\frac{\mathrm{d}\mu}{\mathrm{d}t} = -\frac{\mu}{t_\mu} \tag{A.9}$$

where $t_\mu \approx 10^{35} z^{-9/2}$ s (with z the redshift). The full derivation of (A.9), and the origin of this t_μ is given in [291] and [205], but it is quite involved and not further relevant. Importantly for our application is the solution:

$$\mu(z=0) = \mu(z_0)\exp\left[-\left(\frac{z_0}{z_\mu}\right)^{5/2}\right] \tag{A.10}$$

where z_0 is the redshift at which formation of μ ceased, so free evolution started proceeding, and $z_\mu \approx 2\times 10^6$ is the redshift corresponding to the

[ii] Double Compton scattering dominates over Bremsstrahlung in the evolution of the chemical potential, as long as the baryon density of the universe $\Omega_B h^2 \lesssim 0.09$ [205]. For higher baryonic densities, Bremsstrahlung start to dominate. Our univere is well below this threshold; from Planck 2018 we have $\Omega_B h^2 = 0.0224$ [34], so we are justified in ignoring Bremsstrahlung for the evolution of the chemical potential.

Version of July 22, 2021– Created July 22, 2021 - 14:39

t_μ constant.
We see that these small distortions are exponentially damped. When we add a continuous energy injection (due to a decay process), (A.9) is modified to:

$$\frac{\mathrm{d}\mu}{\mathrm{d}t} = -\frac{\mu}{t_\mu} + 1.401\frac{\delta(\rho_{\rm inj}/\rho_\gamma)}{\delta t} \tag{A.11}$$

Here, we used (A.8) for the effect of energy injection on μ. Integrating this equation gives our final result:

$$\begin{aligned}\mu &= 1.401\int_0^{t_{\rm freeze-out}} \exp\left[-\left(\frac{z'(t)}{z_\mu}\right)^{5/2}\right]\frac{\mathrm{d}(\rho_{\rm inj}/\rho_\gamma)}{\mathrm{d}t}\mathrm{d}t \\ &= 1.401\int_{z_{\mu y}}^{\infty} \exp\left[-\left(\frac{z'}{z_\mu}\right)^{5/2}\right]\frac{\mathrm{d}(\rho_{\rm inj}/\rho_\gamma)}{\mathrm{d}z'}\mathrm{d}z'\end{aligned}$$

and, setting $\rho_{\rm inj} = Q$ we have arrived at (3.3).

A.2 Compton Distortion

First, we can describe the effect of energy injection on the photon energy density by the continuity equation (or conservation of the stress-energy tensor):

$$\frac{\partial\rho_\gamma}{\partial t} + 4H\rho_\gamma = \frac{\delta\rho_{\rm inj}}{\delta t} \tag{A.12}$$

with $H = \dot{a}/a$ is the Hubble parameter.
In addition, we can write this:

$$\frac{1}{a^4\rho_\gamma}\frac{\partial(a^4\rho_\gamma)}{\partial t} = \frac{1}{\rho_\gamma}\frac{\partial\rho_\gamma}{\partial t} + 4\frac{a^3}{a^4}\frac{\partial a}{\partial t} = \frac{1}{\rho_\gamma}\frac{\delta\rho_{\rm inj}}{\delta t}$$

Rewriting the Kompaneets equation to be in terms of ν instead of $x_e = \nu/T_e$, it becomes:

$$\frac{\partial f}{\partial t} - H\frac{\partial f}{\partial \nu} = n_e\sigma_T\frac{1}{m_e\nu^2}\frac{\partial}{\partial\nu}\left[\nu^4\left(T_e\frac{\partial f}{\partial\nu} + f + f^2\right)\right] \tag{A.13}$$

Then, using:

$$\rho_\gamma = \frac{1}{\pi^2}\int f\nu^3\mathrm{d}\nu$$

we can integrate (A.13) over frequency to arrive at [113]:

$$\frac{1}{a^4\rho_\gamma}\frac{\partial a^4\rho_\gamma}{\partial t} = 4n_e\sigma_T\frac{1}{m_e}\left(T_e - \frac{1}{4\rho_\gamma\pi^2}\int_0^\infty \nu^4 f(1+f)\mathrm{d}\nu\right) \tag{A.14}$$

where the last term represents energy transfer from recoil effects. Since we assume the per-particle energy of the injected decay products is significantly higher than the ambient photon energy, the distortion inducing electrons, whether they are decay products themselves or upscattered from high-energy photon decay products, are strongly heated with respect to the background ($T_e \gg \nu$).
Thus, we can ignore the recoil term, and we are left with the simple form:

$$\frac{1}{a^4\rho_\gamma}\frac{\partial a^4\rho_\gamma}{\partial t} = 4n_e\sigma_T\frac{T_e}{m_e} = \frac{1}{\rho_\gamma}\frac{\delta\rho_{\rm inj}}{\delta t} \tag{A.15}$$

Then we can integrate over the full time this takes place and, using the definition from arrive at:

$$\begin{aligned} y = \int_{t_{\mu y}}^{t_{\rm rec}} \frac{T_e}{m_e} n_e\sigma_T {\rm d}t &= \frac{1}{4}\int_{t_{\mu y}}^{t_{\rm rec}} \frac{{\rm d}(\rho_{\rm inj}/\rho_\gamma)}{{\rm d}t}{\rm d}t \\ &= \frac{1}{4}\int_{z_{\rm rec}}^{z_{\mu y}} \frac{{\rm d}(\rho_{\rm inj}/\rho_\gamma)}{{\rm d}z'}{\rm d}z' \end{aligned}$$

again, setting $\rho_{\rm inj} = Q$ we have arrived at (3.6).

Version of July 22, 2021– Created July 22, 2021 - 14:39

Appendix B

Appendix B: Average Electromagnetic Energy from Decay Products

In this appendix, we take the central values of branching ratios of decays and the masses of these particles from [150]. We only consider branching ratios that constitute 10% or more of the decay. For charged particles, we only take one specific charge, since the electromagnetic branching ratio is the same for both particles and anti-particles.

We start by taking the value of the average energy carried away by the electron in muon decay $\langle E_e \rangle / m_{\mu^-} = 0.35$ from [216]. Since muons decay as $\mu^- \to e^- \bar{\nu}_e \nu_\mu$ roughly 100% of the time, the electromagnetic branching ratio of muons is:

$$Br_{EM}^{\mu^-} = 0.35$$

For π^0, we have the decay mode $\pi^0 \to 2\gamma$ with branching ratio $Br_{\mu \to 2\gamma} \approx 1$, so:

$$Br_{EM}^{\pi^0} = 1$$

For π^- we have $\pi^- \to \mu^- \nu_\mu$ with $Br_{\pi^- \to \mu^- \nu_\mu} \approx 1$. For 2-body decay, we know that $\langle E_\mu \rangle / m_{\pi^-} = (1 + (m_\mu / m_{\pi^-})^2)/2 = 0.7865$. Then we have:

$$Br_{EM}^{\pi^-} = 0.7865 \cdot Br_{EM}^{\mu^-} = 0.275$$

For K^+, the dominant branching fractions are $Br_{K^+ \to \mu^+ \nu_\mu} \approx 63.56\%$ and $Br_{K^+ \to \pi^+ \pi^0} \approx 20.67\%$. When we neglect the smaller contributing decays, we do need to increase these fractions so that they make up 1 together.

Version of July 22, 2021– Created July 22, 2021 - 14:39

As such, we divide both fractions by $0.6356 + 0.2067 = 0.8423$. This gives $Br^{eff}_{K^+\to\mu^+\nu_\mu} = 0.755$ and $Br^{eff}_{K^+\to\pi^+\pi^0} = 0.245$.

We take for the energy of μ^+: $\langle E_{\mu^+}\rangle / m_{K^+} = (1 + (m_{\mu^+}/m_{K^+})^2) = 0.523$ and we assume that π^+ and π^0 both take about half of the total energy, since their masses are nearly equal[i].
In total, we have:

$$Br^{K^+}_{EM} = 0.755 \cdot (0.523 \cdot Br^{\mu^-}_{EM}) + 0.245 \cdot (0.5Br^{\pi^+}_{EM} + 0.5Br^{\pi^0}_{EM}) = 0.294$$

For η meson, we have $Br^{neutral}_{\eta} = 72.12\%$, where "neutral" describes decay to photons and π^0, both of which are purely electo-magnetic. For the charged decay modes, the dominant decay is $Br_{\eta\to\pi^+\pi^-\pi^0} = 22.92\%$. We scale up the fractions to form 100% as we did for K_+ to find: $Br^{eff}_{\eta\to\text{neutral}} = 0.759$ and $Br^{eff}_{\eta\to\pi^+\pi^-\pi^0} = 0.241$.

We assume here that each pion takes about one third of the total energy, on account of their masses being very close.
Then we get:

$$Br^{\eta}_{EM} = 0.759 + 0.241 \cdot (\frac{1}{3}Br^{\pi^0}_{EM} + \frac{2}{3}Br^{\pi^\pm}_{EM}) = 0.884$$

For ρ^0, we have $Br_{\rho^0\to\pi^+\pi^-} \approx 1$. Thus, we can directly write:

$$Br^{\rho^0}_{EM} = Br^{\pi^\pm}_{EM} = 0.275$$

For ρ^+, we have $Br_{\rho^+\to\pi^+\pi^0} \approx 1$. Assuming both particles get half of the total energy, we get:

$$Br^{\rho^0}_{EM} = \frac{1}{2}Br^{\pi^+}_{EM} + \frac{1}{2}Br^{\pi^0}_{EM} = 0.6375$$

Finally, η' meson, there are $Br_{\eta'\to\pi^+\pi^-\eta} = 42.5\%$, $Br_{\eta'\to\rho^0\gamma} = 29.5\%$ and $Br_{\eta'\to 2\pi^0\eta} = 22.4\%$. Scaling up like before, we have $Br^{eff}_{\eta'\to\pi^+\pi^-\eta} = 0.45$, $Br^{eff}_{\eta'\to\rho^0\gamma} = 0.31$ and $Br_{\eta'\to 2\pi^0\eta} = 0.24$.
For the energies, we use an approximation, taking $\langle E_\pi\rangle / m_{\eta'} \approx 0.2$ and

[i]The actual values are $\langle E_{\pi^+}\rangle / m_{K^+} = 0.5026$ and $\langle E_{\pi^0}\rangle / m_{K^+} = 0.4974$, which are so close to 0.5 that we can safely neglect the difference.

Version of July 22, 2021– Created July 22, 2021 - 14:39

$\langle E_\eta \rangle / m_{\eta'} \approx 0.6$. We find this from (5.11) by assuming the pions are massless. This is a rough approximation, but since these are fractions of fractions, the relative error from this approximation will be small. The two body decay gives $\langle E_{\rho^0} \rangle / m_{\eta'} \approx 0.66$ and $\langle E_\gamma / m_{\eta'} \rangle \approx 0.34$. In total, we find:

$$Br^{\eta'}_{EM} = 0.45 \cdot (0.4 \cdot Br^{\pi^\pm}_{EM} + 0.6 \cdot Br^{\eta}_{EM}) + 0.31 \cdot (0.34 + 0.66 \cdot Br^{\rho^0}_{EM}) + 0.24 \cdot (0.4 \cdot Br^{\pi^0}_{EM} + 0.6 \cdot Br^{\eta}_{EM}) = 0.63$$

Version of July 22, 2021– Created July 22, 2021 - 14:39